GRADUATE THESIS/DISSERTATION APPROVAL FORM AND SIGNATURE PAGE

Instructions: This form must be completed by all master's and doctoral students with a thesis or dissertation requirement. Please type or print clearly as this form MUST be included as page 1 of your thesis or dissertation via electronic submission to ProQuest. All theses and dissertations must be formatted according to the University and department/program requirements. **Reminder:** It is the responsibility of the student to submit any/all edits requested by the Examining Committee to the Faculty Mentor or Supervising Professor for final approval and signature via the Graduate Program Completion Form.

Type: ☐ Master's Thesis ☑ PhD/Doctoral Thesis or Dissertation

Thesis or Dissertation Title: Investigating the Interfacial Bonding Strength of Additively Manufactured Polyetheretherketone Intervertebral Devices

Author's Name: Cemile Basgul

Month and Year: 01/2021

The signatures below certify that this thesis / dissertation (circle one) is complete and approved by the Examining Committee.

Committee Chairperson's Name: Kenneth Barbee, PhD

Title: Professor, Senior Associate Dean, and Associate Dean for Research

Department: The School of Biomedical Engineering, Science and Health Systems

Institution (*if other than Drexel University*): Drexel University

Signature:

Committee Member's Name: Banu Onaral, PhD

Title: H. H. Sun Professor and Senior Advisor to the President, Global Partnerships

Department: The School of Biomedical Engineering, Science and Health Systems

Institution (*if other than Drexel University*): Drexel University

Signature: BANU ONARAL

Committee Member's Name: Joseph Sarver, PhD

Title: Teaching Professor

Department: The School of Biomedical Engineering, Science and Health Systems

Institution (*if other than Drexel University*):

Signature:

Committee Member's Name: Steven M. Kurtz, PhD

Title: Research Professor/Principal

Department: The School of Biomedical Engineering, Science and Health Systems/Exponent

Institution (*if other than Drexel University*): Drexel/Exponent

Signature:

Committee Member's Name: Michele Marcolongo, PhD

Title: Drosdick Endowed Dean

Department: Material Science and Engineering/College of Engineering at Villanova University

Institution (*if other than Drexel University*): Drexel/Villanova University

Signature:

Committee Member's Name:

Title:

Department:

Institution (*if other than Drexel University*):

Signature:

Investigating the Interfacial Bonding Strength of Additively Manufactured Polyetheretherketone Intervertebral Devices

A Thesis

Submitted to the Faculty

of

Drexel University

by

Cemile Basgul

in partial fulfillment of the

requirements for the degree

of

Doctor of Philosophy

January 2021

Dedications

This dissertation is dedicated to my mom, Müge Erol, my dad, Levent Başgül, my sister, Sena Başgül, my fiancé, Cihan Asar, and my grandmother, Kadriye Erol.

Acknowledgments

I would like to start by thanking my family: my mom, for being a role model as a strong independent woman and starting my journey in traveling abroad when I was 18; my dad, for being an exceptional Turkish dad and supporting my decisions in every direction; my sister, even we spent more time apart than together, for making me feel so proud with her kindness and encouragement; my Swiss mom Daniela Bättig, for being a second mom to me since my exchange year and expanding my horizon; and finally, my fiancé Cihan, who supported me in every way he could even from miles away. I would like to articulate my gratitude to my friends: Dilara Berkay, who supported my mental health in these years especially during corona times by walking at least two hours every day; Yasin Hasekioglu for being the young enthusiastic engineer friend with whom I could bounce ideas off; and Lexi Jednorski for sharing the Ph.D. experience in Biomedical Engineering with me and reviewing my work whenever I needed her. Thank you all for sharing this experience with me and always being there for me along the way.

I would like to extend my appreciation to my advisor, Dr. Kurtz. Thanks for this incredible adventure. Thanks for always believing in me from the very beginning. Thanks for seeing my strengths and introducing me to 3D printing. I will always appreciate that. Thanks for respecting my opinions, allowing me to travel and explore, and pushing me on new adventures to always catch up with the cutting-edge research. Finally, thanks for your support in helping me turn my weaknesses into my strengths throughout this journey. I have learned so much from your wisdom.

To all past and present members of Implant Research Core, thank you for an openminded, respectful, supportive, and collaborative learning environment. Special thanks to Anthony Law, for facing the challenges in 3D printing with me and making it easier and more fun to tackle the issues that arose along the way and being a good friend who was always there to help; to Hannah Spece, for sharing this Ph.D. experience side to side with me, from group projects in the classes until the end by reviewing the papers, sharing ideas, and always supporting me with a positive attitude; and finally, to Dan MacDonald, for being the second advisor after Steve, sharing ideas and providing invaluable feedback at every step along the way. I extend my appreciation to the members of Exponent Inc.: Ryan Siskey who shared and provided ideas for my questions related to mechanical testing and to Nancy Siciliano for providing emotional support, a welcoming smile and encouragement before the meetings and presentations.

I would like to thank my colleagues from Germany: Uwe Popp and Lars Pfotzer, for being so hospitable, helpful, and open to collaborations for research and supporting this work in your company; to my friends, Shashidhar Gorantla, who always shared his extensive knowledge in 3D printing, supported my research and ideas, made quick returns to my questions in between his own work; and Elena Reznikova and Nadiia Churinova who shared their workspace, living space and food with me during my times in Karlsruhe.

I express my gratitude first to ThinkSwiss and ON Foundation organizations which made it possible to travel to the University Hospital of Basel twice for the completion of this work, even in corona times. To Dr. Florian Thieringer, thank you for hosting me twice in their labs and the hospital, for the experience to be in a hospital environment for 3D printing with craniomaxillofacial surgeons, introducing me to the most interesting surgeries, being a great advisor during my times in Basel. To the friends from the 3D print Lab, thank you, Neha Sharma and Shuaishuai Cao. I would also like to thank the University of Basel DBE team, especially Yakub Bayhaqi and Arsham Hamidi, for sharing their knowledge in thermal data collection and analysis and answering my questions all the time.

Last but not least, I would like to thank my co-advisor Dr. Barbee, who helped me design my ideas especially in modeling part of this work and supported my development through this dissertation and to my committee members, Drs. Banu Onaral, Michele Marcolongo, and Joseph Sarver, for their guidance and support throughout my Ph.D. journey.

Table of Contents

List of Tables

List of Figures

List of Abbreviations

1D	One-dimensional
2D	Two-dimensional
3D	Three-dimensional
ABS	Acrylonitrile butadiene styrene
ADSC	Adipose tissue-derived stem cells
AgNP	Silver nanoparticles
Al_2O_3	Aluminum oxide
AM	Additive Manufacturing
ASTM	American Society for Testing and Materials
BC	Boundary condition
BMSC	Bone marrow-derived stem cell
b-TCP	Beta-tricalcium phosphate
CF/CFR	Carbon fiber reinforced
CMF	Cranio-maxillofacial
DIOP	Diopside
DOH	Degree of healing
E.coli	Escherichia coli (gram negative bacteria)
FFF	Fused Filament Fabrication
GO	Graphene oxide
HA	Hydroxyapatite
hFOB1.10	Human fetal osteoblastic cells
h-MSC	Human mesenchymal stem cells
HT	Heat transfer
HTM	Heat transfer model
IC	Initial condition
IF	Interbody fusion
ILC	Intervertebral lumbar cage
IR	Infrared
ISO	International Organization for Standardization
KDIOP	3-glycidoxypropyltrimethoxysilane with DIOP
L929 cells	Mouse derived fibroblasts
LIF	Lumbar interbody fusion
MC3T3-E1 cells	Mouse derived fibroblast-like cells

MG63 cells	Human osteosarcoma fibroblasts
MSC	Mesenchymal stem cells
PAEK	Polyaryletherketone
PC	Polycarbonate
PEEK	Polyetheretherketone
PEKK	Polyetherketoneketone
PGA	Polyglycolic acid
PLA	Polylactic acid
PLGA	Polylactic-co-glycolic acid
PLIF	Posterior lumbar interbody fusion
PLLA	Poly-L-lactic acid
POC	Point of care
PRISMA	The Preferred Reporting Items for Systematic Reviews and Meta-Analyses
PSI	Patient-specific implant
PVA	Polyvinyl alcohol
ROI	Region of interest
S. aureus	Staphylococcus aureus (gram-positive bacteria)
SAOS-2 osteoblasts	Human osteosarcoma cells
SEM	Scanning electron microscopy
SLS	Selective laser sintering
STL	Standard Triangle Language
TASS	Total alkaloids from Semen Strychnine
Ti	Titanium
TiO_2	Titanium dioxide
TPU	Thermoplastic Polyurethane
WAXS	Wide-angle x-ray scattering
XRD	X-ray diffraction
ZrO_2	Zirconium dioxide

Abstract

Investigating the Interfacial Bonding Strength of Additively Manufactured Polyetheretherketone Intervertebral Devices
Cemile Basgul

Interlayer delamination in Additively Manufactured (AM) PEEK implants has been shown to have detrimental mechanical consequences, and recent clinical observations have suggested that it may compromise the integrity of patient-specific Fused Filament Fabricated (FFF) PEEK implants. This dissertation describes thermally driven healing mechanisms in FFF PEEK by developing a model to quantitively assess the healing to evaluate the interlayer adhesion phenomena. Furthermore, it provides an overview of the AM technologies, materials, parameters, design variables, and clinical applications that have been previously studied to understand their impact on the performance of AM PEEK implants.

Firstly, FFF parameters that indirectly controlled the thermal mechanisms were evaluated for PEEK spinal cages printed using the first two generations of FFF machines. Layer delamination as a failure mechanism was identified in both generations of FFF PEEK cages. Altering the cooling time of a layer was not able to change the failure mechanism of FFF cages; however, it improved the mechanical strength of the cages. Although the main temperature settings used to 3D print cages in two generations of FFF machines were different, the mechanical strength did not differ between the two generations of cages. Printing a single cage per build, which decreased the layer cooldown time, was associated with a higher ultimate load than printing

multiple cages per build. Regardless of the cage number printed per build, cages printed with a bigger nozzle demonstrated a higher ultimate load than cages printed with a smaller nozzle, in which the layers cooled down twice as fast.

Considering the thermal mechanisms that affect the layer adhesion, a 1D heat transfer model (HTM) was developed to assess the interlayer and layer temperatures in a FFF PEEK build. The temperature evolutions calculated from HTM were then employed in the non-isothermal degree of healing model. The healing was higher between the upper layers with reference to the print bed when compared to the lower layers. Among the three key FFF temperatures, the nozzle temperature was the most crucial in layer healing. Once it was below a specific value, none of the layers healed properly. The degree of healing increased with the improved build plate temperature allowing more layers to heal 100%. Despite the environment temperature being less influential on the healing of lower layers, more layers healed completely with the chamber temperature increment.

Finally, the heat transfer constituent of the established model to examine the FFF PEEK layer temperatures was validated individually with industrial (2nd) and medical (3rd) generation FFF machines. As observed in theoretical temperature evolutions, the experimental results were in agreement that the temperatures of upper FFF PEEK layers would stay higher. The comparison of the model and the experiments for layer temperatures during FFF processes in both machines overlapped particularly closer to the mid-layers. During the first quarter of the print period, where the healing calculations would be affected, model approximations were converged to the experimental temperatures earlier (beginning at the 20^{th} layers) in both machines and were aligned with the upper layer temperatures until the top of the FFF PEEK builds. The detailed validation method presented here for heat transfer models on determining the layer temperatures of FFF builds will promote further model developments as well as HTM implementation in healing models. The framework introduced in this thesis will enable the parameter optimization to achieve sufficiently healed layers through FFF builds, thus enhancing the macro mechanical properties of FFF PEEK implants for AM at point-of-care.

Chapter 1: Background and Significance

1.1 Clinical Relevance of Intervertebral Devices

Spinal fusion, also known as interbody fusion (IF), is the most common spinal procedure performed in the United States (U.S.), with over 352,000 cases annually [1]. IF is performed to relieve the pain and pressure on the spinal cord that might be caused by various conditions such as intervertebral disc wear out (degenerative disc disease) (Fig. 1.1(A)), spinal stenosis, spondylolisthesis, spondylosis, spinal fractures, scoliosis, and kyphosis [2, 3]. IF was first described in 1944 by Briggs and Milligan, who used a posterior approach as an alternative to posterolateral fusion techniques [4]. Lumbar interbody fusion (LIF) was the most common type of fusion operation performed; ~210,000 cases per year in the U.S. between 1998 and 2008 [5]. The average age for someone who underwent a primary LIF was 56.3 years, with an average hospital stay of 3.9 days. According to this study, both the mean total hospital charges associated with spinal fusion and the national bill for spinal fusion increased significantly in 10 years (3.3 & 7.9 times, respectively). Furthermore, cumulated hospital costs increased 177% in 12 years (until 2015), exceeding $10 billion in 2015, with an average of $50,000 per admission for LIF [6]. Posterior lumbar interbody fusion (PLIF) is one of the fusion techniques to fuse both the anterior and posterior columns of the spine. The anterior column stability is ensured via a bone graft and/or intervertebral lumbar cage(s) (ILC) to reduce post-operative complications and pseudarthrosis [7], while the pedicle screws, rods, and the bone graft create rigidity in the posterior spine (Fig. 1.1(B)).

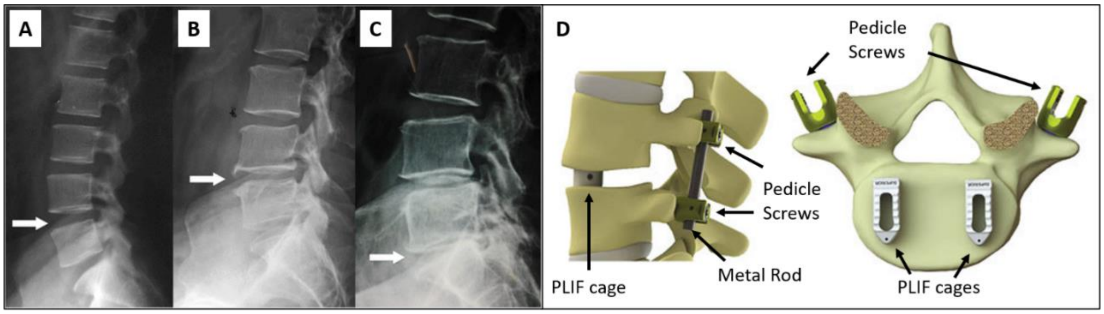

Figure 1. 1. Lumbar disc degeneration in the lateral lumbar spine (indicated with white arrows) with no disc space narrowing (A), mild disc space narrowing (B), and moderate disc space narrowing (C), reprinted from Perera et al. [8] with permission of Springer Nature (http://creativecommons.org/licenses/by/4.0/). Posterior lumbar interbody fusion (PLIF) example with PEEK intervertebral lumbar cage instrumentation (D) (www.solvay.com/en/chemical-categories/specialty-polymers).

Other techniques, including anterior, direct lateral, oblique lateral, and transforaminal LIF, were introduced later; however, none of these techniques proved clinical superiority over the posterior approach, which remains the most used technique for fusions [5].

The intervertebral cage is one of the key components in lumbar fusion which occurs around six months. In the meantime, ILCs assure the spine's structural stability by maintaining the height of the intervertebral disc and stabilizing the force distribution between the vertebral bodies [2, 3]. Autologous bone grafts were used initially to contain the closest properties to the bone, however, increased healing times or high failure rates were associated with donor site morbidity, collapse, subsidence, retropulsion, or resorption of the graft [9].

The most common biomaterials used in interbody fusion devices are titanium and Polyetheretherketone (PEEK) [7]. The first intervertebral devices introduced for interbody fusion in 1986 were made from titanium [10]. Titanium was a favorable material because of its corrosion resistance, low density, and osseointegration capacity [11-13]. Titanium cages were successful in fusion, however, radiopacity makes it hard to determine the position of the cage(s) with reference to the spinal cord and visualize bone ingrowth [14]. Moreover, titanium's high stiffness value (Elastic modulus (E) =50.2 GPa) compared to the cortical and cancellous bones (14.6 and 3.87 GPa, respectively [9]) causes gradual penetration of the cage into the vertebrae and subsidence of the intervertebral disc height occurs [15, 16]. PEEK intervertebral cages were introduced as an alternative to titanium spinal cages to overcome these disadvantages [17]. PEEK is biocompatible and provides durability and strength while having a closer elastic modulus (E=3.84 GPa) both to the cortical and cancellous bone than titanium [18]. Most importantly, its radiolucency allows for radiographic monitoring of the fusion surgery by tracking bone growth and/or misalignment. However, aside from its benefits, PEEK's hydrophobicity inhibits osseointegration, which may result in unsatisfactory outcomes of fusion [19]. There have been efforts to introduce modifications to PEEK cages to create surface porosity and hence improve osseointegration [20]. However, traditional manufacturing techniques are limited in design changes that are restricted to certain areas of the cage's outer surfaces.

1.2 Additive Manufacturing PEEK Implants

Additive Manufacturing (AM), more commonly known as three-dimensional (3D) printing, has introduced a new frontier for medical device manufacturing at the point of care (POC) [21-26], bringing added versatility by allowing the creation of more complex geometries and ensuring the reproducibility of well-defined porous implants in the future. In 2017, overall, AM had an annual growth rate of 21% with a $7.3 billion market size [27]. When 3D printing in healthcare is considered, the number of U.S. hospitals with a centralized 3D printing facility increased by 3200% between 2010 and 2016 care (99 hospitals). 16 hospitals of the top 20 (as ranked by U.S. News and World Report) implemented a medical 3D printing strategy. Many attractions would contribute to this increase in AM-POC. The precision of AM-POC is increasing with better patient outcomes and lower costs of developing treatment plans and devices specifically for the patient. In addition, 3D printing technologies become more accessible with various materials for specific applications and improved software that allows more accurate segmentation of medical images and more complex implant designs.

Fused Filament Fabrication (FFF) is a type of Additive Manufacturing method where the material is heated above its glass transition temperature (T_g) and then extruded through a heated nozzle onto a preferably heated bed. It has the advantage of saving material over other AM techniques such as powder sintering, where the technology is costly, and recycling is not a preferred option for PEEK powder. Compared to powder systems, FFF printers are more suitable regarding contamination and sterility in a hospital setting. Therefore, FFF has attracted researchers for orthopedic and spinal implant manufacturing, including spinal cages. FFF has been used to manufacture various biomedical applications from different polymeric biomaterials, including PEEK [28-30].

FFF PEEK was investigated for various therapeutic areas such as spinal [31-35], craniomaxillofacial (CMF) [36], dental [37], and chest constructions [38-41], which are discussed comprehensively through Chapter 2. While *in vitro* and *in vivo* research is still ongoing for FFF PEEK's clinical use, three studies implanted FFF PEEK patient-specific implants (PSI) for chest reconstruction due to excessive osteotomies to remove cancerous tumors [38, 40, 41]. One patient received a custom-designed FFF PEEK rib prosthesis for bone replacement due to tumor resection [40]. In another study, the patient was implanted with a FFF PEEK scapula to treat an invasive bone tumor [41]. Lastly, 18 patients were treated with either a FFF PEEK anterior chest wall along with the ribs or FFF PEEK ribs for chest wall reconstruction [38]. Although good qualitative outcomes were recognized [40], failure of a FFF PEEK PSI was also disclosed three months after implantation [41]. Further investigations are needed to interpret such failures for FFF PEEK implant optimization.

Temperature management is very important for FFF since it relates to interlayer bonding strength [42, 43], the crystallinity of the polymer [44], and the deformation of the printed part [45, 46] affecting its macro mechanical properties. Although previous research has shown the feasibility of FFF PEEK for implants, the importance of the interlayer bonding was mentioned as the failure mechanism for the macro mechanical properties of FFF PEEK spinal cages [47]. Moreover, although dimensional accuracy of FFF PEEK cranial PSIs were recognized clinically, different zones of crystallinity that caused layer delamination was mentioned that would require optimum thermal management during the FFF process to manufacture optimum implants (Fig. 1.2) [48].

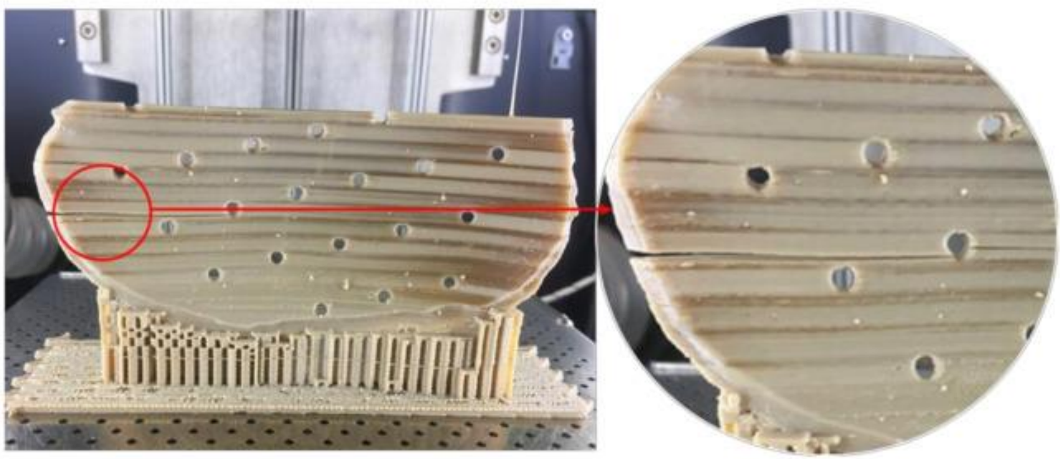

Figure 1. 2. In addition to discoloration due to inefficient crystallization, interlayer delamination (red circle) observed in FFF PEEK Cranial implants during the printing process in the hospital, reprinted from Sharma et al. [48] with permission of MDPI, Basel, Switzerland (http://creativecommons.org/licenses/by/4.0/).

Hence, understanding the heat transfer mechanisms in FFF is essential to manufacture PEEK implants with uniform layer adhesion and improve the mechanical properties [42].

1.3 Thermal Modeling for FFF

Heat transfer of melted polymer and solidification of the layers that are being extruded and repetitive thermal loading of the growing FFF build are important processes that control the final quality of the part. The thermal energy stored in the molten material is redistributed into the part through conduction and is consumed by lateral convection cooling. The layer delamination failure mechanism in FFF PEEK is strongly associated with the thermal conditions controlled by direct and indirect thermal parameters [31, 49]. However, there is no thermal model that analyzes the FFF PEEK layer temperatures via heat transfer.

Previous researchers investigated the relationship of the filament bonding strength and the processing parameters experimentally [42, 50, 51]. Sun et al. [42] analyzed the processing temperatures on the bonding quality of ABS FFF parts and presented that nozzle temperature, environment temperature, and cooling conditions significantly affect the bonding quality of filaments. Similarly, Rodriguez et al. [52] showed that the bonding strength of ABS filaments could be increased by the nozzle and environment temperatures. Moreover, Arif et al. [50] demonstrated that the mechanical performance of FFF PEEK parts was significantly affected by fiber bonding which was regulated by the thermal conditions during the printing process. Thus, temperature management during the FFF process is crucial for the mechanical properties of the FFF build.

Consequently, studies have been interested in analyzing the temperature profiles of FFF processes theoretically to achieve mechanically more stable parts via FFF by optimizing the parameters. One of the first computational models for thermal analysis of fused deposition was developed in 1995 by Yardimci et al. [53], where they concentrated on the cooling behavior of single and multiple filaments by developing 2D heat transfer analysis using finite element methods. Later in 2000, Thomas and Rodriguez [54] obtained thermal histories using an analytical 2-D transient heat transfer analysis for rectangular cross-sections of ABS filaments. Similarly, Bellehumeur et al. [55] estimated the cooling profile of the extruded ABS filaments via thermal analysis of the FFF process. They simplified a single deposition filament as a one-dimensional block hence used a one-dimensional transient heat transfer model, which was then solved analytically via the lumped capacity method (Fig. 1.3). Costa et al. [56] expanded the above efforts by proposing a 1D heat transfer analysis of ABS filament deposition that includes the physical contacts between any filament and its neighbors or print bed.

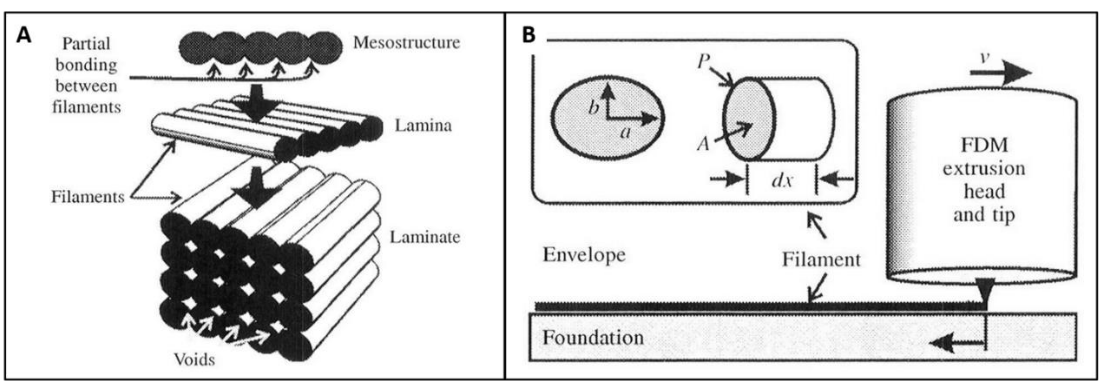

Figure 1. 3. In early heat transfer analysis for FFF, filament temperatures and bonding were studied, which forms layers (indicated as lamina (A)) and the printed part at the end (indicated as a laminate (A)). Depending on the model assumptions considering the heat transfer in one direction or two directions, simplifications were made to

examine the filament temperature (B), reprinted from Bellehumeur et al. [55] with permission of Elsevier.

Later on, Costa et al. [49] used the previously developed model to predict the ABS filament temperatures on a 3D printed geometry design by defining the filament deposition sequence. In addition to the previous work, they included experimental measurements of filament temperatures via thermal readings. Unlike previous models, Zhang et al. [57] defined a sub-milli-metrical cuboid as their element, where they considered the heat transfer from the deposition of PLA elements and modeled it numerically. Depending on the geometry, they defined the element sequence extruded for their algorithm. Furthermore, Ravoori et al. [58] developed an analytical heat transfer model for a single PLA filament extruded on the print bed based on the moving heat source theory. They included experimental measurements via infrared thermography of temperature field on the print ped as a function of time during the filament extrusion. These previous studies were all conducted on filament temperature estimations of low-temperature polymers. One study [59] so far investigated FFF PEEK. They used a 1D heat transfer model by considering the relationship between the cross-sectional shape of the filament and the printing parameters to predict the surface roughness of printed PEEK coupons. However, this study did not include one of the main FFF temperatures: the chamber or environment temperature; but only based the study on the nozzle and the bed temperatures. Finally, only Compton et al. [60] examined the layer temperature via 1D heat transfer analysis numerically for large-scale (358 mm long) CF-ABS builds that were printed as a thin wall. They also compared the model with experimental layer temperatures from thermal videos during FFF in an open environment.

1.4 Degree of Healing

Lee and Springer [61] used an autohesion model for an interface in isothermal conditions in 1987. They mentioned that when intimate contact happens between two polymer interfaces, the bonding process starts due to autohesion. This autohesion is explained by the diffusion of the chain-like molecules across the interface. They approximated the degree of autohesion by the following equation, which increases in time with increased molecular diffusion.

$$D_{au} = x t_{\alpha}^{1/4} \tag{1}$$

Where t_{α} is the time spent from the beginning of the autohesion when the interfaces come into contact and x is the constant related to the Arrhenius equation via temperature.

$$x = x_0 \exp\left(-\frac{E}{RT}\right) \tag{2}$$

x_0 is material dependent constant, E is the activation energy that initiates autohesion, and R is the universal gas constant. They calculated the constant x experimentally for PEEK 150P (Victrex®) as,

$$x = 44.1 \exp \frac{3810}{T\ (K)} \quad s^{-1/4} \tag{3}$$

Later on, Yang and Pitchumani [62] defined the non-isothermal degree of healing (DOH) depending on the reptation movement of a linear polymer chain (Fig. 1.4).

$$Dh(t) = \left[\int_0^t \frac{1}{t_w(T)} dt \right]^{1/4} \tag{4}$$

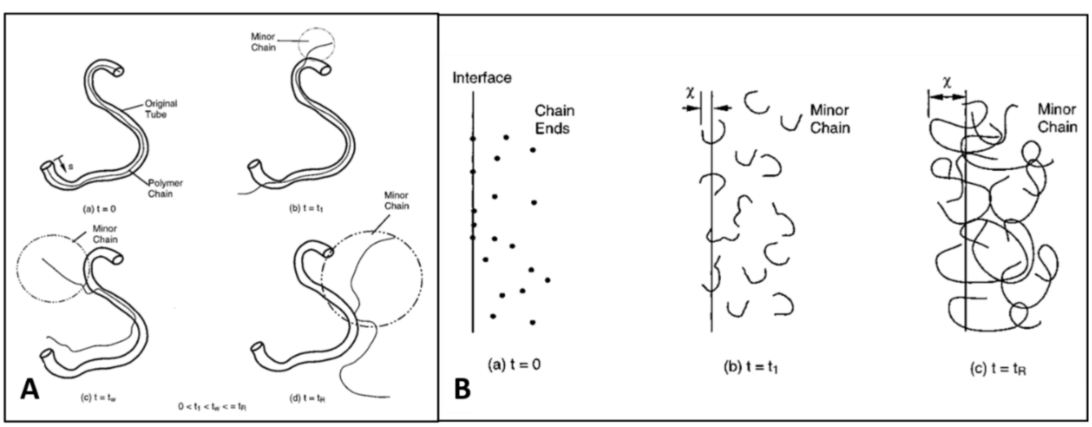

Figure 1. 4. According to the reptation theory, a linear polymer chain leaves the original membrane at reptation time (t_R), and at welding time ($t_W \leq t_R$) maximum bonding strength is reached (A). Once intimate contact is achieved between surfaces,

interdiffusion of minor chains across the polymer interface starts and increases with time (B), reprinted with permission from Yang and Pitchumani [62] Copyright (2020) American Chemical Society.

t_w is the welding function which they calculated via healing experiments of CFR-PEEK.

$$t_w = A\, exp\left[\frac{E}{R}\ \left(\frac{1}{T} - \frac{1}{T_{ref}}\right)\right] \tag{5}$$

Once the temperature-dependent welding time is known for a given temperature history, the degree of healing (referred to as autohesion previously) can be calculated via Equation 4. Costa et al. [49] employed the DOH model developed by Yang and Pitchumani [62] in predicting the bonding degree of filaments in a FFF ABS build. When DOH was above or equal to one, 'good adhesion' was considered and below one was stated as 'poor adhesion'. Furthermore, Yin et al. [63] implemented the non-isothermal DOH in determining the TPU/ABS interface strength, which was achieved via multi-material printing.

Moreover, Ko et al. [64] used the isothermal degree of healing to predict the filament healing in PC-ABS parts with different weight percentages of PC and printed with different infill patterns. All these previous studies used the healing model for predicting the healing between the FFF filaments. Finally, a recent work [65] used a slightly different non-isothermal degree of healing formula than 'Equation 4' developed for toughness [62]. They compared the theoretical degree of healing calculated for ABS layers with the mechanically tested notched FFF ABS samples by pausing the FFF process for 30 seconds at a certain height of the printed object (10 mm). Although both isothermal and non-isothermal healing models have been researched for FFF, so far, the literature involved only low-temperature polymers that are not suitable for load-bearing implants, such as intervertebral cages. Additionally, healing mechanisms of low and high-temperature polymers such as PEEK would be completely different since it was stated that the healing mechanisms are only effective once the temperature is above the glass transition point (Tg) for amorphous polymers and the melting temperature (Tm) for semicrystalline polymers such as PEEK. A comprehensive model for quantitively understanding the interlayer bonding mechanism on FFF PEEK is needed.

In this research, interlayer delamination phenomena in FFF PEEK was evaluated using a heat transfer based non-isothermal healing model. First, FFF parameters to 3D print PEEK cages were tested by considering the indirect thermal parameters were associated with the layer healing thus the mechanical properties of FFF cages manufactured. Next, the 1D heat transfer model and the non-isothermal healing theory were proposed to predict the layer healing degree of FFF PEEK layers. Furthermore, the effects of FFF key temperatures that contribute to healing was examined using the developed model. Finally, The HTM that examines the layer temperatures was validated by thermal readings using industrial and medical generations of FFF PEEK printers.

1.5 Overview of Specific Aims

1.5.1 Central Hypothesis

Thermal parameters may impact the interlayer bonding strength for fused filament fabricated PEEK Spinal Cages. It was hypothesized that a heat transfer-based non-isothermal polymer healing model can be used to determine the optimum parameters for a controlled Fused Filament Fabrication environment while additively manufacturing PEEK. The execution of these aims provides a direct assessment of the interlayer bonding degree of 3D printed PEEK builds and establishes a quantitative model for interlayer debonding phenomenon stated for the Fused Filament Fabrication PEEK. The use of the model will allow for optimizing the parameters of FFF PEEK implants, providing crucial insights into the thermally controlled environment of PEEK printing. This approach may be leveraged for modifying FFF technologies to achieve better interlayer strength for FFF PEEK implants in AM-POC.

1.5.2 Specific Aim 1: Investigate the effect of the current FFF technology parameters on the structural stability of 3D printed PEEK cages.

FFF parameters that affect the thermal conditions during printing impact the mechanical properties of 3D printed structures [42]. However, so far, it is poorly understood how the failure mechanism of a load-bearing PEEK implant will be affected via altering the FFF process parameters which indirectly control the thermal conditions. Within this aim, PEEK cages were 3D printed in two generations (1^{st} and 2^{nd}) of FFF machines under different print speeds, with different nozzle diameters and layer thicknesses, and with different numbers per build. The micro-structures and macro mechanical properties of FFF PEEK cages were evaluated. The hypothesis was that decreasing the cooling time of layers via indirect thermal parameters in FFF will improve the layer healing, thus increase the mechanical loads that FFF PEEK cages can bear.

1.5.3 Specific Aim 2: Develop a heat transfer based non-isothermal layer healing model to improve the interlayer strength for 3D printed PEEK implants.

Improved interlayer strength to enhance the macro mechanical properties of FFF PEEK implants is necessary by addressing the issue of interlayer delamination phenomena of FFF AM. Thus, a comprehensive model is crucial to understand the heat transfer fundamentals that affect layer healing on FFF PEEK implants. First, a heat transfer model was developed to assess the thermal history of the FFF PEEK layers and interfaces with the help of constant parameters (e.g., printing speed, nozzle diameter, layer thickness) defined by Aim 1. Second, the theoretical thermal distributions of the deposited layers were implemented into a non-isothermal healing model to determine the healing degree between FFF PEEK layers. Additionally, the impact of the key FFF process temperatures (print bed (T_B), chamber (T_C), and nozzle temperatures (T_N)) on the degree of healing across the FFF PEEK layers was evaluated using the model. We hypothesized that the heat transfer (HT) based non-isothermal degree of healing model, developed simulating the FFF process, would help to optimize both direct and indirect thermal FFF parameters, hence, improve the quality of interlayer bonding in FFF PEEK implants.

1.5.4 Specific Aim 3: Validate the theoretical layer temperatures determined via heat transfer model established with the experimental FFF PEEK layer temperatures obtained from two different FFF machines.

Although interlayer delamination has been shown as the failure mechanism in FFF PEEK, layer temperatures of FFF PEEK constructs were never examined experimentally in the literature. Specific validation of FFF PEEK layer temperature predictions is critical for the proposed heat transfer model before its further applications in layer healing approximations. Thus, the model geometry (cuboid) used in Aim 2 was 3D printed in the industrial and medical generations of FFF PEEK machines. Thermal videos were recorded during both FFF processes which were then analyzed to achieve the layer temperatures of the PEEK cubes. The heat transfer model was validated with the experimental layer temperatures collected from the two FFF machines. This aim presented a validation method for HTM developed for FFF layer temperature predictions. We hypothesized that the previously exhibited 1D HTM could estimate the FFF PEEK layer temperatures through the FFF build and tolerate the initial geometry change due to a different FFF system with additional heat transfer mechanisms.

1.6 References

1. *How Many Spinal Fusions are Performed Each Year in the United States?* 2018 [cited 2021 01/06/2021]; Available from: https://idataresearch.com/how-many-instrumented-spinal-fusions-are-performed-each-year-in-the-united-states/.
2. McGilvray, K.C., et al., *Evaluation of a polyetheretherketone (PEEK) titanium composite interbody spacer in an ovine lumbar interbody fusion model: biomechanical, microcomputed tomographic, and histologic analyses.* Spine J, 2017.
3. Asil, K. and C. Yaldiz, *Retrospective Comparison of Radiological and Clinical Outcomes of PLIF and TLIF Techniques in Patients Who Underwent Lumbar Spinal Posterior Stabilization.* Medicine (Baltimore), 2016. **95**(17): p. e3235.
4. Briggs, H. and P.R. Milligan, *CHIP FUSION OF THE LOW BACK FOLLOWING EXPLORATION OF THE SPINAL CANAL.* JBJS, 1944. **26**(1): p. 125-130.
5. Rajaee, S.S., et al., *Spinal Fusion in the United States: Analysis of Trends From 1998 to 2008.* Spine, 2012. **37**(1): p. 67-76.
6. Martin, B.I., et al., *Trends in Lumbar Fusion Procedure Rates and Associated Hospital Costs for Degenerative Spinal Diseases in the United States, 2004 to 2015.* Spine (Phila Pa 1976), 2019. **44**(5): p. 369-376.
7. Verma, R., S. Virk, and S. Qureshi, *Interbody Fusions in the Lumbar Spine: A Review.* HSS Journal ®, 2020. **16**(2): p. 162-167.
8. Perera, R.S., et al., *Associations between disc space narrowing, anterior osteophytes and disability in chronic mechanical low back pain: a cross sectional study.* BMC Musculoskelet Disord, 2017. **18**(1): p. 193.
9. Warburton, A., et al., *Biomaterials in Spinal Implants: A Review.* Neurospine, 2020. **17**(1): p. 101-110.
10. Grob, D., S. Daehn, and A.F. Mannion, *Titanium mesh cages (TMC) in spine surgery.* Eur Spine J, 2005. **14**(3): p. 211-21.
11. Chong, E., et al., *The design evolution of interbody cages in anterior cervical discectomy and fusion: a systematic review.* BMC Musculoskelet Disord, 2015. **16**: p. 99.

12. Najeeb, S., et al., *Nanomodified Peek Dental Implants: Bioactive Composites and Surface Modification—A Review.* International Journal of Dentistry, 2015. **2015**: p. 381759.

13. Rao, P.J., et al., *Spine interbody implants: material selection and modification, functionalization and bioactivation of surfaces to improve osseointegration.* Orthop Surg, 2014. **6**(2): p. 81-9.

14. Cutler, A.R., et al., *Comparison of polyetheretherketone cages with femoral cortical bone allograft as a single-piece interbody spacer in transforaminal lumbar interbody fusion.* J Neurosurg Spine, 2006. **5**(6): p. 534-9.

15. Chen, Y., et al., *Comparison of titanium and polyetheretherketone (PEEK) cages in the surgical treatment of multilevel cervical spondylotic myelopathy: a prospective, randomized, control study with over 7-year follow-up.* European Spine Journal, 2013. **22**(7): p. 1539-1546.

16. Niu, C.C., et al., *Outcomes of interbody fusion cages used in 1 and 2-levels anterior cervical discectomy and fusion: titanium cages versus polyetheretherketone (PEEK) cages.* J Spinal Disord Tech, 2010. **23**(5): p. 310-6.

17. Mendenhall, S., *Spinal Industry Update.* 2017. **28**(4): p. 4-6.

18. Vadapalli, S., et al., *Biomechanical rationale for using polyetheretherketone (PEEK) spacers for lumbar interbody fusion-A finite element study.* Spine (Phila Pa 1976), 2006. **31**(26): p. E992-8.

19. Duncan, J.W. and R.A. Bailey, *An analysis of fusion cage migration in unilateral and bilateral fixation with transforaminal lumbar interbody fusion.* European Spine Journal, 2013. **22**(2): p. 439-445.

20. Evans, N.T., et al., *High-strength, surface-porous polyether-ether-ketone for load-bearing orthopedic implants.* Acta Biomater, 2015. **13**: p. 159-167.

21. Eltorai, A.E., E. Nguyen, and A.H. Daniels, *Three-Dimensional Printing in Orthopedic Surgery.* Orthopedics, 2015. **38**(11): p. 684-7.

22. Gibbs, D.M., et al., *Hope versus hype: what can additive manufacturing realistically offer trauma and orthopedic surgery?* Regen Med, 2014. **9**(4): p. 535-49.

23. Martelli, N., et al., *Advantages and disadvantages of 3-dimensional printing in surgery: A systematic review.* Surgery, 2016. **159**(6): p. 1485-1500.

24. Provaggi, E., J.J.H. Leong, and D.M. Kalaskar, *Applications of 3D printing in the management of severe spinal conditions.* Proc Inst Mech Eng H, 2017. **231**(6): p. 471-486.

25. Tack, P., et al., *3D-printing techniques in a medical setting: a systematic literature review.* Biomed Eng Online, 2016. **15**(1): p. 115.

26. Ventola, C.L., *Medical Applications for 3D Printing: Current and Projected Uses.* P t, 2014. **39**(10): p. 704-11.

27. *Medical Additve Manufacturing/3D Printing Annual Report 2018*. 2018: SME.

28. Berretta, S., K. Evans, and O. Ghita, *Additive manufacture of PEEK cranial implants: Manufacturing considerations versus accuracy and mechanical performance.* Materials & Design, 2018. **139**: p. 141-152.

29. Diana, C., et al., *Prototype Orthopedic Bone Plates 3D Printed by Laser Melting Deposition*. Vol. 12. 2019. 906.

30. Honigmann, P., et al., *Patient-Specific Surgical Implants Made of 3D Printed PEEK: Material, Technology, and Scope of Surgical Application*. Vol. 2018. 2018.

31. Basgul, C., et al., *Thermal localization improves the interlayer adhesion and structural integrity of 3D printed PEEK lumbar spinal cages.* Materialia, 2020. **10**: p. 100650.

32. Basgul, C., et al., *Structure-property relationships for 3D printed PEEK intervertebral lumbar cages produced using fused filament fabrication.* J Mater Res, 2018. **33**(14): p. 2040-2051.

33. Basgul, C., et al., *Does annealing improve the interlayer adhesion and structural integrity of FFF 3D printed PEEK lumbar spinal cages?* Journal of the Mechanical Behavior of Biomedical Materials, 2020. **102**: p. 103455.

34. Delaney, L.J., et al., *Acoustic Parameters for Optimal Ultrasound-Triggered Release from Novel Spinal Hardware Devices.* Ultrasound in Medicine & Biology, 2020. **46**(2): p. 350-358.

35. Delaney, L.J., et al., *Ultrasound-triggered antibiotic release from PEEK clips to prevent spinal fusion infection: Initial evaluations.* Acta Biomaterialia, 2019. **93**: p. 12-24.

36. Han, X., et al., *An In Vitro Study of Osteoblast Response on Fused-Filament Fabrication 3D Printed PEEK for Dental and Cranio-Maxillofacial Implants.* Journal of clinical medicine, 2019. **8**(6): p. 771.

37. Prechtel, A., et al., *Fracture load of 3D printed PEEK inlays compared with milled ones, direct resin composite fillings, and sound teeth.* Clinical Oral Investigations, 2020.

38. Wang, L., et al., *Three-Dimensional Printing PEEK Implant: A Novel Choice for the Reconstruction of Chest Wall Defect.* The Annals of Thoracic Surgery, 2019. **107**(3): p. 921-928.

39. Zhang, C., et al., *Bionic design and verification of 3D printed PEEK costal cartilage prosthesis.* Journal of the Mechanical Behavior of Biomedical Materials, 2020. **103**: p. 103561.

40. Kang, J., et al., *Custom design and biomechanical analysis of 3D-printed PEEK rib prostheses.* Biomechanics and Modeling in Mechanobiology, 2018. **17**(4): p. 1083-1092.

41. Liu, D., et al., *Application of 3D-printed PEEK scapula prosthesis in the treatment of scapular benign fibrous histiocytoma: A case report.* Journal of Bone Oncology, 2018. **12**: p. 78-82.

42. Sun, Q., et al., *Effect of processing conditions on the bonding quality of FDM polymer filaments.* Rapid Prototyping Journal, 2008. **14**(2): p. 72-80.

43. Thomas, J. and J. Rodriguez. *Modeling the fracture strength between fused-deposition extruded roads*. in *Solid Freeform Fabrication Symposium Proceeding*. 2000. Austin, TX, USA.

44. Drummer, D., S. Cifuentes-Cuéllar, and D. Rietzel, *Suitability of PLA/TCP for fused deposition modeling.* Rapid Prototyping Journal, 2012. **18**(6): p. 500-507.

45. Xinhua, L., et al., *An investigation on distortion of PLA thin-plate part in the FDM process.* The International Journal of Advanced Manufacturing Technology, 2015. **79**(5): p. 1117-1126.

46. Zhang, Y. and Y. K. Chou, *Three-dimensional finite element analysis simulations of the fused deposition modelling process.* Proceedings of the Institution of Mechanical Engineers, Part B: Journal of Engineering Manufacture, 2006. **220**(10): p. 1663-1671.

47. Basgul, C., et al., *Structure–property relationships for 3D-printed PEEK intervertebral lumbar cages produced using fused filament fabrication.* Journal of Materials Research, 2018: p. 1-12.

48. Sharma, N., et al., *Quality Characteristics and Clinical Relevance of In-House 3D-Printed Customized Polyetheretherketone (PEEK) Implants for Craniofacial Reconstruction.* J Clin Med, 2020. **9**(9).

49. Costa, S.F., F.M. Duarte, and J.A. Covas, *Estimation of filament temperature and adhesion development in fused deposition techniques.* Journal of Materials Processing Technology, 2017. **245**: p. 167-179.

50. Arif, M.F., et al., *Performance of biocompatible PEEK processed by fused deposition additive manufacturing.* Materials & Design, 2018. **146**: p. 249-259.

51. Li, H., et al., *Preparation of high performance adhesives matrix based on epoxy resin modified by bis-hydroxy terminated polyphenylene oxide.* Journal of Adhesion Science and Technology, 2018. **32**(11): p. 1224-1238.

52. Rodriguez, J.F., Thomas, J.P. , Renaud, J.E. *Maximizing the Strength of Fused-deposition ABS plastic parts*. in *10th, Solid freeform fabrication symposium*. 1999. Austin, TX.

53. Yardimci, M.A.G., S.I.; Danford, S.C.; Safari, A., *Numerical modeling of Fused Deposition processing* Proceedings of the ASME Materials Division, 1995. **MD-Vol. 69-2**: p. 1225-1236.

54. Thomas, J. and J. Rodriguez, *Modeling the fracture strength between fused-deposition extruded roads.* Proc. Solid Freeform Fabr. Symp, 2000: p. 16-23.

55. Bellehumeur, C., et al., *Modeling of Bond Formation Between Polymer Filaments in the Fused Deposition Modeling Process.* Journal of Manufacturing Processes, 2004. **6**(2): p. 170-178.

56. Costa, S., F. Duarte, and J. Covas, *Using MATLAB to Compute Heat Transfer in Free Form Extrusion*. 2011.

57. Zhang, J., et al., *Numerical investigation of the influence of process conditions on the temperature variation in fused deposition modeling.* Materials & Design, 2017. **130**: p. 59-68.

58. Ravoori, D., et al., *Experimental and theoretical investigation of heat transfer in platform bed during polymer extrusion based additive manufacturing.* Polymer Testing, 2019. **73**: p. 439-446.

59. Wang, P., B. Zou, and S. Ding, *Modeling of surface roughness based on heat transfer considering diffusion among deposition filaments for FDM 3D printing heat-resistant resin.* Applied Thermal Engineering, 2019. **161**: p. 114064.

60. Compton, B.G., et al., *Thermal analysis of additive manufacturing of large-scale thermoplastic polymer composites.* Additive Manufacturing, 2017. **17**: p. 77-86.

61. Lee, W.I. and G.S. Springer, *A Model of the Manufacturing Process of Thermoplastic Matrix Composites.* Journal of Composite Materials, 1987. **21**(11): p. 1017-1055.

62. Yang, F. and R. Pitchumani, *Healing of Thermoplastic Polymers at an Interface under Nonisothermal Conditions.* Macromolecules, 2002. **35**(8): p. 3213-3224.

63. Yin, J., et al., *Interfacial bonding during multi-material fused deposition modeling (FDM) process due to inter-molecular diffusion.* Materials & Design, 2018. **150**: p. 104-112.

64. Ko, Y.S., et al., *Improving the filament weld-strength of fused filament fabrication products through improved interdiffusion.* Additive Manufacturing, 2019. **29**: p. 100815.

65. Coasey, K., et al., *Nonisothermal welding in fused filament fabrication.* Additive Manufacturing, 2020. **33**: p. 101140.

Chapter 2: Structure, Properties, and Bioactivity of 3D Printed PAEKs for Implant Applications: A systematic review*

2.1 Abstract

Additive manufacturing (AM) of high-temperature polymers, specifically polyaryletherketones (PAEK), is gaining significant attention for medical implant applications. As 3D printing systems evolve towards point-of-care manufacturing, research on this topic continues to expand. Specific regulatory guidance is being developed for the safe management of 3D printing systems in a hospital environment. PAEK implants can benefit from many advantages of additive manufacturing such as design freedom, material, and antibacterial drug incorporation, and enhanced bioactivity provided by cancellous bone-like porous designs. In addition to AM PAEK bioactivity, the biomechanical strength of 3D printed implants is crucial to their performance and thus widely studied. In this review, we discuss the printing conditions that have been investigated so far for additively manufactured PAEK implant applications. The effect of processing parameters on the biomechanical strength of implants is summarized, and the bioactivity of PAEKs, along with material and drug incorporation, is also covered in detail. Finally, the therapeutic areas in which 3D printed PAEK implants are investigated and utilized are reviewed.

---

* The content of this chapter is under review in the Journal of Biomedical Materials Research: Part B – Applied Biomaterials: Basgul, C., Spece, H., Sharma, N., Thieringer, F.M., Kurtz, S.M. Structure, Properties, and Bioactivity of 3D Printed PAEKs for Implant Applications: A systematic review. *Under review.* Submitted 08 September 2020.

2.2 Introduction

As the precision and reliability of additive manufacturing (AM) advance, 3D printing of high-temperature polymers is gaining increasing attention for biomedical applications, especially for production in a hospital setting [1-3]. Polyetheretherketone (PEEK) and polyetherketoneketone (PEKK), two members of the polyaryletherketone (PAEK) family, have been increasingly investigated using AM, with the ultimate goal of providing personalized treatments by developing techniques suitable for implant applications [4-6]. Unlike AM of metallic biomaterials such as Ti-6Al-4V alloy, which have been extensively researched in the past two decades [7], AM techniques for PAEKs have emerged only recently, and considerably less is known about the structure-property relationships and suitability for implantation of AM PAEK. Several factors have driven the recent interest in AM PAEK for implants, including the possibility of fabricating patient-specific implants (PSIs) that meet the complex anatomical structural requirements at the implantation site, the desire to fabricate porous polymeric scaffolds that better match the biomechanical milieu, and the enthusiasm among clinicians to develop patient-centric implant solutions at the point of care (POC).

The advancements in AM have revolutionized the practice of modern medicine, leading to a paradigm shift in healthcare. For reconstructive surgeries, clinicians have continuously aimed to improve surgical outcomes with the use of prefabricated implants. Yet, these implants provide limited solutions in addressing patient-specific complexities [8, 9]. Customized implants, on the other hand, are designed to fit precisely in the patient's anatomical defects or malformations [10]. In the future, POC AM as an advanced technology will allow individualized reconstruction in such complex cases considering its high adjustability, cost-effectiveness, and shorter lead time, which is crucial for trauma cases or other time-critical medical interventions and not feasible with traditional manufacturing methods [11]. At present, there remain procedural challenges with PSIs, as well as unresolved regulatory considerations for POC manufacturing. Additionally, research for improving the additive processing of high-temperature polymers for PSIs is ongoing [12, 13].

Furthermore, specific design criteria in current PAEK implants are desirable, such as interconnected porous structures to improve its bioactivity [14, 15]. Porous surfaces of PEEK are shown to be more attractive for cells than untextured machined PEEK and provide promising results for further design alterations of PAEK implants [16]. However, for porosity implemented via traditional methods, it is not feasible to control the porous design (e.g. porous geometry, pore size, and interconnectivity). AM opens the door to new possibilities by providing the design freedom, in addition to other advantages, to create tunable porosity for various implant applications [17].

Currently, fused filament fabrication (FFF) technology, the most accessible AM method, is already implemented in the hospitals for the fabrication of anatomical bio-models, customized surgical instruments, and prosthetic aids [18, 19]. While these applications have typically been achieved with low-temperature polymers, recent technological advancements in FFF 3D printers have made it possible to process high-temperature thermoplastic materials such as PAEK. As a consequence, FFF 3D printers are currently being developed specifically for medical PAEK applications and POC manufacturing. In response to growing interest in POC AM, both the US and EU released guidelines and regulations for additively manufactured medical devices in 2017 [20, 21]. Per these regulations, specific operational and regulatory standards should be established at the POC to assess whether a fabricated PSI conforms to the intended clinical use. Furthermore, standard organization-based certification processes relating to quality management protocols for the 3D printer, as well as for the design planning of the PSIs, should be integrated into the hospital environment. With a clear regulatory pathway, 3D printer companies have been working towards fulfilling these guidelines for POC AM. Certification is required for the entire manufacturing process including data acquisition, further processing to packaging, and the traceability of the finished implant. For instance, after the fabrication of implants using a 3D printer at the POC, on-site sterilization must be undertaken as one part of this entire process. One company has even developed a printer integrated into a cleanroom environment to help this process monitoring [22].

As interest in the POC fabrication of PAEK implants grows, it is increasingly important to summarize the state of knowledge as it continues to expand and evolve. We would like to direct the reader to previous reviews of PEEK in a biomedical context [23, 24], which provide an overview of AM techniques and explain the differences between the two principal technologies for AM PAEKs: fusion of polymer powder, such as selective laser sintering (SLS), or consolidation of extruded layers, known as FFF. The reader is referred to previous reviews for further explanation of SLS and FFF

[23, 24]. In the present review, we address the factors affecting the structure, biomechanical properties, and bioactivity of 3D printed PEEK/PEKK for implant applications. We, therefore, sought to address the following questions: (1) Under what printing conditions have PAEKs been printed for implants; (2) What are the strength limitations for AM PAEKs; (3) Has AM PAEK been evaluated *in vitro* and *in vivo*; and (4) In what therapeutic areas has AM PAEK been used clinically in humans?

2.3 Materials and Methods

The Preferred Reporting Items for Systematic Reviews and Meta-Analyses (PRISMA) guidelines were used for this manuscript [25]. Two different databases were utilized to perform searches to identify research articles that investigated the bioactivity and biomechanical properties of additively manufactured PEEK/PEKK for biomedical implants. Sources dated between May 2005 and May 2020, and the search was performed on May 27, 2020. The following keywords were separately searched in the SCOPUS database: Keyword combination 1 was (“peek" OR "polyetheretherketone") AND ("additive manufacturing" OR "three-dimensional printing" OR “3D printing”), and keyword combination 2 was ("peek" OR "polyetheretherketone") AND ("medical" OR "biomedical") AND ("3dprinting") OR ("additive manufacturing" OR "three-dimensional printing"). The second search was conducted through following databases using ProQuest: Biotechnology Research Abstracts, Ei Compendex®, Embase®, Engineered Materials Abstracts, FDAnews, Inspec®, MEDLINE®, NTIS: National Technical Information Service, and SciSearch®. The following keywords were separately searched in these databases: Keyword combination 1 was ("Polyetheretherketone" OR "PEEK" OR "polyaryletherketone") AND ("additive manufacturing" OR "3D Printing" OR "fused deposition modeling" OR stereolithography OR "selective laser sintering" OR "3-D Printing"), and keyword combination 2 was ("Polyether ether ketone" OR "PEEK" OR "polyaryletherketone") AND ("additive manufacturing" OR "3D Printing" OR "fused deposition modeling" OR stereolithography OR "selective laser sintering" OR "3-D Printing" OR "three-dimensional printing") AND ("medical" OR "biomedical").

There were 175 and 47 results from keyword combinations 1 and 2, respectively, from SCOPUS, and 469 and 277 results from keyword combinations 1 and 2, respectively, from the remaining databases. 533 studies were selected to screen after the removal of duplicates and unrelated records (n=435). Review articles, abstracts, conference proceedings, and non-English articles were excluded from the study as well (n=235). 298 studies were assessed carefully to include in the review The inclusion criteria were: (1) studies that additively manufactured PAEK medical implants; (2) studies that investigated either 3D printed PEEK or PEKK for future implant applications; (3) studies examining biomechanics, bioactivity via *in vitro* or *in vivo* response, and/or material properties of AM PAEK. The exclusion criteria were: (1) studies not involving PEEK/PEKK; (2) studies in which PEEK/PEKK was not additively manufactured; and (3) studies in which PEEK/PEKK was not 3D printed specifically for an implant application or for *in vivo* implantation within the study. 258

of the assessed studies were rejected using these exclusion criteria, resulting in a selection of 40 articles for inclusion in this review (Fig. 2.1).

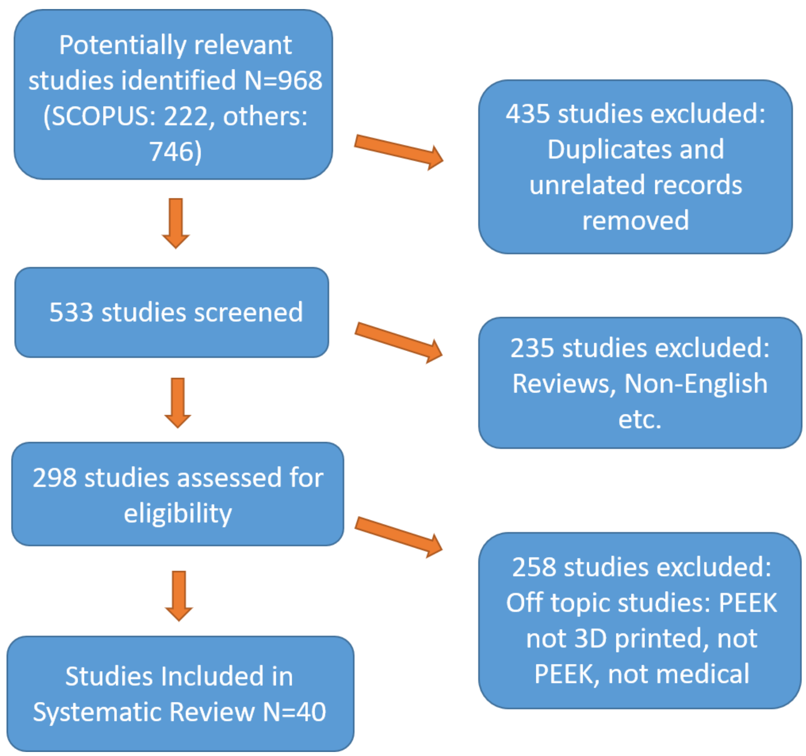

Figure 2. 1. PRISMA flowchart showing the steps of the article selection process with numbers of included and excluded articles.

To answer the research questions, the data extracted from the papers were carefully selected. The definitions of each data type extracted from the table are explained in detail in Table 2.1., and a schematic of the printing parameters is provided in Figure

2.2. To further describe the printing conditions of the reviewed studies, PAEK materials may be classified as “industrial” or “medical” grade, with the latter denoting that the material meets certain regulatory criteria to ensure quality and biocompatibility. Similarly, printers are denoted as “industrial” or “medical”, depending on whether the system can provide a sterile printing environment. Mechanical test data presented only in graphs were extracted via WebPlotDigitizer [26].

Table 2. 1. Data extracted from the papers.

Term	Definition
3D Printing Conditions	
PAEK Material	Material (in either filament, powder, or granule form) used to 3D print
Filament/Powder Producer	PAEK material manufacturer
Printer Brand	3D printer brand
Build volume (mm^3)	Maximum size of the implant that can be printed. Reported as length x width x height except for cylindrical build volume (diameter x length)
Laser power (W)	Power of the laser used to sinter the powdered material for SLS
Spot Diameter (mm)	Radius of the laser beam for SLS
Hatch Distance (mm)	Separation between the two consecutive laser beams for SLS also referred to as scan spacing
Nozzle Temperature (℃) (Tn)	Temperature at which material is extruded for FFF
Print bed temperature (℃) (Tb)	Temperature of the heated build platform for FFF
Environment temperature (℃) (Te)	Enclosed environment/chamber temperature for FFF
Cooling temperature (℃) (Tc)	Temperature of environment that is ensured via cooling of the chamber for FFF

Nozzle Diameter (mm)	Diameter of the extruder where the material is extruded for FFF
Layer height (mm)	Height of each deposited layer or powder stack
Print speed/Scanning speed (mm/s)	Speed of the laser and/or extruder
Structural Properties	
3D printed specimen	3D printed parts printed in the study
Undesired porosity (%)	Porosity measured post-printing for 100% infill part
Designed porosity (%)	Designed porosity percentage of the 3D printed part
Actual porosity (%)	Measured porosity percentage of the porous designed 3D printed part
Post-processing properties	
Annealing	Heat treatment of the 3D printed part to remove internal stresses
Thermocycling	Aging protocol of exposing materials to similar temperatures in the body
Autoclaving	Sterilization method via high-pressure steam for healthcare applications
Mechanical Properties	
Compressive strength (MPa)	Ultimate strength value from the stress/strain curve under compression
Tensile strength (MPa)	Ultimate strength value from the stress/strain curve under tension
Ultimate force (Maximum Load) (N)	Highest load achieved before failure
Push-out Force (N)	Maximum load achieved while push out testing the 3D printed scaffold/implant implanted in bone
Martens hardness (MPa)	Hardness value of the sample calculated under compressive load
Biocompatibility Properties	
In vivo vs. in vitro	Research conducted on a living organism vs. cell culture
Medium	Cell and/or animal type used in studies
Material blend	Materials used for incorporation along with PEEK/PEKK
Bioactivity	Activity to promote cell viability, adhesion, and differentiation
Antibacterial activity	Activity to provide adequate protection against bacteria without disruption of host tissue
Osseointegration	Structural and functional connection between the implant surface and bone

2.4 Results

2.4.1 Printing conditions

For the 40 studies reviewed, we found that FFF as an AM method is used more frequently (62.5%, n = 25/40) than SLS (37.5%, n=15/40) (Fig. 2.2). Studies were categorized by the two methods (Table 2.2 for FFF and Table 2.3 for SLS). A majority of studies used PEEK (92%, n=23/25 for FFF and 93.3%, n=14/15 for SLS) compared to PEKK (8%, n=2/25 for FFF and 6.7%, n=1/15 for SLS).

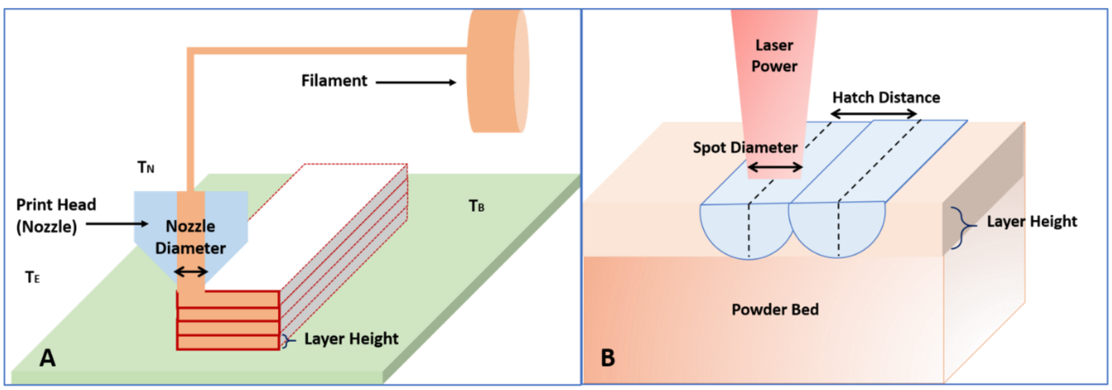

Figure 2. 2. Printing parameters extracted from papers for both FFF (a) and SLS systems (b).

For FFF studies, industrial-grade filaments (62%, n = 18/29) are used more often than medical-grade filaments (38%, n=11/29). A large amount of studies used industrial printers (62.5%, n = 15/24), followed by self-developed (16.7%, n = 4/24), upgraded low temperature printers (12.5%, n = 3/24), and medical (8.3%, n = 2/24). Build volume for FFF printers ranged between 145 x 135 x 148 mm³ to 454 x 454 x

650 mm³. The nozzle temperature ranged from 340°C to 485°C. Print bed temperature was chosen between 100°C and 250°C. Finally, environment/chamber temperatures ranged from 20°C to 200°C. Nozzle diameters used in the studies were between 0.2 and 0.6 mm, where a 0.4 mm nozzle was most common (80%, n = 16/20). Layer height was chosen as between 0.05 -0.3 mm. Extruder speed for FFF studies ranged from 5 to 50 mm/s.

For SLS studies as for FFF studies, medical grade powder (8.3%, n = 1/12) was used less frequently compared to industrial grade powder (91.7%, n = 11/12). 3D printers used in SLS studies were mostly in-house built (45.5%, n = 5/11), followed by industrial printers (45.5%, n = 5/11) and a modified printer (9%, n = 5/11). The highest build volume indicated for SLS printers is 700 x 380 x 560 mm³. Laser power reported in the SLS studies varied from 1.9-28 Watts. Spot diameter for SLS studies varied from 0.4 to 3.5 mm, with the most common diameter being 0.8 mm (50%, n = 3/6). The layer height reported in SLS studies was 0.1- 0.2 mm (62.5%, n = 5/8), 0.15 mm (12.5%, n = 1/8), 0.12 mm (12.5%, n = 1/8) and 0.1 mm (12.5%, n = 1/8). The printing speed ranged from 2.1 to 5080 mm/s.

For SLS studies, a majority of studies used porous designs (86.7%, n = 13/15) (Fig. 2.3) compared to solid designs (13.3%, n = 2/15), and none of the studies measured the undesired porosity. For FFF studies, a majority of studies examined solid designs (76%, n = 19/25), and undesired porosity was measured in five studies (20%, n = 5/25). Annealing (6.7%, n = 1/15) was the only mentioned post-processing method for SLS papers, whereas for FFF annealing (16%, n = 4/25) was followed by autoclaving (4%, n = 1/25) and thermocycling (4%, n = 1/25).

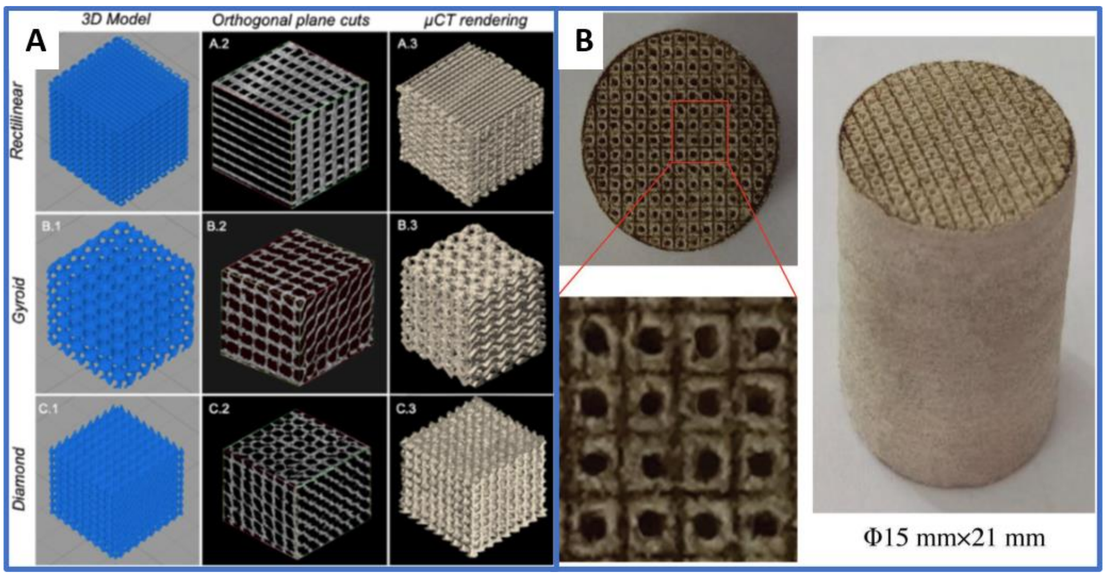

Figure 2. 3. Porous designs manufactured via 3D printing are shown to improve the bioactivity of PAEK. (A) Porous PEEK was created via FFF, reprinted from Spece et al. [17] with permission from Elsevier. (B) Porous PEEK/β-TCP/PLLA created via SLS, reprinted from Feng et al. [27] with permission John Wiley and Sons.

Table 2. 2. Printing conditions to additively manufactured PAEK via Fused Filament Fabrication.

Study	PAEK Material	Filament Producer	Printer Brand	Build Volume (mm^3)	Processing temperatures* (℃)	Nozzle Diameter (mm)	Layer height (mm)	Print Speed (mm/s)	3D Printed Specimen	Porosity (%)	Post Processing
Basgul 2020 [28]	PEEK OPTIMA™ LT1	Invibio	Indmatec HPP155	145 x 135 x 148	Tn:390-410 Tb:100	0.4	0.1	25 33.3	Spinal Cage	Undesired 2.85-4.26	Annealing 200℃ & 300℃ 4 hours℃
Basgul 2020 [29]	450G™	Victrex ™	Indmatec HPP155	145 x 135 x 148	Tn:390-410 Tn:100	0.4	0.1	25 41.6	Spinal Cage	Undesired 0.43-2.24	-
			Apium P220	205 x 155 x 150	Tn:485 Tb:130	0.4 0.2	0.1-0.2 0.05-0.1				
Cheng 2020 [30]	TETRAfuse®PEKK	RTI Surgical	-	-	-	-	-	-	Cylindrical Implants	-	-
Cheng 2020 [6]	PEKK Filament	-	Indmatec HPP155	145 x 135 x 148	-	-	-	-	Mandibular reconstruction part	-	-
Delaney 2020 [31]	PEEKMed	Apium	Indmatec HPP155	145 x 135 x 148	Tn:405 Tb:100	0.4	0.1	25 [32]	Spinal Clips	-	-

Elhattab 2020 [33]	450G™	Victrex ™	AON-M2	454 x 454 x 640	Tn:390 Tb:110	-	-	25	Porous PEEK structures	Designed 50 40 30 0	-
Lau 2020 [34]	PEEK filament	Huaian Ruanke Trade Co.	Black Magic 3D Prusa i3 (modified)	250 x 210 x 200	Tn:340	0.6	-	-	Circular Disks	-	-
Petersmann 2020 [35]	KetaSpire® PEEK	Solvay	SpiderBot 4.0 HT	200 x 200 x 180	Tn:427 Tb:160 Te:90	0.5	0.25	20	Adjusted dog-bone	Undesired 1.18	-
Prechtel 2020 [36]	Essentium PEEK KetaSpire® PEEK MS-NT1 VESTAKEEP® i4 G 450G™	Essentium Solvay Victrex ™ Evonik	HTRD1.2 Kumovis	CBD* 170 x 100	Tn:390 Tb:220 Te:100 Tc:120	0.4	0.15	5	Dental Inlays	-	-
Prechtel 2020 [37]	Essentium PEEK KetaSpire® PEEK MS-NT1	Essentium Solvay Victrex ™ Evonik	HTRD1.2 Kumovis	CBD* 170 x 100	Tn:410 Tb:250 Te:200	0.4	0.1 0.15 0.2 0.3	10 15 20	Rectangular cuboid	-	Thermocycling 5-55℃ 10000 cycles Autoclaving 134 ℃ 2 bars

	VESTA KEEP® i4 G 450G™										
Spece 2020 [17]	450G™	Victrex ™	Apium P220	205 x 155 x 150	Tn:420-450	0.2	0.1	37	Porous Scaffolds	Designed 70-74 Actual 68-70	-
Su 2020 [38]	Medical Grade	Shaanxi Jugsao-AM	Jugao-AM Tech. Corp. (unspecified model)	-	Tn:430	0.4	0.2	40	Porous PEEK structures	-	Annealing 200℃ & 300℃ 1.5 hours
Zhang 2020 [39]	450G™	Victrex ™	Self-developed	-	Tn:420	0.4	0.2	40	Costal Cartilage Prosthesis	-	-
Delaney 2019 [32]	PEEKMed	Apium	Indmatec HPP155	145 x 135 x 148	Tn:405 Tb:100	0.4	0.1	25	Spinal Clips Porous Pucks	Designed Spinal Clips 38 Porous Pucks N/A	-
Han 2019 [40]	450G™	Self-produced from granules	Jugao-AM Tech. Corp. (unspecified model)	-	Tn:420 Te:20	0.4	0.2	40	TS (ISO 527-1) and Cuboid specimen (ISO 178)	-	Annealing 300℃ 2 hours℃

Han 2019 [41]	VESTA KEEP® i4 G	Evonik	Apium P220	145 x 135 x 148	Tn:480 Tb:130	0.4	0.2	-	Disk samples	-	-
Jung 2019 [42]	450G™	Self-produced from granules	Self-developed	-	Tn:400 Te:160	0.4	0.2	20	Disk-shaped and screw-shaped samples & TS	-	-
Wang 2019 [3]	PEEK OPTIMA™ LT1*	Invibio	Jugao-AM-Tech. Corp. (unspecified model)	-	Tn:340	-	-	-	Chest wall reconstruction implants	-	-
Basgul 2018 [43]	PEEK OPTIMA™ LT1	Invibio	Indmatec HPP155	145 x 135 x 148	Tn:390-410 Tb:100	0.4	0.1	16.6 25 33.3 50	Spinal Cage	Undesired 2 - 20	-
Honigmann 2018 [1]	Apium PEEK (Medical Grade)	Apium	Apium P220	145 x 135 x 148	Tn:400 Tb:100	0.4	0.1-0.3	-	Various patient specific implants	-	-
Kang 2018 [2]	-	-	Self-developed	-	Tn:420	0.4	0.2	40	Rib Prosthesis	-	-
Liu 2018 [44]	-	-	-	-	-	-	-	-	Scapula Prosthesis	-	-
Zhao 2018 [45]	450G™	Self-produced from	Self-developed	-	Tn:375 Tb:270 Te:170	0.4	0.2	30	Blocks (25*10*15 mm³)	-	-

		granules			Tn:355-375 Tb:230-270 Te:130-170				Dog Bone Specimen (1BA type ISO527)		
Deng 2017 [46]	450G™	Victrex ™	Indmatec HPP155	145 x 135 x 148	Tn:380	-	-	-	Porous PEEK structures	-	-
Vaezi 2015 [47]	450G™	Victrex ™	UP 3D Printer (Modified)	-	Tn:410 Tb:110 Te:80	0.4	0.2	-	Porous PEEK structures TS	Designed 38 Undesired 14	Annealing 200℃ 4 hours℃

*CBD: Cylindrical Build Volume, Processing Temperatures: Tn: Nozzle Temperature, Tb: Print Bed Temperature, Te: Environment/chamber Temperature, Tc: Cooling Temperature, TS: Tensile Specimen, Wang et al.[3]'s study material is indicated as surgical-grade provided from Victrex.

Table 2. 3. Printing conditions to additively manufactured PAEK via Selective Laser Sintering.

Study	PAEK Material	Powder Producer	Printer Brand	Build Volume (mm³)/Scan area (mm²)	Laser Power (W)	Spot Diameter (mm)	Hatch Distance (mm)	Layer height (mm)	Scanning Speed (mm/s)	3D Printed Specimen	Porosity (%)	Post-Processing
Feng 2020 [48]	PEEK Powder	Dongguan Guanhui Plastic Materials	N/A	-	2.2	0.4	0.95	0.1-0.2	2.5	Porous PEEK/PVA-GO & Porous PEEK/PVA structures	-	-
Wu 2020 [49]	PEEK Powder	Dongguan Guanhui Plastic Materials	Self-developed	-	2	-	0.1	-	150	TASS-PEEK/PGA porous scaffolds	-	-
Berretta 2018 [50]	PEEK OPTIMA ™ LT1	Invibio	EOSINT P 800	700 x 380 x 560	15	-	0.2 [51]	-	1000-2250 [51]	Porous Cranial Implants	-	-
Feng 2018 [27]	PEEK Powder	Dongguan Guanhui Plastic Materials	N/A	-	-	0.5	0.95	0.1-0.2	120	PEEK/β-TCP/PLLA porous scaffolds	-	-
Shishkovsky 2018 [52]	PEEK Powder	Victrex™	N/A	50 x 50 or 100 x 100 [53]	1.9-10.7 [54]	1-3.5 [54]	-	-	2.1-720 [54]	Dog bone & cuboid specimen	-	Annealing 150℃ 1 hour

Shuai 2018 [55]	PEEK Powder	Dongguan Guanhui Plastic Materials	Self-developed	-	-	-	-	-	-	TiO_2-PEEK/PGA scaffolds	-	-
Zhong 2018 [4]	-	-	China are 3D	-	-	-	-	-	-	Porous PEEK Cranial Implant	-	-
Roskies 2017 [56]	OXPEKK	Oxford Performance Materials	EOSINT P 800	-	-	-	-	-	-	PEKK/ADSC scaffolds for mandibular defects	Design ed 50	-
Shuai 2017 [57]	PEEK Powder	Dongguan Guanhui Plastic Materials	Self-developed	-	2.5	0.8	3	0.1-0.2	6.67	PEEK/PGA–DIOP & PEEK/PGA–KDIOP scaffolds	-	-
Roskies 2016 [58]	-	-	EOSINT P 800	700 x 380 x 560	-	-	-	0.12	-	Porous PEEK Structures	Design ed 36	-
Shuai 2016 [59]	PEEK Powder	Dongguan Guanhui Plastic Materials	Self-developed	-	2.5	0.8	3	0.1-0.2	6.67	PEEK/PGA-HAP porous scaffolds	Design ed 48.9	-
Shuai 2016 [60]	PEEK Powder	Dongguan Guanhui Plastic Materials	Self-developed	-	-	0.8	2.5	0.1-0.2	6.67	PEEK/PGA porous scaffolds	-	--
El Halabi 2011 [5]	-	-	EOSINT P 800	700 x 380 x 560	-	-	-	-	-	Dog bone specimen & Porous Cranial Implants	-	-

von Wilmowsky 2008 [61]	PEEK™ 150 PF	Victrex™	Modified EOSINT P 380	340 x 340 x 620	10	-	0.2	0.15	4500	PEEK w carbon/β-TCP/Bioglass disks	-	-
Tan 2005 [62]	PEEK™ 150XF	Victrex™	-	-	9-28	-	-	0.1	5080	Porous PEEK/HA scaffolds	Designed 69.9-73.5	-

2.4.2 Biomechanical Strength of AM PAEKs

In the previous section, the parameters used in PAEK printing were explained in detail for both SLS and FFF systems. This section summarizes the available literature regarding the strength limitations of AM PAEK. 29 papers mechanically tested specimens under either static compression (58.6%, n = 17/29) or tensile (41.4%, n = 12/29) loading conditions (Table 2.4, Fig. 2.4).

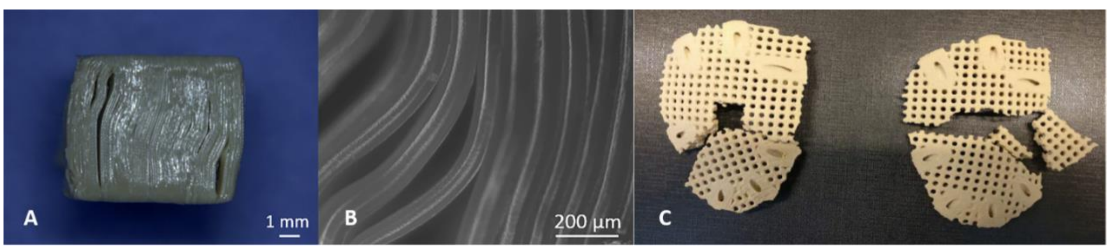

Figure 2. 4. The failure mechanism is mentioned as layer debonding for FFF spinal implants (a-b), reprinted from Basgul et al. [43] with permission from Elsevier, whereas brittle fractures are observed for SLS cranial implants under compression loading conditions (b), reprinted from Berretta et al. [50] with permission from Elsevier.

None of the studies included investigated fatigue testing. The most frequent outcome measured from mechanical tests was tensile strength (41.4%, n = 12/29), followed by compressive strength (27.6%, n = 8/29), maximum load (24%, n = 7/29), push-out force (3.5%, n = 1/29) and Martens hardness (3.5%, n = 1/29). Notably, there was a variety of factors that affect the biomechanical outcomes of the 3D printed parts, including tested specimen size/shape, material, AM method, testing method, extrusion temperature [42, 45], print speed [37, 43], part orientation [37, 50], and nozzle diameter [29].

Table 2. 4. Studies conducted mechanical testing on AM PAEK.

Study	AM method	Material	Specimen	Loading Condition	Outcome Measured	Value
Feng 2020 [48]	SLS	PEEK/PVA-GO & PEEK/PVA	Porous Scaffold	Compression	Compressive Strength (MPa)	10.1-20.1
Berretta 2018 [50]	SLS	PEEK	Porous Cranial Implant	Compression	Maximum Load (N)	336-794
Feng 2018 [27]	SLS	PEEK/β-TCP/PLLA	Porous Scaffold	Compression	Compressive Strength (MPa)	17-34
Shishkovsky 2018 [52]	SLS	PEEK	Dog-bone	Tensile	Tensile Strength (MPa)	6-37
Shuai 2018 [55]	SLS	$nTiO_2$-PEEK/PGA	Porous Scaffold	Compression	Compressive Strength (MPa)	38-51
Roskies 2017 [56]	SLS	PEKK/ADSC	Porous Scaffold	Compression	Maximum Load (N)	3003
Shuai 2017 [57]	SLS	PEEK/PGA–DIOP & PEEK/PGA–KDIOP	Porous Scaffold	Compression	Compressive Strength (MPa)	25-38
Shuai 2016 [59]	SLS	PEEK/PGA-HAP	Porous Scaffold	Compression	Compressive Strength (MPa)	19-38
				Tensile	Tensile Strength (MPa)	71-95
Shuai 2016 [60]	SLS	PEEK/PGA	Porous Scaffold	Compression	Compressive Strength (MPa)	34-46
				Tensile	Tensile Strength (MPa)	56-102
El Halabi 2011 [5]	SLS	PEEK	Dog-bone	Tensile	Tensile Strength (MPa)	76
			Porous Cranial Implant	Compression	Maximum Load (N)	608-1028

Basgul 2020 [28]	FFF	PEEK	Spinal Cage	Compression	Maximum Load (N)	7323-7625
Basgul 2020 [29]	FFF	PEEK	Spinal Cage	Compression	Maximum Load (N)	7016-11670
Cheng 2020 [6]	FFF	PEKK	Cylindrical Implants	Compression	Push-out Force (N)	2820
Petersmann 2020 [35]	FFF	PEEK	Dog-bone	Tensile	Tensile Strength (MPa)	60-66
Prechtel 2020 [36]	FFF	PEEK	Dental Inlays	Compression	Maximum Load (N)	1062-1800
Prechtel 2020 [37]	FFF	PEEK	Rectangular cuboid	Compression	Martens Hardness (MPa)	102-185
Spece 2020 [17]	FFF	PEEK	Porous Scaffold	Compression	Compressive Strength (MPa)	6.6-17.1
Su 2020 [38]	FFF	PEEK	Porous Scaffold	Compression	Compressive Strength (MPa)	23
Zhang 2020 [39]	FFF	PEEK	Cartilage Implant	Tensile	Tensile Strength (MPa)	0.7-8.3
Han 2019 [40]	FFF	PEEK	Dog-bone	Tensile	Tensile Strength (MPa)	95
	FFF	CFR-PEEK				101
Jung 2019 [42]	FFF	PEEK	Dog-bone	Tensile	Tensile Strength (MPa)	84.1
Wang 2019 [3]	FFF	PEEK	Cartilage Implant	Tensile	Tensile Strength (MPa)	89
Basgul 2018 [43]	FFF	PEEK	Spinal Cage	Compression	Maximum Load (N)	7856-8964
Zhao 2018 [45]	FFF	PEEK	Dog-bone	Tensile	Tensile Strength (MPa)	45-67
Vaezi 2015 [47]	FFF	PEEK	Dog-bone	Tensile	Tensile Strength (MPa)	75.1
			Porous Scaffold	Tensile	Tensile Strength (MPa)	29.3

Seven studies in total (17.5%, n = 7/40) tested dog-bone specimens in order to investigate the material properties of 3D printed PEEK (Table 2.5). We found a variety of guidelines followed (American Society for Testing and Materials (ASTM) or

International Organization for Standardization (ISO)) and dog-bone specimen dimensions.

Table 2. 5. Studies tested the mechanical properties of the material for both SLS and FFF technologies.

	AM method	Material	Dimensions or Standard number	Tensile Strength (MPa)
Shishkovsky 2018 [52]	SLS	PEEK	6 mm² sectional area, 3 mm length	37
El Halabi 2011 [5]	SLS	PEEK	ASTM D638	76
Petersman 2020 [35]	FFF	PEEK	ISO 527-1A (shortened 10 mm)	60-66
Han 2019 [40]	FFF	PEEK	ISO 527-1A	95
Jung 2019 [42]	FFF	PEEK	ASTM D638-1	84
Zhao 2018 [45]	FFF	PEEK	ISO 527-1BA	45-67
Vaezi 2015 [47]	FFF	PEEK	60 x 4.5 x 3 mm³	75.1

2.4.3 Biocompatibility response of PAEKs

There are six (24%, n= 6/25) and three (20%, n = 3/15) *in vivo* FFF studies and SLS articles, respectively (Table 2.6). Six studies (15%, n= 6/40) used animal models, specifically rabbits (83%, n = 5/6) and sheep (83%, n = 1/6). Human implant studies (7.5%, n= 3/40) can be found in the next section. Eight (32%, n= 8/25) and 11 (73.3%, n= 11/15) studies were *in vitro* studies for FFF and SLS AM PEEK/PEKK, respectively. Among *in vitro* studies, human cell lines were used the most (63.2%, n = 12/19), followed by mouse (26.3%, n = 5/19), rat (5.3%, n = 1/19) and bacteria (5.3%, n = 1/19) cell lines. Among all *in vivo* and *in vitro* studies 15 studies incorporated materials into PEEK/PEKK (62.5%, n = 15/24), whereas 10 of them studied pure PEEK/PEKK (41.7%, n = 10/24). There are two *in vitro* studies in which an antibacterial drug was incorporated into the PEEK (10.5%, n = 2/19) [34, 49], and one *in vivo* study in which rabbit ADSCs were seeded prior to implantation (11.1%, n = 1/9) [56]. All *in vitro* studies investigated bioactivity via several methods such as cell proliferation, adhesion, viability, differentiation, and morphology except for one study conducting only antibacterial activity [34]. In total, four studies conducted additional antibacterial activity assessments (21.1%, n = 4/19). Among these four, three studies examined gram-positive and gram-negative bacteria, with the remaining study experimenting only with the gram-positive bacteria.

Table 2. 6. Summary of *in vivo* and *in vitro* AM PAEK studies.

Study	**AM method**	**Material***	***In vivo* vs *in vitro***	**Test medium***	**Assessment**
Feng 2020 [48]	SLS	PEEK/PVA & PEEK/PVA-GO	*in vitro*	MG63 cells	Bioactivity
			in vivo	Rabbit	
Wu 2020 [49]	SLS	PEEK/ TASS/PGA	*in vitro*	hFOB1.10 cells	Bioactivity & Antibacterial activity
				S. aureus & E. coli	
Feng 2018 [27]	SLS	PEEK/βTCP/PLLA	*in vitro*	MG63 cells	Bioactivity
			in vivo	Rabbit	

Shishkovsky 2018 [52]	SLS	PEEK/TiO_2/Al_2O_3/ZrO_2	*in vitro*	h-MSC	Bioactivity
Shuai 2018 [55]	SLS	PEEK/PGA/ TiO_2	*in vitro*	MG63 cells	Bioactivity & Antibacterial activity
				S. aureus & E. coli	
Roskies 2017 [56]	SLS	PEEK/ADSC	*in vivo*	Rabbit	Osseointegration
Shuai 2017 [57]	SLS	PEEK/PGA–DIOP & PEEK/PGA–KDIOP	*in vitro*	MG63 cells	Bioactivity
Roskies 2016 [58]	SLS	PEEK	*in vitro*	Rat BMSC & ADSC	Bioactivity
Shuai 2016 [59]	SLS	PEEK/PGA-HA	*in vitro*	MG63 cells	Bioactivity
Shuai 2016 [60]	SLS	PEEK/PGA	*in vitro*	MG63 cells	Bioactivity
von Wilmowsky 2008 [61]	SLS	PEEK w carbon/β-TCP/Bioglass disks	*in vitro*	hFOB1.10	Bioactivity
Tan 2005 [62]	SLS	PEEK/HA	*in vitro*	Human fibroblasts	Bioactivity
Cheng 2020 [30]	FFF	PEKK	*in vivo*	Sheep	Osseointegration
Elhattab 2020 [33]	FFF	PEEK	*in vitro*	MC3T3-E1 cells	Bioactivity
Lau 2020 [34]	FFF	PEEK/ampicillin/vancomycin	*In vitro*	S. aureus	Antibacterial activity
Spece 2020 [17]	FFF	PEEK	*in vitro*	MC3T3-E1 cells	Bioactivity
Su 2020 [38]	FFF	PEEK	*in vivo*	Rabbit	Osseointegration
Han 2019 [40]	FFF	PEEK & CFR PEEK	*in vitro*	L929 cells	Bioactivity
Han 2019 [41]	FFF	PEEK	*in vitro*	SAOS-2 cells	Bioactivity
Jung 2019 [42]	FFF	PEEK & PEEK/Ti	*in vitro*	MG63 cells	Bioactivity
			in vivo	Rabbit	Osseointegration
Wang 2019 [3]	FFF	PEEK	*in vivo*	Human	Implantation
Kang 2018 [2]	FFF	PEEK	*in vivo*	Human	Implantation

Liu 2018 [44]	FFF	PEEK	*in vivo*	Human	Implantation
Zhao 2018 [45]	FFF	PEEK	*in vitro*	L929 cells	Bioactivity
Deng 2017 [46]	FFF	PEEK/AgNP	*in vitro*	MG63 cells S. aureus & E. coli	Bioactivity & Antibacterial activity

*Please refer to the abbreviations section for the material open forms and cell line explanations.

2.4.4 Therapeutic areas for AM PAEK

AM PEEK/PEKK for spinal implants were evaluated in 6 studies in which FFF was the AM method for all [28-32, 43] (Fig. 2.5). Specifically, intervertebral devices (n=3) [28, 29, 43], spinal clips designed for spinal fusion infection (n=2) [31, 32] and cylindrical implants (n=1) [30] were evaluated in these 6 studies. Furthermore, AM PEEK/PEKK was investigated for craniomaxillofacial (CMF) implants and reconstructions in 6 studies [4, 6, 41, 50, 56, 58]. Mandibular implant (n=1) [6] , cranial implants (n=2) [4, 50], disk samples (n=1) [41], and porous scaffolds (n=2) [56, 58] were printed in these 6 studies via both SLS and FFF. In total, 4 studies investigated AM PAEKs for dental applications. Of these studies, 2 printed cuboids [37, 40], one used disk samples and indicated the possibility for dental applications [41], and one printed dental inlays [36]. There are 4 studies that explored FFF PAEKs for chest wall reconstruction, which included anterior chest wall construction [3], costal cartilage [39], rib [2], and scapula prosthesis [44].

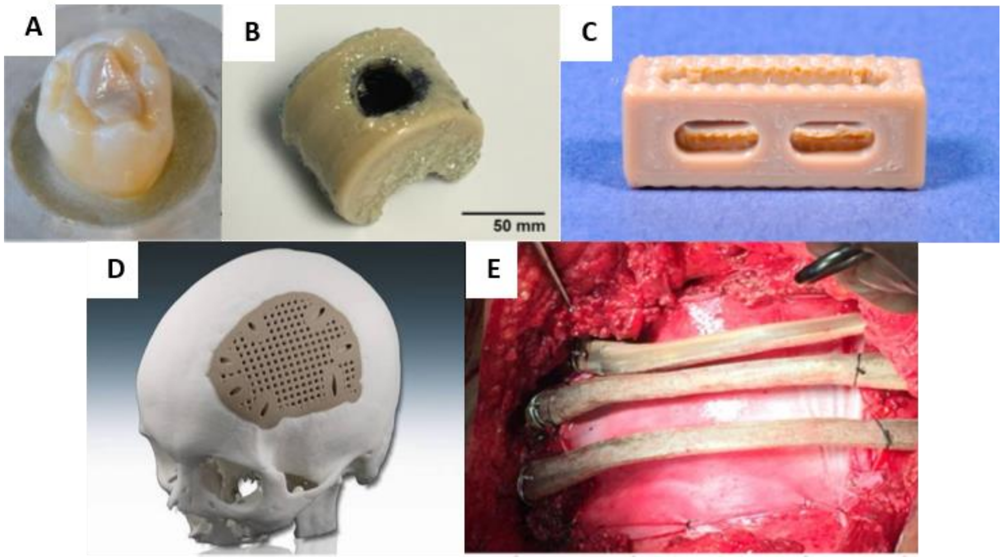

Figure 2. 5. AM PAEK is investigated for dental (a), reprinted from Prechtel et al. [36] with permission from Springer, spinal (b-c), reprinted from Delaney et al. [31] (b), and Basgul et al. [28] (c) with permission from Elsevier, cranial (d), reprinted from Berretta et al. [50] with permission from Elsevier, and chest reconstruction surgeries (e), reprinted from Kang et al. [2] with permission from Springer Nature, via FFF (a, b, c, e) and SLS (d) systems.

While research is still ongoing for the clinical use of AM PAEK, 3 studies implanted FFF PEEK into patients who were in need of PSI for chest reconstruction [2, 3, 44]. Kang et al. [2] implanted one patient with custom-designed rib prostheses for bone replacement due to tumor resection. Liu et al. [44] operated on an invasive bone tumor of the scapula in a patient and replaced the bone with a FFF PEEK scapula. Lastly, Wang et al. [3] implanted 18 patients with FFF PEEK implants for chest wall reconstruction. Additionally, infection prevention was investigated conceptually by a spinal clip design [31, 32] and antibacterial drug release via biodegradable polymer coating on PAEK for implants [34], however, these studies do not include *in vivo* studies and *in vitro* bioactivity studies.

2.5 Discussion

Additive manufacturing PAEKs for implant applications has gained increasing interest in the past decade. In this review, we evaluated the printing conditions, strength limitations, and biocompatibility of AM PAEK, along with the therapeutic areas for AM PAEK implants. Important printing conditions are summarized for both methods, SLS and FFF, here. The variety in printing conditions across the studies must be noted along with the differences in printing technology capabilities, both of which affect the biologic and material properties of PAEK. Although there has been an effort on improving 3D printed PAEK strength via printing parameter optimization, there is no standardized method for additively manufacturing PAEK implants under a set of generally accepted or optimized conditions. Current studies assert that AM PAEK may provide sufficient strength under impact loads, but the impact and fatigue performance of these implants must be evaluated further in the future. AM PAEK showed promising *in vitro* bioactivity and *in vivo* osseointegration and was found to be suitable for various material incorporations such as biodegradable polymers and antibacterial agents. Already, AM PAEK implants have been implanted in humans for chest reconstruction surgeries due to tumors, representing a significant step in adopting these materials for clinical use. Still, standards followed for implantations remain undeveloped, and careful risk management and quality assurance assessments are needed for AM PAEK implants prior to the implementation of POC manufacturing.

We found more papers using FFF than SLS for PAEK implants. This might be due to the financial burden of obtaining an SLS system and the challenges related to powder handling and recyclability [23]. Although SLS provides more freedom in terms of available materials and design complexity, powder management is questioned in a hospital environment regarding sterilization and safety. On the other hand, FFF medical printers are already developed to enable 3D printing in a sterile environment [37]. Industrial grade materials were used more often than the medical-grade for both methods, possibly due to the high cost of medical-grade materials which must be created and tested in compliance with relevant guidelines. Processing temperatures and power is important and ranged across the studies for both AM technologies. These values depend on the dimensions of the part printed, the machine capabilities, and the number of samples printed in a single build [29, 63]. Increasing the processing temperature or power may help to increase the mechanical strength, however, temperature/power must be low enough to still allow for additive manufacturing of detailed parts without deformation. We also found variety in the spot and nozzle diameters and the layer height chosen according to the extruder/spot size. Smaller spot/nozzle sizes and layer heights would allow printing finer details and better surface finish, however, might compromise on the strength [29]. The print speed range was higher for SLS than FFF studies. While laser speed is limited by the mechanical printer design for SLS, FFF speed is not only restricted by the extruder mechanical design but also material flow. One FFF study demonstrated this limitation for spinal implants, finding that undesired porosity increased with higher speeds [28]. Porous designs are explored in almost half of the studies (48%) and were more extensively studied using SLS (87%). Although porous designs aiming to improve implant osseointegration are often inspired by the high porosity of cancellous bone [17], the designed porosity varied across the studies between 30-74%. Interestingly, more than half of the studies (58%) mention neither the designed porosity percentage nor the actual experimental porosity percentage. There is only one study that provided both actual experimental porosity and designed porosity of the porous designs [17]. For solid designs and nonporous implants, undesired porosity might occur during processing. However, not many studies (10%) reported undesired porosity. Similarly, only a few studies mention annealing as a post-processing method for the AM PAEK. We found variety in the annealing temperatures and durations of these studies. Though annealing has been indicated to relieve stress and increase mechanical strength by improving crystallization [64], it was also found to have no impact on improving the mechanical properties of AM PEEK implants post-printing [43]. One study also reported shrinkage of PEEK samples resulting from additional heating, signifying a possible threat to the dimensional stability of AM PAEK [52]. Obviously, the potential alteration of AM implant size is a critical consideration in post-processing management, and it would be beneficial for future research to provide guidance on the post-printing heating necessity of AM PAEK implants.

Regarding the biomechanical evaluation of AM PAEK implants, the main loading conditions were chosen as compression and tension. In addition to the outcome measurement discrepancy, differences in the printing parameters and dimensions for each tested part make the direct comparison of these study results unfeasible. It was observed that strength, load, and hardness values were recorded for mechanically tested AM PAEK. Keeping in mind these variances, AM spinal implants printed under various conditions demonstrated between 51-82% of the maximum machined spinal implant load before failure. AM dental inlays showed between 48-103% strength of machined inlays. AM costal cartilage prosthesis is shown to be in the range of natural costal cartilage [39]. Only a few studies (18%) printed and tested standard dog-bone specimens in addition to printed implants/scaffolds to determine the mechanical properties of 3D printed materials. However, dimensional adjustments of the standard dog-bone specimen and designs from different standards created challenges for drawing conclusions from the data provided across the studies. Further research will be useful to develop standard testing for 3D printed implants that are printed under certain printing conditions with specific materials. For instance, AM dental implants printed with the same material provided from different suppliers demonstrated different mechanical strength [36]. This is substantial to explore, as different suppliers are now offering their medical-grade filaments/powders while also moving to the transition process for POC-AM.

Studies in this review reinforce the notion that printing conditions greatly affect 3D printed implant strength, as widely stated in the literature for AM parts [24]. A potentially important parameter when 3D printing implants is the choice of implant number printed in a single build. It should be determined cautiously, since using FFF implant number was shown to significantly impact the mechanical strength of spinal implants [29]. However, when discussing the mechanical outcomes, most of the studies did not mention this number. This should be noted for future studies. Similarly, undesired porosity was shown to decrease mechanical strength in the implant studies, as is reported in non-medical AM PAEK literature [65]. This undesired porosity might be located in certain areas, which might affect implant strength when bearing loads in different directions. Further investigations on the porosity locations and their effect under different loading conditions are needed. Only four studies (10%) measured the undesired porosity when the end goal was printing 100% infill implants/structures. A significant majority of studies for implant applications focused on porous scaffolds and compared the strength of porous parts with that of cancellous bone. Most of the studies indicated that the strength of porous parts was higher than human cancellous bone (0.1-16 MPa) [48, 60]. However, the designed and/or experimental porosity percentage of the porous scaffolds are not indicated in most of the studies. It is not recommended to compare the results with human cancellous bone directly without considering the porosity. Finally, one study showed that autoclaving and thermocycling did not affect the mechanical outcomes of dental inlays, which is promising for the sterilization of AM PAEK implants [37]. However, this process should be explored further for the other therapeutic areas in simulated body environments.

Regardless of printing conditions, 3D printed implants may be anisotropic meaning they will display different biomechanical strengths when tested in different directions as stated for AM PAEK implants [37, 50]. Therefore, it is crucial to establish all the mechanical properties of a 3D printed implant in all directions, since the implant will face more complex loading conditions once implanted inside the body. Finally, despite the enhancement of bioactivity afforded by material incorporations into AM PAEKs for implant applications, further research is needed to understand the strength compromise of the scaffolds for specific material additions in the future.

AM PAEK has been evaluated both *in vivo* and *in vitro*. 15% of the studies conducted *in vivo* animal studies, whereas almost half of the studies (48%) investigated biocompatibility *in vitro*. *In vivo* studies were conducted on sheep and rabbits and indicated satisfactory osseointegration. All the *in vitro* studies indicated good bioactivity for AM PAEK, with a few of them specifically measuring antibacterial activity. Current biocompatibility studies of porous AM PAEK indicate promising *in vitro* and *in vivo* behavior for long term implantation. Increased bioactivity for AM implant surfaces compared to machined were reported [41] and could be explained by the increased surface roughness of PAEKs via AM. Surface topography is known to have a major effect on cell behavior and has been studied for AM PAEK implants [40, 41]. Among *in vivo* and *in vitro* studies, more than half of the studies incorporated materials into PEEK/PEKK and inspected the biocompatibility and osseointegration. Materials incorporated in these studies can be summarized as nanoparticles such as oxides [52], bioceramics [27, 59, 61, 62], biological agents [56], and antibacterial drugs [34, 49]. Some studies introduced these materials via biodegradable polymers. While the positive effect of these materials on the bioactivity of AM PAEK is mentioned, the importance of the optimum weight percentage for both mechanical and bioactivity outcomes is emphasized. For instance, enhanced antibacterial drug rate inhibits the antibacterial activity but may also impact cell activity and viability. Biodegradable polymers enable the incorporation of the desired material, however, careful design consideration is needed regarding the mechanical stability for the long-term 3D printed implants.

AM PAEKs have been investigated to treat the following therapeutic areas so far: spinal, craniomaxillofacial, dental, and thoracic. In addition to ongoing preclinical research for AM PAEK, FFF PEEK prostheses were implanted in 20 patients clinically. It is crucial to mention that the regulations followed for AM PAEK implants remain unclear for these studies, where self-developed printers and unconfirmed medical grade materials were used. One study mentioned good qualitative outcomes for rib prosthesis implanted in a patient [2], whereas dislocation and disjunction of a FFF PEEK scapula prosthesis were observed in another study after three months of implantation [44]. Further explanations are needed to interpret such failures to determine if it is due to the manufacturing method, implant design, or surgical method applied. On the other hand, successful outcomes were recorded for 18 patients who received FFF PEEK implants for chest wall reconstruction [3]. Although 14% less forced vital capacity (a measure of lung function) was observed postoperatively, this is linked to constraints of treatment options rather than implant performance. Finally, AM PAEKs were designed to treat and prevent the possible post-operative infection by antibacterial drugs incorporated into biodegradable polymer coating onto PAEK [34]. Alternatively, AM enabled a FFF spinal device to prevent infection for spinal surgeries by allowing for controlled drug released post-surgery [31, 32]. *In vitro* and *in vivo* studies in this area will lead researchers for infection prevention efforts post-surgery via AM PAEK.

2.6 Study Limitations & Conclusion

Some limitations should be noted for this chapter. We evaluated the PAEK AM studies which investigated implants and/or parts for implant applications. There is inconsistency in the printing conditions and methods reported for each study, therefore every parameter could not be extracted from each paper. Although 73% of the studies conducted biomechanical tests on AM PAEK, there are no standard testing protocols for implants printed under unified conditions. Even material assessment studies could not be compared due to differences in test specimen size and shape and standards followed. However, identifying these variations in the literature is the first step in addressing them in order to move the guidelines and regulations in 3D printing PAEK implants forward for POC AM. In this review, while *in vivo* and *in vitro* studies are reviewed in general to show the biologic response of AM PAEK implants, detailed outcomes of these studies regarding bioactivity and osseointegration were out of the scope of this review. As more studies are conducted, more detailed comparisons and assessments will be helpful.

In summary, various research conducted on AM PAEK for implants have been systematically reviewed here in order to help the further development towards POC AM. Printing conditions from these 40 studies were summarized and the inconsistencies across the studies were recognized. As the current studies revealed reasonable biomechanical strength for AM PAEK implants under uniaxial compression or tension conditions, further research is needed under standardized static and fatigue loading conditions taking the anisotropic behavior into consideration. Studies reported improved bioactivity and promising antibacterial activity *in vitro* on AM PAEK, however, there are still knowledge gaps and further *in vivo* studies would be beneficial. Although there is an early effort on AM PAEK implantation, standard printing and testing conditions accompanied by more *in vitro* and *in vivo* studies are required to fill these gaps. We intend for this systematic review to help stimulate further research towards AM PAEKs for AM-POC.

2.7 References

1. Honigmann, P., et al., *Patient-Specific Surgical Implants Made of 3D Printed PEEK: Material, Technology, and Scope of Surgical Application.* Biomed Res Int, 2018. **2018**: p. 4520636.
2. Kang, J., et al., *Custom design and biomechanical analysis of 3D-printed PEEK rib prostheses.* Biomechanics and Modeling in Mechanobiology, 2018. **17**(4): p. 1083-1092.
3. Wang, L., et al., *Three-Dimensional Printing PEEK Implant: A Novel Choice for the Reconstruction of Chest Wall Defect.* The Annals of Thoracic Surgery, 2019. **107**(3): p. 921-928.
4. Zhong, R., et al., *Clinical application of triangular parabolic PEEK mesh with hole button produced by combining CAD, FEM and 3DP into cranioplasty.* Biomedical Research, 2018. **29**.
5. El Halabi, F., et al., *Mechanical characterization and numerical simulation of polyether-ether-ketone (PEEK) cranial implants.* J Mech Behav Biomed Mater, 2011. **4**(8): p. 1819-32.
6. Cheng, K.-j., et al., *Topological optimization of 3D printed bone analog with PEKK for surgical mandibular reconstruction.* Journal of the Mechanical Behavior of Biomedical Materials, 2020: p. 103758.
7. Putra, N.E., et al., *Multi-material additive manufacturing technologies for Ti-, Mg-, and Fe-based biomaterials for bone substitution.* Acta Biomaterialia, 2020. **109**: p. 1-20.
8. Huang, M.F., et al., *The Use of Patient-Specific Implants in Oral and Maxillofacial Surgery.* Oral and Maxillofacial Surgery Clinics of North America, 2019. **31**(4): p. 593-600.
9. Memon, A.R., et al., *A review on computer-aided design and manufacturing of patient-specific maxillofacial implants.* Expert Review of Medical Devices, 2020. **17**(4): p. 345-356.
10. Gualdrón, C.I.L., et al., *Present and future for technologies to develop patient-specific medical devices: A systematic review approach.* Medical Devices: Evidence and Research, 2019. **12**: p. 253-273.
11. Fan, D., et al., *Progressive 3D Printing Technology and Its Application in Medical Materials.* Frontiers in Pharmacology, 2020. **11**.

12. Poukens, J., et al., *A classification of cranial implants based on the degree of difficulty in computer design and manufacture.* The International Journal of Medical Robotics and Computer Assisted Surgery, 2008. **4**(1): p. 46-50.

13. Järvinen, S., et al., *The use of patient specific polyetheretherketone implants for reconstruction of maxillofacial deformities.* Journal of Cranio-Maxillofacial Surgery, 2019. **47**(7): p. 1072-1076.

14. Toth, J.M., *Chapter 7 - Biocompatibility of Polyaryletheretherketone Polymers A2 - Kurtz, Steven M*, in *PEEK Biomaterials Handbook*. 2012, William Andrew Publishing: Oxford. p. 81-92.

15. Torstrick, F.B., et al., *Getting PEEK to Stick to Bone: The Development of Porous PEEK for Interbody Fusion Devices.* Tech Orthop, 2017. **32**(3): p. 158-166.

16. Torstrick, F.B., et al., *Porous PEEK improves the bone-implant interface compared to plasma-sprayed titanium coating on PEEK.* Biomaterials, 2018. **185**: p. 106-116.

17. Spece, H., et al., *3D printed porous PEEK created via fused filament fabrication for osteoconductive orthopaedic surfaces.* Journal of the Mechanical Behavior of Biomedical Materials, 2020: p. 103850.

18. Hatz, C.R., et al., *Can an entry-level 3D printer create high-quality anatomical models? Accuracy assessment of mandibular models printed by a desktop 3D printer and a professional device.* International Journal of Oral and Maxillofacial Surgery, 2020. **49**(1): p. 143-148.

19. Licci, M., et al., *Development and validation of a synthetic 3D-printed simulator for training in neuroendoscopic ventricular lesion removal.* Neurosurgical Focus, 2020. **48**(3).

20. Tseng, J.-W., et al., *Screw extrusion-based additive manufacturing of PEEK.* Materials & Design, 2018. **140**: p. 209-221.

21. T., H. and R. P., *A new method for the model-independent assessment of thickness in three-dimensional images.* Journal of Microscopy, 1997. **185**(1): p. 67-75.

22. M., H. *3D Printing at Point of Care*. 2020 [cited 2020 06/05]; Available from: https://3dheals.com/3d-printing-at-point-of-care.

23. Singh, S., C. Prakash, and S. Ramakrishna, *3D printing of polyether-ether-ketone for biomedical applications.* European Polymer Journal, 2019. **114**: p. 234-248.

24. Wang, Y., et al., *Parameters Influencing the Outcome of Additive Manufacturing of Tiny Medical Devices Based on PEEK.* Materials (Basel), 2020. **13**(2).

25. Moher, D., et al., *Preferred Reporting Items for Systematic Reviews and Meta-Analyses: The PRISMA Statement.* PLOS Medicine, 2009. **6**(7): p. e1000097.

26. Rohatgi, A., *WebPlotDigitizer*. 2019: San Francisco, CAlifornia, USA.

27. Feng, P., et al., *A Multimaterial Scaffold With Tunable Properties: Toward Bone Tissue Repair.* Adv Sci (Weinh), 2018. **5**(6): p. 1700817.

28. Basgul, C., et al., *Does annealing improve the interlayer adhesion and structural integrity of FFF 3D printed PEEK lumbar spinal cages?* Journal of the Mechanical Behavior of Biomedical Materials, 2020. **102**: p. 103455.

29. Basgul, C., et al., *Thermal localization improves the interlayer adhesion and structural integrity of 3D printed PEEK lumbar spinal cages.* Materialia, 2020. **10**: p. 100650.

30. Cheng, B.C., et al., *A comparative study of three biomaterials in an ovine bone defect model.* Spine J, 2020. **20**(3): p. 457-464.

31. Delaney, L.J., et al., *Acoustic Parameters for Optimal Ultrasound-Triggered Release from Novel Spinal Hardware Devices.* Ultrasound in Medicine & Biology, 2020. **46**(2): p. 350-358.

32. Delaney, L.J., et al., *Ultrasound-triggered antibiotic release from PEEK clips to prevent spinal fusion infection: Initial evaluations.* Acta Biomaterialia, 2019. **93**: p. 12-24.

33. Elhattab, K., et al., *Fabrication and evaluation of 3-D printed PEEK scaffolds containing Macropores by design.* Materials Letters, 2020. **263**: p. 127227.

34. Lau, N.C., et al., *Preparation and characterization for antibacterial activities of 3D printing polyetheretherketone disks coated with various ratios of ampicillin and vancomycin salts.* Applied Sciences (Switzerland), 2020. **10**(1).

35. Petersmann, S., et al., *Mechanical properties of polymeric implant materials produced by extrusion-based additive manufacturing.* Journal of the Mechanical Behavior of Biomedical Materials, 2020. **104**: p. 103611.

36. Prechtel, A., et al., *Fracture load of 3D printed PEEK inlays compared with milled ones, direct resin composite fillings, and sound teeth.* Clinical Oral Investigations, 2020.

37. Prechtel, A., et al., *Comparison of various 3D printed and milled PAEK materials: Effect of printing direction and artificial aging on Martens parameters.* Dental Materials, 2020. **36**(2): p. 197-209.

38. Su, Y., et al., *Additively-manufactured poly-ether-ether-ketone (PEEK) lattice scaffolds with uniform microporous architectures for enhanced cellular response and soft tissue adhesion.* Materials & Design, 2020. **191**: p. 108671.

39. Zhang, C., et al., *Bionic design and verification of 3D printed PEEK costal cartilage prosthesis.* Journal of the Mechanical Behavior of Biomedical Materials, 2020. **103**: p. 103561.

40. Han, X., et al., *Carbon Fiber Reinforced PEEK Composites Based on 3D-Printing Technology for Orthopedic and Dental Applications.* J Clin Med, 2019. **8**(2).

41. Han, X., et al., *An In Vitro Study of Osteoblast Response on Fused-Filament Fabrication 3D Printed PEEK for Dental and Cranio-Maxillofacial Implants.* Journal of clinical medicine, 2019. **8**(6): p. 771.

42. Jung, H.-D., et al., *Enhanced bioactivity of titanium-coated polyetheretherketone implants created by a high-temperature 3D printing process.* Biofabrication, 2019. **11**(4): p. 045014.

43. Basgul, C., et al., *Structure-property relationships for 3D printed PEEK intervertebral lumbar cages produced using fused filament fabrication.* J Mater Res, 2018. **33**(14): p. 2040-2051.

44. Liu, D., et al., *Application of 3D-printed PEEK scapula prosthesis in the treatment of scapular benign fibrous histiocytoma: A case report.* Journal of Bone Oncology, 2018. **12**: p. 78-82.

45. Zhao, F., D. Li, and Z. Jin, *Preliminary Investigation of Poly-Ether-Ether-Ketone Based on Fused Deposition Modeling for Medical Applications.* Materials (Basel), 2018. **11**(2).

46. Deng, L., Y. Deng, and K. Xie, *AgNPs-decorated 3D printed PEEK implant for infection control and bone repair.* Colloids and Surfaces B: Biointerfaces, 2017. **160**: p. 483-492.

47. Vaezi, M. and S. Yang, *Extrusion-based additive manufacturing of PEEK for biomedical applications.* Virtual and Physical Prototyping, 2015. **10**(3): p. 123-135.

48. Feng, P., et al., *Graphene oxide-driven interfacial coupling in laser 3D printed PEEK/PVA scaffolds for bone regeneration.* Virtual and Physical Prototyping, 2020. **15**(2): p. 211-226.

49. Wu, P., et al., *A polymer scaffold with drug-sustained release and antibacterial activity.* International Journal of Polymeric Materials and Polymeric Biomaterials, 2020. **69**(6): p. 398-405.

50. Berretta, S., K. Evans, and O. Ghita, *Additive manufacture of PEEK cranial implants: Manufacturing considerations versus accuracy and mechanical performance.* Materials and Design, 2018. **139**: p. 141-152.

51. Berretta, S., K.E. Evans, and O. Ghita, *Processability of PEEK, a new polymer for High Temperature Laser Sintering (HT-LS).* European Polymer Journal, 2015. **68**(Supplement C): p. 243-266.

52. Shishkovsky, I., et al., *Nano-size ceramic reinforced 3D biopolymer scaffolds: Tribomechanical testing and stem cell activity.* Composite Structures, 2018. **202**: p. 651-659.

53. Shishkovsky, I. and V. Scherbakov, *Selective Laser Sintering of Biopolymers with Micro and Nano Ceramic Additives for Medicine.* Physics Procedia, 2012. **39**: p. 491-499.

54. Shishkovsky, I., K. Nagulin, and V. Sherbakov, *Laser sinterability and characterization of oxide nano ceramics reinforced to biopolymer matrix.* The International Journal of Advanced Manufacturing Technology, 2015. **78**(1): p. 449-455.

55. Shuai, C., et al., *Antibacterial Capability, Physicochemical Properties, and Biocompatibility of $nTiO_2$ Incorporated Polymeric Scaffolds.* Polymers, 2018. **10**(3): p. 328.

56. Roskies, M.G., et al., *Three-dimensionally printed polyetherketoneketone scaffolds with mesenchymal stem cells for the reconstruction of critical-sized mandibular defects.* Laryngoscope, 2017. **127**(11): p. E392-e398.

57. Shuai, C., et al., *Silane Modified Diopside for Improved Interfacial Adhesion and Bioactivity of Composite Scaffolds.* Molecules (Basel, Switzerland), 2017. **22**(4): p. 511.

58. Roskies, M., et al., *Improving PEEK bioactivity for craniofacial reconstruction using a 3D printed scaffold embedded with mesenchymal stem cells.* Journal of Biomaterials Applications, 2016. **31**(1): p. 132-139.

59. Shuai, C., et al., *Characterization and Bioactivity Evaluation of (Polyetheretherketone/Polyglycolicacid)-Hydroyapatite Scaffolds for Tissue Regeneration.* Materials (Basel, Switzerland), 2016. **9**(11): p. 934.

60. Shuai, C., et al., *Polyetheretherketone/poly (glycolic acid) blend scaffolds with biodegradable properties.* J Biomater Sci Polym Ed, 2016. **27**(14): p. 1434-46.

61. von Wilmowsky, C., et al., *Effects of bioactive glass and beta-TCP containing three-dimensional laser sintered polyetheretherketone composites on osteoblasts in vitro.* J Biomed Mater Res A, 2008. **87**(4): p. 896-902.

62. Tan, K.H., et al., *Fabrication and characterization of three-dimensional poly(ether- ether- ketone)/-hydroxyapatite biocomposite scaffolds using laser sintering.* Proc Inst Mech Eng H, 2005. **219**(3): p. 183-94.

63. Wang, P., et al., *Effects of printing parameters of fused deposition modeling on mechanical properties, surface quality, and microstructure of PEEK.* Journal of Materials Processing Technology, 2019. **271**: p. 62-74.

64. Jaekel, D., F.J. Medel, and S.M. Kurtz, *Validation of crystallinity measurements of medical grade PEEK using specular reflectance FTIR-microscopy*. Vol. 5. 2009. 2511-2516.

65. Cicala, G., et al., *Engineering thermoplastics for additive manufacturing: a critical perspective with experimental evidence to support functional applications.* Journal of Applied Biomaterials & Functional Materials, 2017. **15**(1): p. e10-e18.

Chapter 3: Effects of the current FFF technology parameters on the structural stability of 3D printed PEEK cages

3.1 Abstract

Additive manufacturing is a potential application for polyaryletheretherketone (PEEK) spinal interbody fusion cages, which were introduced as an alternative to titanium cages because of their biocompatibility, radiolucency, strength, and resistance to subsidence. Additive Manufacturing of PEEK is challenging and poorly understood because of its high melting temperature (over 340°C). The purpose of this study was to (1) evaluate the FFF PEEK spinal implants additively manufactured with two generations of FFF machines (2) characterize the mechanical and microstructure of two generations of FFF PEEK implants (3) determine the effect of parameters on additively manufactured PEEK spinal implants' structural stability. A standard cage design, which was used to validate ASTM F2077 [1], was 3D printed with both first and second-generation FFF PEEK printers. 1st generation cages were printed single and multiple (1 and 6) in a single build with one available nozzle size (0.4 mm) under four different print speeds (1000, 1500, 2000 & 3000 mm/min). X-Ray Diffraction (XRD) was used to determine the degree of crystallinity of 1st generation PEEK cages. For the 2nd generation of FFF cages, parameters varied as follows: nozzle sizes (0.2 mm and 0.4 mm), print speeds (1500 and 2500 mm/min), and the number of cages printed in a single build (1, 4, and 8). To calculate the porosity percentage, FFF cages were micro-CT scanned prior to destructive testing. Mechanical tests were then conducted on FFF cages according to ASTM F2077 [1]. Although the main temperature settings of two-generation FFF

machines were different for 3D printed cages, the mechanical strength of both generations' FFF cages was similar. Layer delamination was identified in both generations of FFF PEEK cages. Altering the cooling time of a layer was not able to change the failure mechanism of FFF cages, however, it was able to improve cages' mechanical strength. Printing a single cage per build, which decreases a layer's cooldown time, caused a higher ultimate load than printing multiple cages per build. In the same manner, regardless of the number printed per build, cages printed with bigger nozzle diameter achieved higher ultimate load compared to cages printed with smaller nozzle diameter, in which the cooling time of a layer was almost doubled. Additionally, printing with a bigger nozzle diameter resulted in less porosity, which might have an additional effect on the failure mechanism. This study shows the parameters which indirectly enhance the thermal management during 3D printing affect the interlayer adhesion, thus the macro mechanical properties of FFF cages.

3.2 Introduction

Intervertebral lumbar devices are common to treat patients in which the spine is unstable, such as in degenerative disc disease, spondylolisthesis, and recurrent disc herniation, to maintain the height of the intervertebral disc [2, 3]. Polyetheretherketone (PEEK) interbody fusion cages were introduced as an alternative to titanium (Ti) cages because of several advantages [4, 5]. First, PEEK has a comparable elastic modulus with cortical bone, which reduces the stress at the adjacent vertebrae and reduces subsidence [6]. Second, PEEK's radiolucency allows for radiographic monitoring and/or tracking of cage position, misalignment, and bone ingrowth needed for a healthy fusion. On the other hand, PEEK is costly and its hydrophobicity limits a positive bone interaction [7]. There have been efforts to introduce modifications to PEEK to create surface porosity and hence improve osseointegration [8]. However, traditional manufacturing techniques such as porogen leaching are restricted to limited areas when creating porous structures on cages [9]. Additive Manufacturing (AM) has sparked cage manufacturers' interest, by enabling medical device customization and allowing to manufacture complex shapes to enhance cell attraction [10-15]. Fused Filament Fabrication (FFF) is one of the AM methods, for which temperature management is very important since it is related to interlayer bonding strength [16, 17], the crystallinity of the polymer [18], and the deformation of the printed part [19, 20]; all of which affect the macro mechanical properties of the finished implant. Although previous research has shown the feasibility of FFF PEEK [21-24], the importance of the interlayer adhesion was identified as the failure mechanism that limited the macro mechanical properties of FFF PEEK load-bearing implants [25]. It was shown that not controlling the cooling conditions of FFF parts is causing the poor interlayer adhesion and to overcome this problem overall parametric optimization of the FFF printing process is an important tool [16].

Previous researchers investigated the relationship of the bonding strength and the processing parameters experimentally [16, 26, 27]. Arif et al. [26] showed that the mechanical performance of FFF parts was significantly affected by fiber bonding which was regulated by the thermal conditions during the printing process. Li et al. [27], on the other hand, determined the effect of an air gap, layer thickness, and printing speed on the bonding intensity between adjacent filaments and concluded that layer thickness and printing speed would primarily affect the bonding process of filaments compared to other parameters. Furthermore, Sun et al. [16] analyzed the processing temperatures on the bonding quality (assessed by the changes in the mesostructure and the degree of healing achieved between the layers) of FFF parts and observed that cooling conditions affect the bonding quality significantly.

In the literature, it is clear that the FFF parameters which affect the thermal conditions during printing have an impact on the 3D printed structures' mechanical properties. However, so far, it is poorly understood how a load-bearing PEEK implant's failure mechanism and layer adhesion will be affected by altering the FFF process parameters. Hence, the following research questions were investigated: (1) Can altering the structural and FFF parameters, which indirectly control the thermal conditions, change the failure mechanism of FFF PEEK cages? (2) How is the cooling time of a layer is affected by changing the structural and FFF process parameters? (3) Will decreasing the cooling time of a layer increase the mechanical loads that 3D printed PEEK cages bear by enhancing the interlayer adhesion?

3.3 Materials & Methods

3.3.1 FFF Process & Parameters

1st generation standardized spinal cages were 3D printed with an experimental filament developed from PEEK OPTIMA™ LT1, whereas for 2nd generation cages 450G™ PEEK filament was used (Invibio Biomaterial Solutions Ltd., Thornton Cleveleys, UK), which were dried at 60°C for at least 12 hours prior to printing. OPTIMA™ LT1 is the most widely used grade of PEEK for implant applications, with a melt flow index of 3.4 and molecular weight of 115,000 [28]. It has a reported melting temperature of ~343°C and glass transition temperature of ~145°C with a crystallization peak of ~160°C [29]. 450G™ is an industrial-grade material and has the same chemical properties as the medical-grade OPTIMA™ LT1 (such as melting and glass transition temperature).

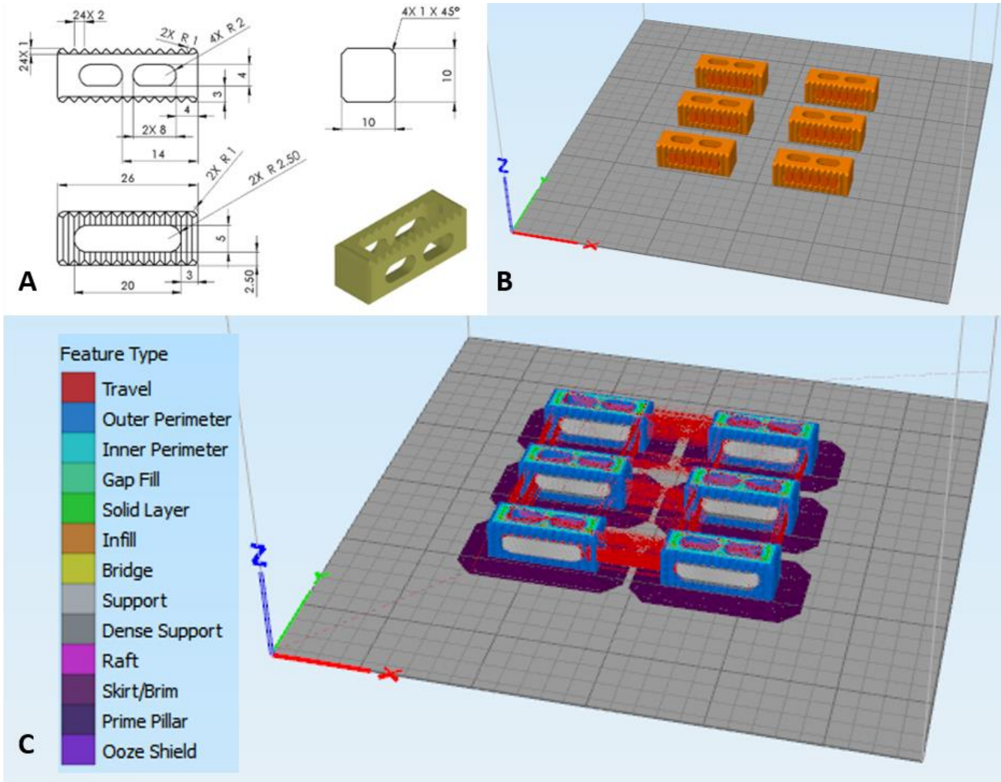

Figure 3. 1. The CAD drawing (A) shows the design parameters for the cage used in this study. FFF cages were created with support structures on the heated bed (B) and the g-codes were created with the addition of the brims around the cages (C) on the Simplify 3D software.

The lumbar cage design used in this study was developed as a reference for ASTM interlaboratory studies (Fig. 3. 1 (A)) [30]. The Standard Triangle Language (STL) file of the cage was created from a 3D model drafted using commercially available software (SolidWorks 2016). Simplify 3D software (available commercially) was used to digitally slice the samples and create the g-codes for both FFF machines. Three-mm temporary support structures were generated in the holes of both sides of the cages to ensure the horizontal cage struts did not collapse during printing (Fig. 3. 1 (B)). In addition, to increase the adhesion between the print object and the print bed, brims were added to the cages (Fig. 3.1 (C)). For 2nd generation cages, additional leg structures were added around the four corners of the cages to avoid any warping effect during the printing (Fig. 3. 2 (E-left)). These support structures were subsequently trimmed from the cages after printing and before any mechanical or physical property testing.

1st generation cages were manufactured with the 1st generation FFF machine, Indmatec HPP 155/Gen 2 and 2nd generation cages were 3D printed with the 2nd generation FFF machine, Apium P220, from the same manufacturer (Apium Additive Technologies GmbH, Karlsruhe, Germany) (Fig. 3. 2). To increase the adhesion between the cages and the heated bed further, one layer of Dimafix® (DIMA 3D Printers) solution was applied onto the heated bed before printing.

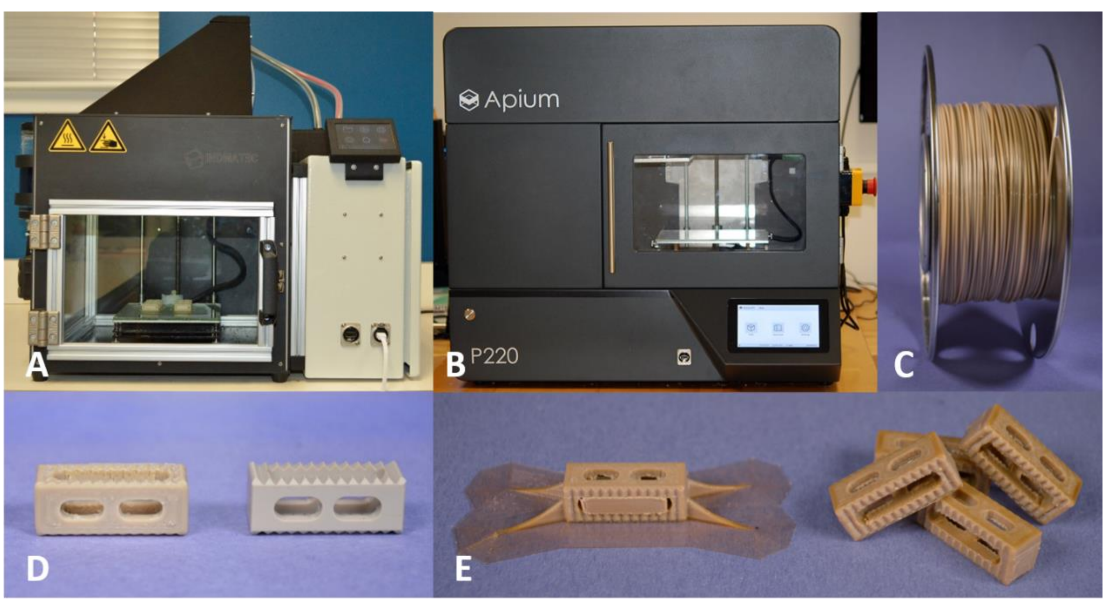

Figure 3. 2. Spinal cages were printed using two generations of commercial FFF machines capable of reaching the high temperatures associated with printing PEEK (Indmatec HPP 155/Gen 2 (A) & Apium P220 (B)) and 1.75 mm PEEK filaments provided in industrial and medical grades (Invibio) (C). Control cages were machined from the same material (D-right). The brims and support structures were removed prior to testing for both 1st and 2nd generation cages (E).

As controls, cages were machined from the PEEK OPTIMA™ LT1 extruded rod (Fig. 3.2 (D-right)). The first-generation printer could reach up to 450°C for the nozzle temperature and 150°C for the print bed temperature. The print environment is insulated, however, there is not an additional heating element inside the chamber. The second-generation printer, on the other hand, has a wider range both for the nozzle and bed temperatures (maximum of 540°C and 160°C, respectively). The print environment is again insulated, and there is an additional heating element which is a metal plate around the nozzle with a fixed temperature of 160-250°C.

Parameters, all of which can either directly or indirectly affect the thermal history of the layers within the cages, were investigated in this study. For 1st generation cages, printing conditions were kept same for all cohorts, except for the nozzle (extruder) X/Y axis movement speed, also referred to as “print speed” and the number of cages printed per build. 1st generation FFF cages were printed single cage or six cages per build under four different printing speeds, 1000, 1500, 2000, and 3000 mm/min (Table 3.1). For 2nd generation cages, four parameters studied were the nozzle size, print speed, layer thickness, and the number of cages printed per build. FFF cages were printed with two different nozzle diameters, which were 0.2 and 0.4 mm, under two different printing speeds, which were 1500 and 2500 mm/min. Under these four different conditions, cages were printed with a single cage, four cages, or eight cages per build. Under higher speed, single cages were printed with two different layer thicknesses, which were ½ and ¼ times the original nozzle diameter (Table 3.1).

Table 3. 1. FFF parameters used in this study for 1st and 2nd generation PEEK printers.

	1st Generation Printer	2nd Generation Printer
Extruder		
Nozzle Diameter	0.4	0.4 & 0.2
Extrusion Multiplier	0.98	0.98
Extrusion Width	0.48	0.48
Ooze Control (Retraction Enabled)		
Retraction Distance (mm)	0.55	0.55
Retraction Speed (mm/min)	1800	1800
Retraction Vertical Lift	0.00	0.00
Layer Settings		
Layer Height (mm)	0.1	0.05 & 0.1 & 0.2
Top Solid Layers	3	3
Bottom Solid Layers	3	3
Outline/Perimeter Shells	3	3
First Layer Setting		
1st Layer Height	180% Height	180% Height
1st Layer Width	100% Width	100% Width
1st Layer Speed	30%	30%
Additions (Skirt/Brim)		
Use Skirt/Brim	Enabled	Enabled
Skirt Layers	1	1
Skirt Offset from Part (mm)	0.00	0.00
Skirt Outlines	15	15
Infill Settings		
Internal Fill Pattern	Rectilinear	Rectilinear
External Fill Pattern	Rectilinear	Rectilinear
Interior Fill Percentage	100%	100%
Outline Overlap	50%	50%
Infill Extrusion Width	90%	90%

Minimum Infill Length (mm)	5	5
Support Settings		
Generate Support Material	Enabled	Enabled
Support Infill Percentage	30%	30%
Print Support Every (layers)	1	1
Temperature Settings		
Bed Temperature (°C)	100	130
Nozzle Temperature(°C)	390-410	485
Speed Settings		
Default Printing Speed (mm/min)	1000-3000	1500-2500
Outline Underspeed	50%	50%
Solid Infill Underspeed	80%	80%
X/Y Axis Movement Speed (mm/min)	4800	4800
Z Axis Movement Speed (mm/min)	1000	1000
Other		
Build Volume (mm^3)	145x135x148	205x155x150
Filament Diameter (mm)	1.75	1.75

In addition, the amount of material used to print cages and the print times are recorded (in Table 3.2).

Table 3. 2. Material usage and time spent on builds in this study.

Printer	**Nozzle diameter (mm)**	**Speed (mm/min)**	**Layer thickness (mm)**	**Number of Cages per Build**	*Time of the build (min)*	*Material Used for print (g)*
1st Generation Printer	0.4	2500	0.1	1	53	2.43
		1000	0.1	6	377	13.28
		1500			242	13.28
		2000			202	13.28
		3000			122	13.28
	0.4	1500	0.1	1	52	2.60
				4	203	9.77

2nd Generation Printer				8	406	19.3
		2500	0.2	1	23	3.20
			0.1	1	32	2.60
				4	130	9.77
				8	261	19.3
	0.2	1500	0.1	1	122	2.67
				4	417	10.6
				8	828	21.0
		2500	0.05	1	130	2.51
			0.1	1	70	2.67
				4	277	10.6
				8	552	21.0

3.3.2 Mechanical Testing

Cages (n=6) from each cohort were tested under compression loading condition (ASTM F2077 [1]) with the help of an MTS Mini Bionix 858 system (MTS Systems Corporation, Eden Prairie, MN) (Fig. 3.3 (A)). Moreover, the test system meets the quality system requirements of ISO 17025 [31]. In addition, cages were tested in the vertical direction (z-plane) of their build orientation (x-y plane) to simulate the worst-case scenario for failure via layer delamination by applying the force perpendicular to the build direction (Fig. 3.3 (B)). This scenario was enhanced by conducting only compression which is the loading condition with the highest and instant load that will be applied on to the cages, out of three different loadings (compression, compression-shear, and torsion) and fatigue loading conditions according to ASTM F2077 [1].

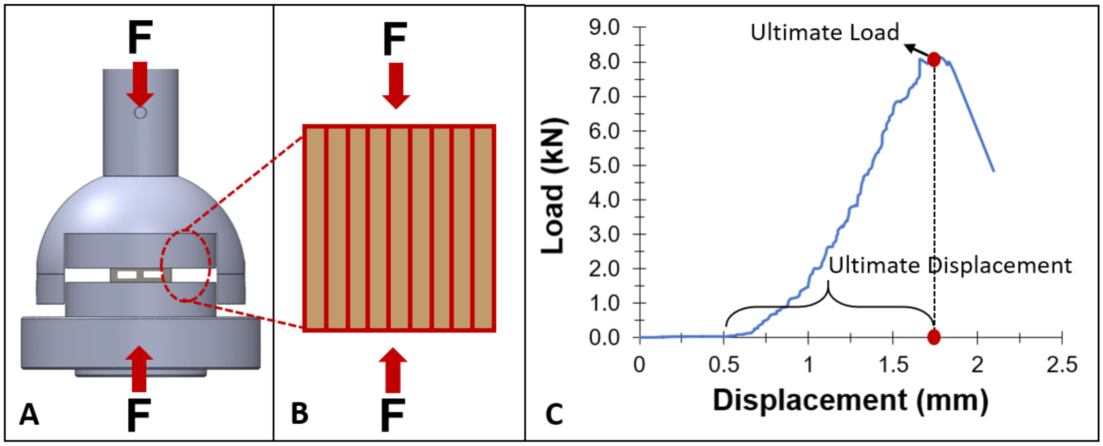

Figure 3. 3. Compression tests were conducted on the printed cages as per ASTM F2077 [30] (A) in the direction orthogonal to the build layers (B), ultimate load (N), and ultimate displacement (mm) values were calculated from the load/displacement curves (C).

The strain rate was 25 mm/min [1] and the maximum load of the cell was 15 kN, whereas the data was collected at 100 Hz. Load-displacement curves from compression data were collected. The ultimate load and displacement values were calculated using a custom script developed using commercial software (MATLAB 2016b (Fig. 3.3 (C)).

3.3.3 Imaging and Material Characterization

Prior to testing, three cages from each cohort were micro-CT scanned at 10 μm isotropic resolution using a Scanco μCT 80 (Scanco Medical, Switzerland). Both ends of the cage design, where it was solid cuboid, were defined as the regions of interest to obtain porosity measurements per cage (Fig. 3.4 (A)). A control volume (5x5x2 mm^3), limited by the standardized cage design, was created for the porosity calculations (Fig. 3.4 (B)). Two control volume measurements were taken from the designated regions per cage to compare the average porosity between the cohorts (n=6 per cohort). The histogram of the grayscale values (which correspond with densities) resulting from the micro-CT scans appeared as two clear peaks (one for the PEEK cages, and the other for empty space (i.e. air)). The threshold chosen for the segmentation threshold was the halfway point between the two peaks. Evaluations were conducted via Scanco software (Scanco Medical, Switzerland) on the control volumes. The evaluation for porosity percentage provided "Solid Volume/Total Volume" values. The porosity percentage of the control volumes were calculated using Equation 6.

$$1 - \frac{Volume_{Solid}}{Volume_{Total}} \tag{6}$$

Furthermore, detailed surface micrographs of printed cohorts were taken to analyze the porosity and the structure of the surface via scanning electron microscopy (SEM). Prior to SEM, cages were sputtered with platinum and palladium to achieve a conductive surface.

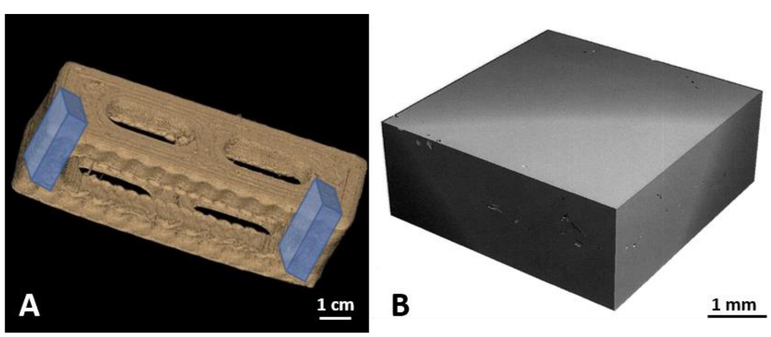

Figure 3. 4. Control volumes (shown as blue boxes) were taken from both ends of the micro-CT scanned cage (a), which were then used to measure the porosity of the printed cages (b).

In addition to SEM imaging, X-ray diffraction (XRD) (n=6) was used to determine the degree of crystallinity of 1st generation PEEK cages. Wide-angle x-ray scattering (WAXS) was determined as the scattering technique for XRD. An internal plate was used to collect diffracted X-ray at a distance of 82 mm from the sample for 60 minutes. The internal plate was then read using the RAXIA software to determine the diffraction pattern by plotting 2 theta (2θ) versus intensity. MagicPlot software was used to fit Gaussian distributions and determine the area of the curve to each crystalline peak. The degree of crystallinity was calculated using Equation 7.

$$\frac{Area_{Crystalline}}{Area_{Amorphous} + Area_{Crystalline}} \qquad (7)$$

3.3.4 Statistical Analysis

Normality tests were conducted on the distributions of residuals using the Shapiro-Wilk test. Generally, the distributions were normal. Therefore, 2-way ANOVA with a posthoc Tukey Honest Significant Difference Test were chosen to analyze the data. The ultimate load, ultimate displacement, and porosity metrics were the dependent variables while the nozzle diameter, cages printed per build, layer thickness, and print speed were the independent variables. Printer generation comparison was done via an independent sample t-test. SPSS software (IBM SPSS Statistics 25; Armonk, NY) was used to conduct the statistical analyses with $\alpha=0.05$.

3.4 Results

3.4.1 Imaging & Material Characterization

XRD confirmed that crystallinity did not depend on the manufacturing method in 1st generation FFF PEEK cages. XRD also did not show any significant differences between the printed and machined cohorts ($p=0.97$, 1.0, 1.0, and 1.0 for printed cohorts with 1000, 1500, 2000, and 3000 mm/min, respectively). The average crystallinity calculated via WAXS was approximately 49% (Table 3.3).

Table 3. 3. Metrics calculated in this study.

					Ultimate Load (N)		Ultimate Displacement (mm)		Porosity (%)		Crystallinity (%)	
Printer	**Nozzle diameter (mm)**	**Speed (mm/ min)**	**Layer thickness (mm)**	**Number of Cages per Build**	*Mean*	*Std dev*	*Mean*	*Std dev*	*Mean*	*Std dev*	*Mean*	*Std dev*
Machined (Controls)	-	-	-	-	14229	335	3.12	0.42	0	0	48.5	0.95
1st Generation Printer	0.4	2500	0.1	1	11686	751	3.50	0.37	1.80	0.14	-	
		1000		6	8964	304	1.43	0.18	1.88	1.12	49.5	4.32
		1500		6	8336	1044	1.55	0.85	3.82	0.89	47.9	4.26
		2000		6	7949	559	1.51	0.18	2.99	0.92	48.6	3.38
		3000		6	7856	167	1.63	0.05	19.6	2.70	49.1	3.13
2nd Generation Printer	0.4	1500	0.1	1	11330	326	2.81	0.15	0.71	0.23	-	
				4	8934	413	2.21	0.21	0.43	0.06	-	
				8	8558	968	2.51	0.50	0.44	0.16	-	
		2500	0.2	1	11670	911	3.71	0.27	-	-	-	
			0.1	1	11612	325	2.86	0.17	0.58	0.24	-	
				4	8860	456	2.18	0.10	0.77	0.20	-	
				8	9042	481	2.41	0.33	0.99	0.52	-	
	0.2	1500	0.1	1	7690	559	1.91	0.21	1.63	0.42	-	
				4	6672	495	1.65	0.11	1.75	0.40	-	
				8	8048	675	1.82	0.06	2.17	0.76	-	
		2500	0.05	1	8798	613	1.71	0.24	-	-	-	
			0.1	1	8694	612	2.09	0.18	1.23	0.32	-	
				4	7016	438	1.72	0.25	1.81	0.65	-	
				8	7141	1164	1.87	0.29	2.24	0.55	-	

In addition to crystallinity, for 1st generation cages, it was shown that the highest print speed (3000 mm/min) increased the level of undesired porosity in cages (20%) significantly compared to cages printed with under 2500 mm/min (2.9%) (Table 3.3). A significant difference in porosity between the printer generations was observed when single cages were printed under the speed '2500 mm/min' ($p<0.001$ and mean difference=1.21) (Fig. 3.5 (C)). For 2nd generation cages, there was a significant association between porosity and the number of cages printed per build as well as the nozzle diameter (mean difference=0.15% between cages printed one and four cages per build, 0.42% between one and eight cages printed per build, $p<0.001$ and mean difference=1.15% $p=0.02$, respectively). However, the porosity was not associated with changing the print speed for 2nd generation cages ($p=0.51$). Under slower speed and for all build sizes, printing with the smaller diameter nozzle was associated with higher porosity for the printed cages ($p<0.01$ for all and mean difference=0.92%, 1.32%, and 1.73% for cages printed one, four, and eight per build, respectively) (Fig. 3.5 (A)). In the same manner, under higher print speed and for all cage numbers printed at the same time, printing with the smaller diameter nozzle was associated with higher porosity for the cages ($p<0.05$ for all and mean difference=0.65%, 1.04%, and 1.25% for cages printed one, four, and eight per build, respectively) (Fig. 3.5 (B)). Furthermore, when the number of cages printed per build was compared regarding their porosity, there was a porosity difference only when printing with the smaller nozzle diameter under higher speed. Cages printed 8 per build had higher porosity compared to single printed cages ($p=0.002$ and mean difference=1.00%).

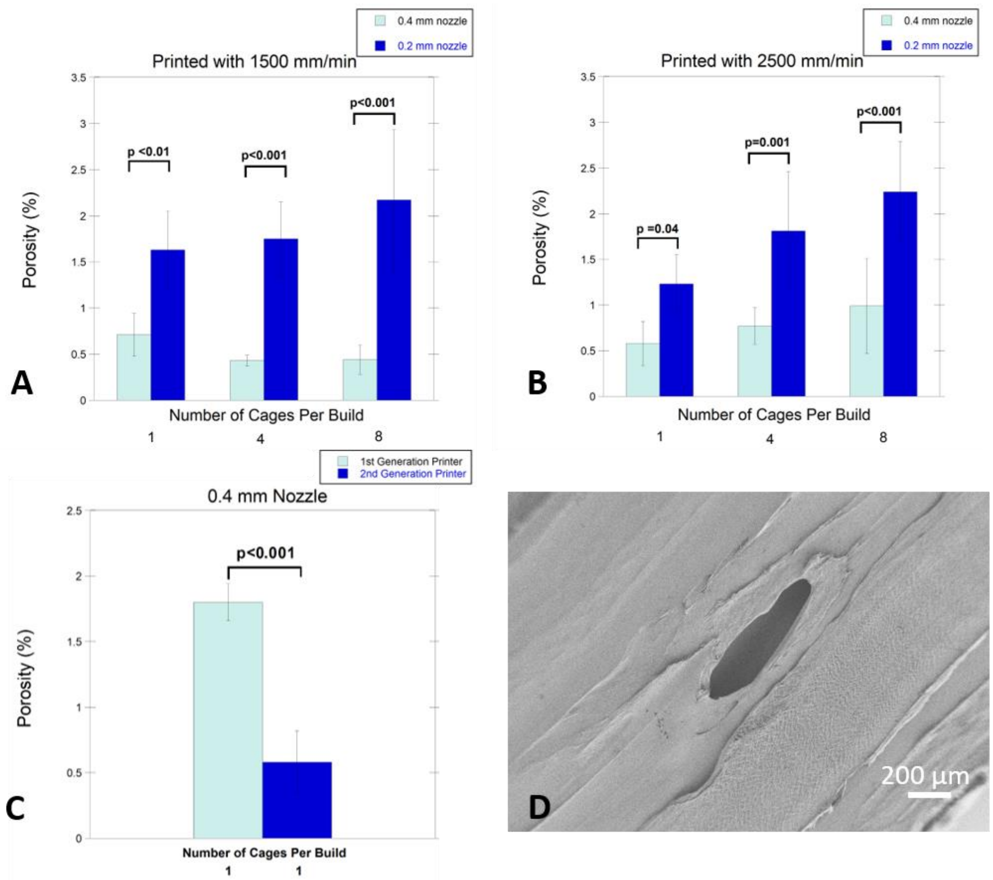

Figure 3. 5. Printing with a smaller nozzle resulted in higher porosity in 2nd generation cages when printed under both print speeds (A-B). 1st generation cages had significantly higher porosity than the 2nd generation cages (C). A representative pore from the surface of a 1st generation cage when printed with slower speed using the 1st generation FFF printer (D).

In addition to porosity, the failure mechanism observed for cages was interlayer delamination. Thus, in addition to diminishing entrapped micro-bubbles in filament prior to printing, a good layer bonding must be considered to reach the optimum structural integrity under load (Fig. 3.6).

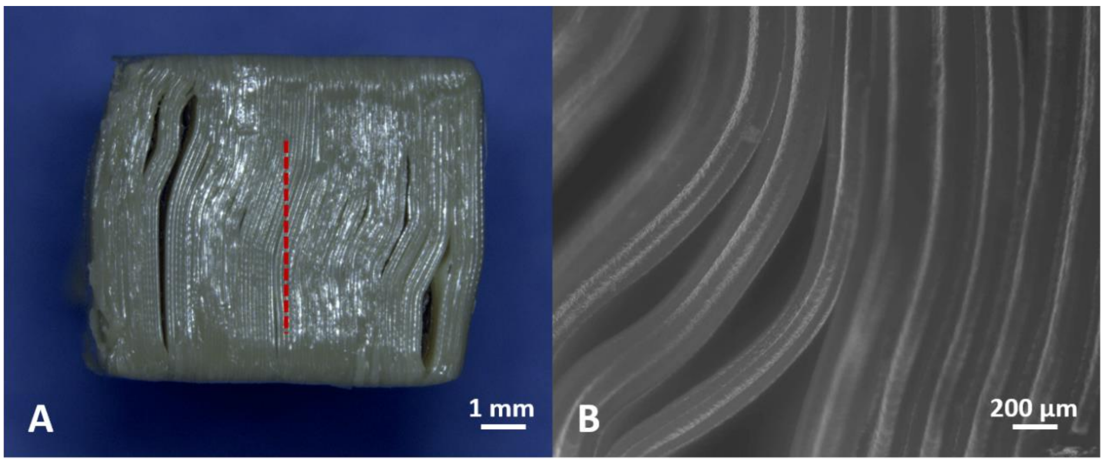

Figure 3. 6. The cracks were aligned parallel with the layers under compression loading condition (A). Interlayer debonding was observed as the failure mechanism of both FFF PEEK cage generations (B).

3.4.2 Mechanical Testing

3.4.2.1 Printer Generation

There was not a significant difference in ultimate load cages achieved, between the printer generations for both printing single (Fig. 3.7 (A)) and printing multiple (Fig. 3.7 (B)) ($p=0.32$ and $p=0.27$, respectively).

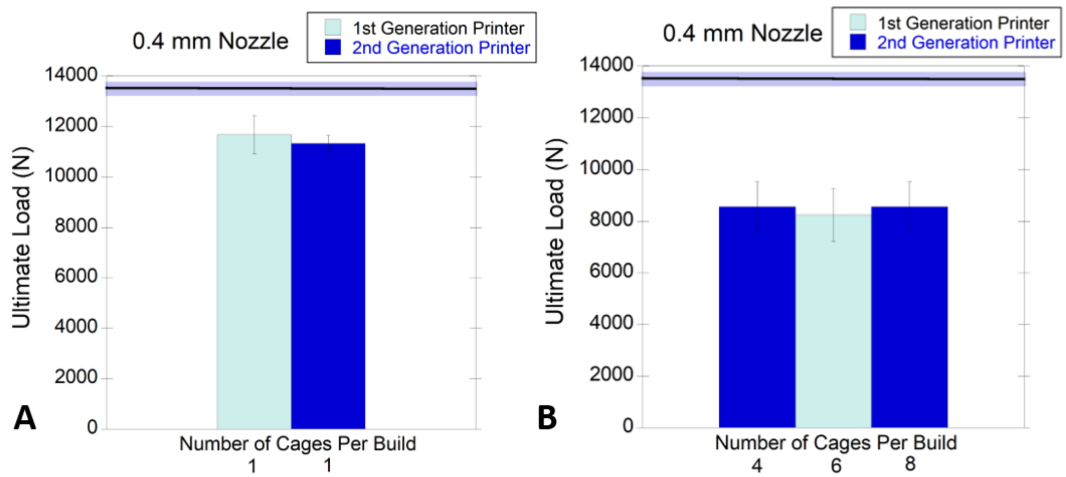

Figure 3. 7. There was not a significant difference observed between printer generations when single (A) and multiple (B) printed cages' ultimate load was compared. The purple bar in all graphs is showing the machined PEEK cage values with their mean and the standard deviation [25].

Furthermore, there was not a significant difference in the ultimate displacement of cages when printed multiple between 1st and 2nd generation printers. However, there was a significant difference in the ultimate displacement between the 1st and 2nd generation printers when single cages were printed. Cages printed with the 1st generation printer showed higher ultimate displacement compared to cages printed with the 2nd generation printer (mean difference=0.683 mm and p=0.002).

3.4.2.2 Print Speed

For 1st generation PEEK cages printed under four different speeds (from 1000 to 3000 mm/min), parts printed with the highest speed (3000 mm/min) showed significantly higher porosity ($p<0.001$ for all comparisons) which resulted in the decreased mechanical outcome (Table 3.3). However, printing up to 2500 mm/min did not affect cages' mechanical strength in both generations of FFF machines. There was not a significant difference when 1st generation cages were printed between 1000-2500 mm/min ($p>0.05$). In the same manner, there was not a significant difference between printing 1500 and 2500 mm/min for 2nd generation cages ($p>0.05$).

3.4.2.3 Printing single vs multiple

In addition to printing with two different nozzle sizes and at two different speeds, cages were printed at one, four, and eight at a time with both nozzle sizes to observe the effect of heat concentration on the layer strength of cages. It was observed that single prints achieved higher strength than multiple prints with the newer (2nd generation) FFF machine for both features (Fig. 3.8 (A)). In the same manner, only single prints with the newer (2nd generation) FFF system failed under higher mechanical loads than multiple prints with the older (1st generation) FFF system (Fig. 3.8 (B)).

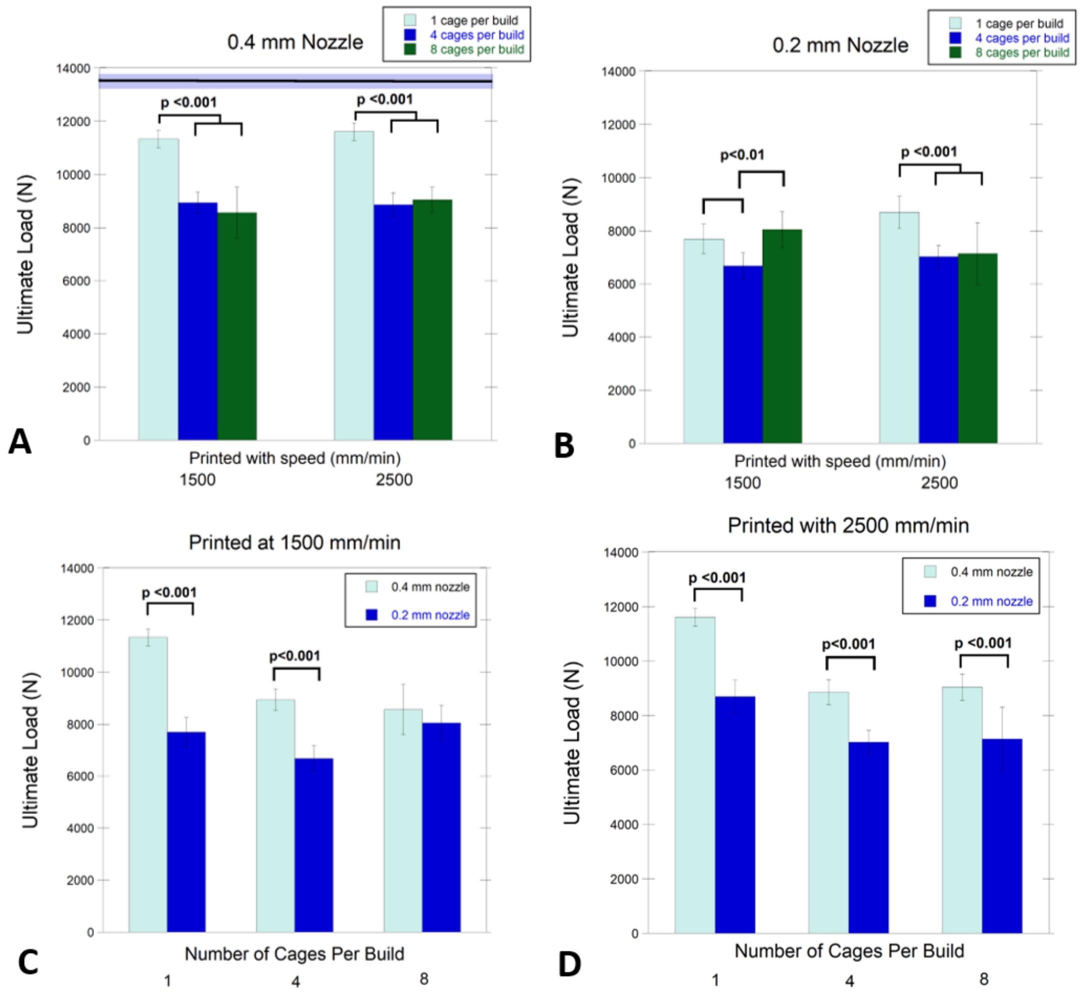

Figure 3. 8. Printing single cages achieved a higher ultimate load than printing multiple cages per build with a bigger nozzle diameter (A) (purple bar showing the machined PEEK cage values with its mean and the standard deviation) and smaller nozzle diameter under higher speed (B). Cages printed with the bigger nozzle diameter showed higher ultimate load than printing with the smaller nozzle diameter when printing single and four cages per build under slower speed (C), whereas for all printing conditions under higher speed (D).

3.4.2.4 Printhead (nozzle) diameter

One nozzle size was available for the 1st generation FFF machine, thus 1st generation FFF cages were printed only with a 0.4 mm nozzle. 2nd generation cages were 3D printed with 0.2- and 0.4-mm nozzle sizes. It was observed that cages printed with the smaller nozzle diameter failed at a lower maximum load than printed with the bigger nozzle diameter under higher speed (mean difference=2918, 1845, and 1901 N for 1, 4, and 8 cage per build, respectively and $p<0.001$ for all) (Fig. 3.8 (D)). Furthermore, under slower speed, cages printed with bigger nozzle diameter showed higher ultimate load than when printed with smaller nozzle for cages printed single and four per build (mean difference=3640 and 2262 N, $p<0.001$ for both, respectively) (Fig. 3.8 (C)). For all cage numbers printed (1, 4, and 8 per build), cages printed with a smaller nozzle diameter displaced less than cages printed with the bigger nozzle diameter under both slower and higher speed (under slower speed; mean difference= 0.91, 0.56, and 0.70 mm, under higher speed; mean difference= 0.77, 0.47 and 0.54 mm for 1, 4 and 8 cages per build, $p<=0.001$ for all).

3.4.2.5 Layer Thickness

There was no significant association between layer thickness and ultimate load for 2nd generation cages ($p=0.77$-0.89) (Fig. 3.9). However, cages that have thicker layers (0.2 mm) displaced more than cages that have thinner layers (0.1 mm) for the larger diameter nozzle (mean difference=0.848 mm and $p<0.001$). In the same manner, for the smaller diameter nozzle; cages that have thicker layers (0.1 mm) displaced more than cages that have thinner layers (0.05 mm) (mean difference=0.382 mm and p=0.01).

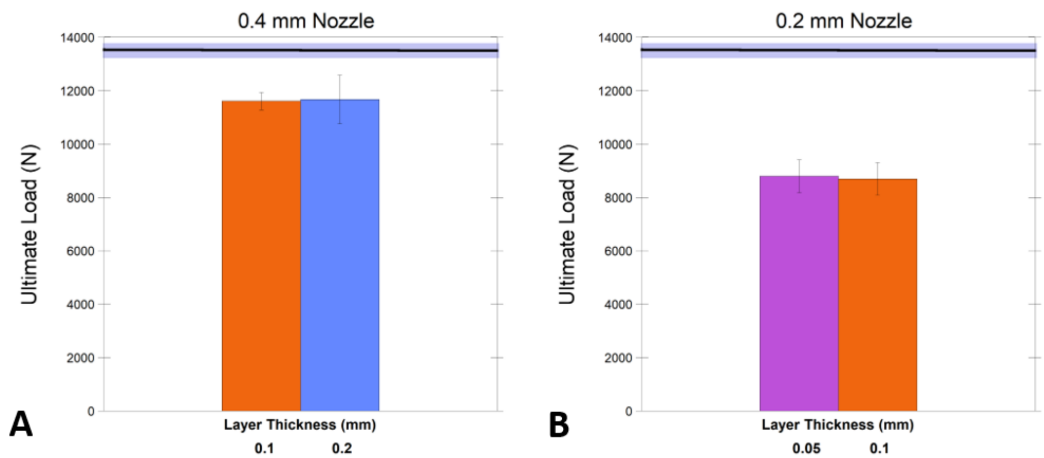

Figure 3. 9. Printing single cages with different layer thicknesses did not show a significant difference in cages' ultimate load for both nozzle diameters (0.4 mm nozzle (A) and 0.2 mm nozzle (B)) when printed under higher speed with the 2nd generation printer. The purple bar in all graphs is showing the machined PEEK cage values with their mean and the standard deviation.

3.5 Discussion

The purpose of this study was to investigate the effect of changing FFF parameters (that indirectly control the thermal conditions) on the mechanical properties and microstructure of standardized spinal cages printed with two generations of FFF machines. Specifically, under constant temperature conditions for the nozzle and printing bed, we varied the print speed and the number of cages fabricated per build for

1st generation cages and the nozzle size, print speed, layer thickness, and the number of cages fabricated per build for 2nd generation cages. We did not observe an association between the cage properties and crystallinity as a function of printing speed, further supporting the concept that print defects at the microscale, rather than crystalline morphology, are likely responsible for the differences between the FFF and machined PEEK cages. Additionally, we observed that, for the fixed temperature conditions of the present study, altering the FFF parameters did not change the failure mechanism of FFF cages. FFF cages still failed due to interlayer debonding. However, changing printing conditions that decrease the cooling time of a layer were found to improve the interlayer adhesion and strength of 3D printed PEEK cages. For example, there was a significant increase in cages' ultimate load when the cooling time of a layer was decreased by printing a single cage per build. Single 3D printed cages printed with both printer generations exceeded 10kN before failure and achieved 86% ultimate load of the traditionally machined PEEK cages. Furthermore, printing with a larger nozzle diameter resulted in stronger cages compared to printing with a smaller nozzle diameter. Although for finer details and microstructures a smaller nozzle diameter might be needed, one should be careful about the increase in printing time of the structures which leads to longer cooling times of layers. Moreover, despite increasing layer thickness decreased the print time of a single cage, it did not change cages' mechanical strength significantly. In the same manner, changing print speed (below 3000 mm/min) did not affect cages' strength, suggesting that the speeds investigated here did not drastically decrease the cooling time of a layer. Porosity was not affected by the print speed when it was below 3000 mm/min. However, printing with a smaller nozzle resulted in higher porosities in the cages. In one case, cages printed multiple per build had higher porosity compared to a cage printed one per build. Finally, there was not a difference in cages' strength when printed with two different PEEK printer generations. However, cages printed with the second-generation printer had less internal porosity.

Several limitations to the current study should be recognized here. The mechanical and microstructural outcomes of this study are associated with the current configuration of the printers and the constant temperature conditions employed in this study. One might expect different impacts on the mechanical properties and porosity of the 3D printed PEEK cages than observed in this study when a different printer and/or changes in the current configurations are employed. Nozzle diameter, print head speed, and ambient temperatures controlled during the print were restricted to the 3D printers' capabilities utilized in this study, which are the first two generations of Apium PEEK printers. In addition, it must be noted that layer thickness is restricted by the nozzle diameter, whereas the number of samples that can be printed at the same time is restricted by the print bed dimensions.

In previous studies investigating FFF, Rodriquez et al. [32] mentioned the importance of layer adhesion for the bulk 3D printed material's strength for a low temperature processing material (Acrylonitrile butadiene styrene (ABS)). PEEK is even more challenging compared to low-temperature processed materials regarding interlayer adhesion because of its high crystallization speed and melting point, which increases the thermal gradient between the layers. In a recent study on 3D printed PEEK dog bone specimens, the interlayer delamination phenomenon was mentioned for vertically built samples and emphasized the high thermal gradient in the build direction [26]. Thus, minimizing the thermal gradient across layers is important to 3D printed PEEK load-bearing implants to achieve better macro-mechanical properties.

It was shown in this study that decreasing the thermal gradient across layers could be possible by altering the structural and FFF parameters. For instance, the decision of printing one cage versus multiple cages per build significantly affected the cages' ultimate strength. The reason why single cages achieved significantly higher ultimate load is likely due to the ambient temperature of the print chamber being passively controlled. When printing a single cage, layers are directly laid over each other with relatively shorter cooling times. However, when multiple cages are being printed, after a layer is deposited for a cage, the nozzle moves to print the same layer for the other cages sequentially which significantly increases the cooling time of a layer.

Another manufacturing parameter that affected the thermal gradient through the cage and resulted in significantly different mechanical outcomes was the nozzle diameter. Printing with the smaller nozzle diameter (0.2 mm) caused lower ultimate strength in cages. Printing with a smaller nozzle diameter is not only increasing the cooling time of a layer, but it also causes a single line deposited to consolidate faster, since the volume of an extruded line through the nozzle is lower than a line extruded through a bigger nozzle. Thus, the lines, which later form a layer, cool faster, resulting in lower temperatures and poorer interlayer adhesion. This might have caused the higher porosity in cages when printed with a smaller nozzle diameter. The significant effect of the nozzle diameter (0.4, 0.6, and 0.8 mm) on interlayer cohesion was previously mentioned by Kuznetsov et al. [33]. They observed increased strength while printing with a larger nozzle when the layer thickness was kept constant. They also discussed increased layer height (ranging from 0.06 mm to 0.6 mm) decreased the strength of 3D printed polylactic acid (PLA) parts for all nozzles investigated. Similarly, Uddin et al. [34] showed that the smallest layer thickness (0.09 mm) amongst three layer thicknesses (0.09, 0.19, and 0.39 mm) revealed the highest failure strength when ABS was printed with a 0.4 mm diameter nozzle. Furthermore, Deng et al. [35] investigated three different layer thicknesses (0.2, 0.25, and 0.3 mm) for 3D printed PEEK dog-bone specimens. They optimized a set of variables including layer thickness and concluded that 0.2 mm layer thickness gave the best tensile properties. Tymrak et al. [36], on the other hand, mentioned no significant difference in ABS/PLA 3D printed parts when printed with three different layer heights (0.2, 0.3, and 0.4 mm). As in their research, we did not observe a significant layer thickness effect in 3D printed PEEK cages' ultimate strength in this study when single cages were printed. However, higher layer thickness resulted in larger displacements in cages, suggesting a more ductile behavior. This could be a sign that thicker layers transferred more heat and increased the interlayer adhesion, however, this effect was not strong enough to affect the failure load.

We found no association between the cages' ultimate strength and the print speeds investigated in this study when below 2500 mm/min. The results of the 1st generation cages suggested optimum print speeds below 2500 mm/min to 3D print PEEK, whereas increasing the print speed up to 3000 mm/min decreased the ultimate strength of 3D printed PEEK spinal cages and increased porosity to 20%. Similarly, Abbott et al. [37] investigated interlayer adhesion of ABS and found that increased print speed (from 600 mm/min to 3000 mm/min) resulted in lower yield strength. Likewise, Christiyan et al. [38] printed ABS composites with different print speeds (1800, 2000, and 3000 mm/min) and showed that the lowest print speeds resulted in the highest tensile and flexural strength.

In the present study, the cages' mechanical and microstructure were evaluated by altering the structural and manufacturing parameters to investigate the indirect effect of thermal conditions during the print. Nonetheless, thermal conditions (nozzle and bed temperatures) were different for 1st and 2nd generation PEEK printers while printing PEEK cages. Although these temperatures were different for these two printer generations, the cages' ultimate strength did not change when the same print builds (single vs multiple) were compared. However, 1st generation cages displaced more which suggests slightly more ductile behavior. This could be because of the build volume difference between the printer generations, in which the 1st generation printer had a smaller build volume that could result in better heat preservation.

In summary, this study investigated the structural and FFF parameters which indirectly affect the thermal conditions during the print for 3D printed PEEK spinal cages. The results of this study support our hypothesis which was the adjusting parameter of FFF technology will enhance the interlayer adhesion of 3D printed cages, thus its macro mechanical properties. Cages when printed one per build with both generations achieved 86% ultimate strength of the machined PEEK cages. For both generations, printing multiple cages per build was associated with lower ultimate strength and poorer interlayer adhesion. Although there was a difference between the processing temperatures of the 1st and 2nd generation of PEEK printers, interestingly, the cages' strength was not associated with the printer generation. Print speeds below 3000 mm/min did not affect the cages' mechanical and microstructural outcomes. Moreover, printing with a bigger nozzle diameter increased the ultimate load of the cages and decreased the undesired porosity regardless of the layer thickness.

3.6 References

1. ASTM Standard F2077-14, *Test Methods For Intervertebral Body Fusion Devices*. 2014, ASTM International.
2. McGilvray, K.C., et al., *Evaluation of a polyetheretherketone (PEEK) titanium composite interbody spacer in an ovine lumbar interbody fusion model: biomechanical, microcomputed tomographic, and histologic analyses.* Spine J, 2017.
3. Asil, K. and C. Yaldiz, *Retrospective Comparison of Radiological and Clinical Outcomes of PLIF and TLIF Techniques in Patients Who Underwent Lumbar Spinal Posterior Stabilization.* Medicine (Baltimore), 2016. **95**(17): p. e3235.
4. Grob, D., S. Daehn, and A.F. Mannion, *Titanium mesh cages (TMC) in spine surgery.* Eur Spine J, 2005. **14**(3): p. 211-21.
5. Mendenhall, S., *Spinal Industry Update.* 2017. **28**(4): p. 4-6.
6. Vadapalli, S., et al., *Biomechanical rationale for using polyetheretherketone (PEEK) spacers for lumbar interbody fusion-A finite element study.* Spine (Phila Pa 1976), 2006. **31**(26): p. E992-8.
7. Duncan, J.W. and R.A. Bailey, *An analysis of fusion cage migration in unilateral and bilateral fixation with transforaminal lumbar interbody fusion.* European Spine Journal, 2013. **22**(2): p. 439-445.
8. Evans, N.T., et al., *High-strength, surface-porous polyether-ether-ketone for load-bearing orthopedic implants.* Acta Biomater, 2015. **13**: p. 159-167.
9. Torstrick, F.B., et al., *Getting PEEK to Stick to Bone: The Development of Porous PEEK for Interbody Fusion Devices.* Techniques in Orthopaedics, 2017. **32**(3): p. 158-166.
10. Eltorai, A.E., E. Nguyen, and A.H. Daniels, *Three-Dimensional Printing in Orthopedic Surgery.* Orthopedics, 2015. **38**(11): p. 684-7.
11. Gibbs, D.M., et al., *Hope versus hype: what can additive manufacturing realistically offer trauma and orthopedic surgery?* Regen Med, 2014. **9**(4): p. 535-49.
12. Martelli, N., et al., *Advantages and disadvantages of 3-dimensional printing in surgery: A systematic review.* Surgery, 2016. **159**(6): p. 1485-1500.

13. Provaggi, E., J.J.H. Leong, and D.M. Kalaskar, *Applications of 3D printing in the management of severe spinal conditions.* Proc Inst Mech Eng H, 2017. **231**(6): p. 471-486.

14. Tack, P., et al., *3D-printing techniques in a medical setting: a systematic literature review.* Biomed Eng Online, 2016. **15**(1): p. 115.

15. Ventola, C.L., *Medical Applications for 3D Printing: Current and Projected Uses.* P t, 2014. **39**(10): p. 704-11.

16. Sun, Q., et al., *Effect of processing conditions on the bonding quality of FDM polymer filaments.* Rapid Prototyping Journal, 2008. **14**(2): p. 72-80.

17. Thomas, J. and J. Rodriguez. *Modeling the fracture strength between fused-deposition extruded roads*. in *Solid Freeform Fabrication Symposium Proceeding*. 2000. Austin, TX, USA.

18. Drummer, D., S. Cifuentes-Cuéllar, and D. Rietzel, *Suitability of PLA/TCP for fused deposition modeling.* Rapid Prototyping Journal, 2012. **18**(6): p. 500-507.

19. Xinhua, L., et al., *An investigation on distortion of PLA thin-plate part in the FDM process.* The International Journal of Advanced Manufacturing Technology, 2015. **79**(5): p. 1117-1126.

20. Zhang, Y. and Y. K. Chou, *Three-dimensional finite element analysis simulations of the fused deposition modelling process.* Proceedings of the Institution of Mechanical Engineers, Part B: Journal of Engineering Manufacture, 2006. **220**(10): p. 1663-1671.

21. Wu, W.Z., et al., *Manufacture and thermal deformation analysis of semicrystalline polymer polyether ether ketone by 3D printing.* Materials Research Innovations, 2014. **18**(S5): p. 12-16.

22. Vaezi, M. and S. Yang, *Extrusion-based additive manufacturing of PEEK for biomedical applications.* Virtual and Physical Prototyping, 2015. **10**(3): p. 123-135.

23. Rahman, K.M., T. Letcher, and R. Reese. *Mechanical Properties of Additively Manufactured PEEK Components Using Fused Filament Fabrication*. in *ASME 2015 International Mechanical Engineering Congress and Exposition*. 2015. Houston, Texas, USA: ASME.

24. Cicala, G., et al., *Engineering thermoplastics for additive manufacturing: a critical perspective with experimental evidence to support functional applications.* Journal of Applied Biomaterials & Functional Materials, 2017. **15**(1): p. e10-e18.

25. Basgul, C., et al., *Structure–property relationships for 3D-printed PEEK intervertebral lumbar cages produced using fused filament fabrication.* Journal of Materials Research, 2018: p. 1-12.

26. Arif, M.F., et al., *Performance of biocompatible PEEK processed by fused deposition additive manufacturing.* Materials & Design, 2018. **146**: p. 249-259.

27. Li, H., et al., *Preparation of high performance adhesives matrix based on epoxy resin modified by bis-hydroxy terminated polyphenylene oxide.* Journal of Adhesion Science and Technology, 2018. **32**(11): p. 1224-1238.

28. Kurtz, S.M., *Chapter 2 - Synthesis and Processing of PEEK for Surgical Implants*, in *PEEK Biomaterials Handbook*. 2012, William Andrew Publishing: Oxford. p. 9-22.

29. Green, S. and J. Schlegel, *A Polyaryletherketone Biomaterial for use in Medical Implant Applications*. 2001: Lancashire, UK.

30. ASTM Research Report: F04-1014, *Interlaboratory Study to Establish Precision Statements for ASTM F2077*. 2014.

31. International Organization for Standardization. *ISO/IEC 17025:2005*. [cited 2018 6 Feb]; Available from: https://www.iso.org/standard/39883.html.

32. Rodriguez, J.F., Thomas, J.P. , Renaud, J.E. *Maximizing the Strength of Fused-deposition ABS plastic parts*. in *10th, Solid freeform fabrication symposium*. 1999. Austin, TX.

33. Kuznetsov, V.E., et al., *Strength of PLA Components Fabricated with Fused Deposition Technology Using a Desktop 3D Printer as a Function of Geometrical Parameters of the Process.* Polymers, 2018. **10**(3): p. 313.

34. Uddin, M.S., et al., *Evaluating Mechanical Properties and Failure Mechanisms of Fused Deposition Modeling Acrylonitrile Butadiene Styrene Parts.* Journal of Manufacturing Science and Engineering, 2017. **139**(8): p. 081018.

35. Deng, X., et al., *Mechanical Properties Optimization of Poly-Ether-Ether-Ketone via Fused Deposition Modeling.* Materials (Basel, Switzerland), 2018. **11**(2): p. 216.

36. Tymrak, B.M., M. Kreiger, and J.M. Pearce, *Mechanical properties of components fabricated with open-source 3-D printers under realistic environmental conditions.* Materials & Design, 2014. **58**: p. 242-246.

37. Abbott, A.C., et al., *Process-structure-property effects on ABS bond strength in fused filament fabrication.* Additive Manufacturing, 2018. **19**: p. 29-38.

38. Christiyan, K.G.J., U. Chandrasekhar, and K. Venkateswarlu, *A study on the influence of process parameters on the Mechanical Properties of 3D printed*

ABS composite. IOP Conference Series: Materials Science and Engineering, 2016. **114**: p. 012109.

Chapter 4: Development of a heat transfer-based non-isothermal layer healing model to improve the interlayer strength for 3D printed PEEK implants

4.1 Abstract

FFF as an AM method for PEEK has established a promising future for medical applications so far, however interlayer delamination as a FFF implant's failure mechanism has raised critical concerns. This study aimed to (1) develop a one-dimensional (1D) heat transfer model to calculate the layer and interlayer temperatures by considering the nature of 3D printing for a FFF PEEK build; (2) utilize the temperature distribution of interlayers in a non-isothermal healing model to predict the healing degree through layers of the FFF PEEK part, and (3) investigate the main temperature effects of the FFF system on layer healing, including the effect of the print bed, nozzle, and chamber temperatures. A 1D heat transfer model (HTM) was developed with initial and boundary conditions by assuming the dominant heat loss in the layer build direction. Boundary temperatures and heat transfer characteristics were considered to be constant in the model. The initial conditions were as follows: (1) The layer temperature was equal to the nozzle temperature once extruded, (2) The conduction boundary for the first layer was the print bed with a constant temperature. The boundaries for each layer were defined and updated by the nature of the printing process. The temperature distributions calculated from HTM were implemented in the non-isothermal degree of healing model. The degree of healing values for each interlayer point were obtained for the FFF PEEK part. The upper layers in reference to the print bed exhibited a higher degree of healing compared to the lower layers.

Increasing the print bed temperature increases the healing of the layers allowing more layers to heal 100%. The nozzle temperature has the biggest effect on the layer healing and under certain nozzle temperature, none of the layers are healing properly. Finally, although environment temperature has less effect on the lower layers that are closer to the print bed, 100% healed layer number increased when the chamber temperature is increasing. This chapter provides the theoretical model that will enable the parameter optimization to achieve sufficiently healed layers through FFF builds, thus enhancing the macro mechanical properties of FFF PEEK implants.

4.2 Introduction

Additive Manufacturing (AM), more commonly known as three-dimensional (3D) printing, has emerged as a new frontier for medical device manufacturing [1]. Although relatively new, AM has already been used to fabricate medical devices and surgical instruments from a range of metallic and polymeric materials [1-6]. Spinal surgery is one of the therapeutic areas in which there has been early interest in AM. Additive manufacturing techniques, including FFF, have been successfully used to manufacture polyetheretherketone (PEEK) spinal implants [7-12], including spinal cages [7-9]. Although FFF PEEK has shown its potential for point-of-care AM, layer delamination has been observed as the failure mechanism for FFF PEEK spinal implants as indicated in the previous chapters. It is important to address the concerns on the mechanical failure mechanism of FFF PEEK spinal implants to open the path for further research questions on possible FFF PEEK applications in medicine. This failure mechanism is strongly associated with the thermal conditions controlled by direct and indirect thermal parameters [7, 13]. In FFF systems, extruded lines build up the layers which are laid consecutively on top of each other until they form the final part. During these processes, heat transfer occurs between the deposited layers as well as from layers into the print bed and the print environment. These heat transfer processes determine the temperature history of the merging layers, which plays a critical role in the unity of the part and its mechanical strength. It is important to understand the thermal history in FFF PEEK to enhance the layer adhesion for an FFF implant with superior mechanical properties.

Researchers have previously analyzed the thermal conditions of FFF systems for low-temperature polymers via HTM to understand the challenges in FFF such as warping, adhesion, and layer delamination [13-19]. Most of these studies focused on the extruded fiber (filament), which creates the layers, temperature, and adhesion [13-15]. Thomas et al. [14] obtained the interface temperatures of filaments via analytically solving a two-dimensional (2D) heat transfer model to predict the fracture toughness of the FFF ABS parts. As expected, they stated that prolonging the fiber solidification times increases the bonding strength between the fibers. Similarly, a study combined a one dimensional (1D) HTM to estimate the cooling profile and a polymer sintering model to investigate the bond formation between the filaments in FFF ABS parts [15]. Depending on the quantitative predictions of filament bonding degree, they concluded that increasing the nozzle temperature (T_N) affects the filament temperature profile more than chamber temperature (T_C). In the same manner, Costa et al. [13] investigated the filament adhesion on FFF ABS parts via a 1D HTM to estimate the filament temperatures and healing. In addition to low-temperature polymer studies, filament temperature distribution was assessed with the help of a 1D HTM to investigate the surface roughness of FFF PEEK parts [20]. Other than exploring the filament temperature distribution, HTM is recognized to affect the layer temperatures in an FFF build. Compton et al. [17] examined the heat management problem of the large-scale CFR-ABS FFF with a 1D HTM for complications such as warping and cracking. Contrary to Bellehumeur et al. [15], they found that the ambient temperature (T_C) has the largest effect on increasing the size of an object that can be successfully printed.

Moreover, some studies utilized the layer temperature distribution gathered from HTMs into a non-isothermal degree of healing (DOH) formula, defined by Yang et al. [21], to assess the layer healing in low-temperature FFF builds [13, 18]. Non-isothermal degree of healing is explored to explain the healing between the layers of FFF builds since the layer temperatures during printing and cooling processes are not constant while healing occurs. Costa et al. [13] showed the filament adhesion locally, where below 100% healing is indicated as poor adhesion, for FFF ABS parts. Furthermore, Yin et al. [18] studied the filament bonding strength of two different low-temperature materials (TPU and ABS).

Improved interlayer strength to enhance the macro mechanical properties of FFF PEEK implants is necessary by addressing the issue of interlayer delamination phenomena of FFF AM. Although there have been efforts to investigate the filament bonding in FFF parts on low-temperature polymers via heat transfer based non-isothermal degree of healing models, there are some drawbacks in the previous models. First, despite the layer delamination failure in FFF builds, previous models were mainly focused on the filament temperature distribution rather than investigating the layer temperatures. Additionally, there are controversial conclusions for the main temperature effects on the filament bonding in low-temperature FFF parts. Thus, a comprehensive model is crucial to understand the heat transfer fundamentals for parameter optimization to improve the layer healing on FFF PEEK implants.

In this study, we hypothesized that the enhancement of key FFF process temperatures (print bed (T_B), chamber (T_C), and nozzle temperatures (T_N)) would yield a higher degree of healing, and hence improved interlayer adhesion, across the FFF PEEK layers. Hence, we hypothesized: (1) a 1D heat transfer model would predict the temperature distributions of FFF PEEK layers via simulating the FFF process; and (2) that the layer temperature distribution achieved from the HTM, when integrated with a non-isothermal polymer healing model, would improve the quality of interlayer bonding between adjacent layers in a FFF PEEK construct.

4.3 Materials & Methods

4.3.1 Heat Transfer Model (HTM)

Here a 1D transient heat transfer model is presented to predict the temperatures of layers and interlayers by simulating the deposition process in 3D printing PEEK parts. The initial geometry (Fig. 4.1 (A)) is inspired by the XZ plane of the standard cage design used in the previous chapter (Fig. 3.1). The two simplifications are justified by the geometric characteristics of the extruded layer: (1) Considering the 0.2 mm layer height while printing with 0.4 mm nozzle diameter (Table 4. 1), the layer dimensions will be 0.2x10x10 mm^3. Since the layer dimensions in the y and z directions are 50 times bigger than the x-direction, the heat transfer from a layer is considered to occur at most in the x-direction (Fig. 4.1 (A)). Thus, a 1D heat transfer model is employed here which is the substantial assumption of the model (Fig. 4.1 (B)), (2) It is assumed that a uniform temperature distribution throughout the cross-section (i.e., variations in the temperature across the layer thickness are not taken into consideration).

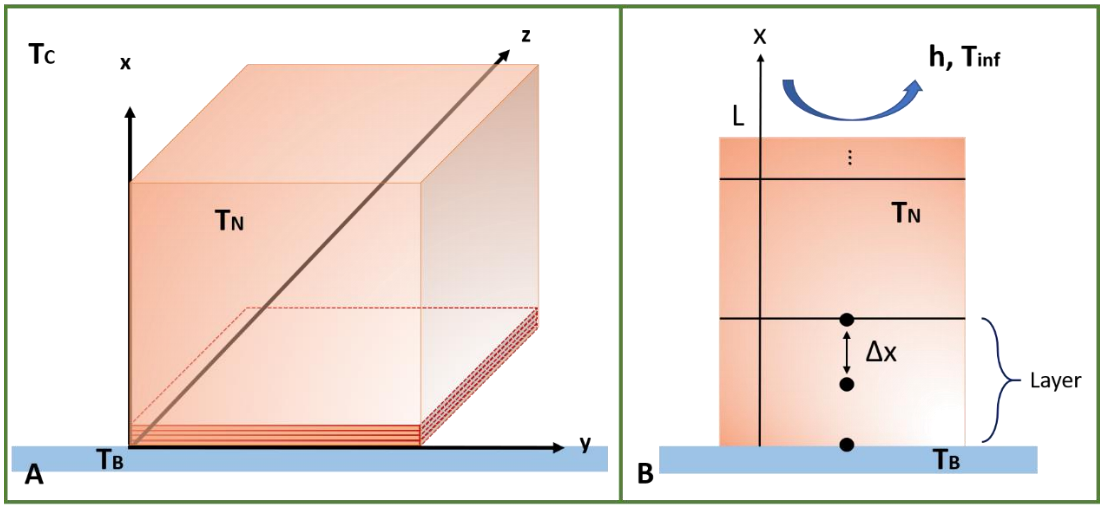

Figure 4. 1. In the physical FFF PEEK process, layers in nozzle temperature (T_N) are deposited on top of each other onto a print bed (T_B) inside a chamber (T_C=T_{inf}) (A). In the 1D HTM, a layer will have either the print bed (T_B) or another layer underneath as the conduction boundary and on top, the chamber temperature with a constant convection coefficient (h) will be effective as the convection boundary until a new layer is deposited (B).

Three main temperatures are affecting the heat transfer through layers in this model, which are, print bed temperature (T_B); material deposition temperature, referred to as the nozzle temperature, (T_N); and the environment temperature in the closed chamber where the part is printed (T_C). T_N and T_B are selected based on the FFF machine settings that were used to print FFF PEEK cages in the previous chapter and a presumptive value, that will be validated in the next chapter, is selected for T_C (Table 4. 1). These temperatures are considered to be constant through the print. A layer is examined as a rectangle bar stacked on top of each other at certain time intervals, which is indicated as layer deposition time in the model. Layer deposition time is calculated experimentally which is the time spent to print a layer of the initial cube geometry at 2000 mm/min.

Table 4. 1. Parameters used in the heat transfer model.

Parameters	**Value**
Thermal conductivity, k (W/m,K)	0.29
Specific heat capacity, cp (J/kg.K)	1957
Density, ρ (kg/m^3)	1300
Natural convection coefficient, h ($W/m^2.K$)	17.5
Part length, L (m)	0.01
Number of layers	50
Layer height, d (m)	0.0002
Distance between the nodes, Δx (m)	0.0001
Number of nodes, n	101
Layer deposition time, t (sec)	10
Timestep, Δt (sec)	0.038
Cooldown time (sec)	300
Initial Temperature, T_N (°C)	485
Bed Temperature, T_B (°C)	130
Chamber Temperature, T_C (°C)	80

To track both the internal layer temperatures and the boundary temperatures of each layer through the print, three nodes are defined in a layer, which are 0.1 mm apart from each other (Δx) (Fig. 4.1 (B) & Eq. 8).

$$\Delta x = \frac{layer\ height}{(nodes\ per\ layer - 1)} \tag{8}$$

Initial conditions (IC) are as follows: For a single layer, the initial temperature upon deposition is assumed uniform and equal to the nozzle temperature (T_N). The temperature at the bottom surface of the specimen is set to be equal to the temperature of the building stage (T_B), while for other surfaces exposed to air, the convection boundary conditions are applied. The boundary conditions (BC) of a layer are defined specifically and updated for all layers after each layer deposition to simulate the 3D printing process (Fig 4.2). The derivation of the convection coefficient (h), applied in convection BC equations, will be explained in detail later in this chapter (Appendix B).

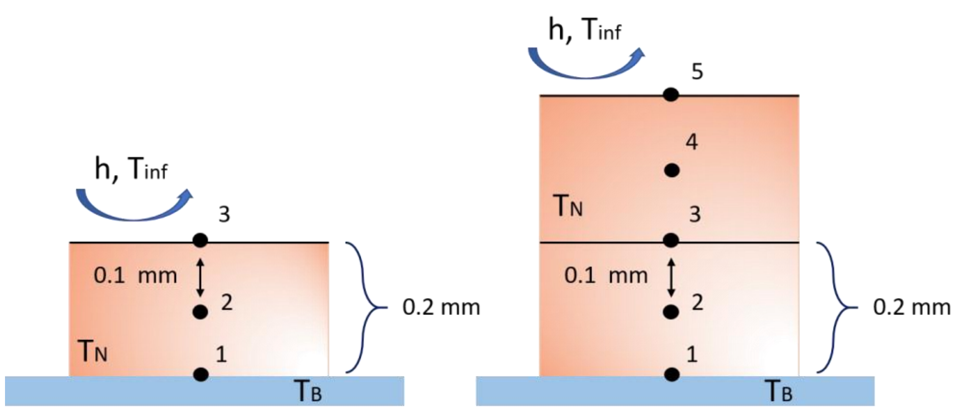

Figure 4. 2. For instance, the first layer boundaries will be the print bed at the bottom (node 1 = conduction BC) and the air on top (node 3 = convection BC), until the second layer is deposited. Once the 2nd layer is deposited, 'node 3' is an interlayer point and becomes conduction BC both for the first layer and the second layer.

The unsteady-state heat conduction equation in one-dimensional rectangular coordinate system to obtain the temperature distribution for constant thermophysical properties is provided by [22]

$$\frac{\partial^2 T}{\partial x^2} = \frac{1}{\alpha}\frac{\partial T}{\partial t} \tag{9}$$

The thermal diffusivity constant (α) is calculated through three material-dependent parameters by

$$\alpha = \frac{k}{\rho . c_p} \tag{10}$$

The density (ρ) and coefficient of thermal conductivity (k) of PEEK are accessed from material datasheets of the bulk material which is the same material as the filament used in the previous chapter [23]. The specific heat capacity (c_p) for the glass transition and melting temperatures of PEEK were calculated according to Eq. 11 [24] and the average value was employed in the model (Table 4. 1).

$$c_p = 0.496T + 308.15(\pm 0.1\%) \tag{11}$$

If we approximate the derivatives in Eq.9, the heat conduction equation can be also written in the finite-difference form. The time (t) and location (x) domains can be gridded with the small intervals of Δ*x* and Δ*t* (Fig. 4.3).

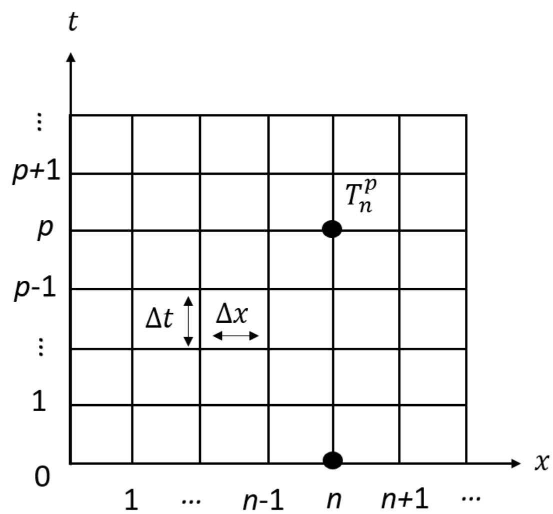

Figure 4. 3. For the nodes defined in the FFF part (n, n+1, …), temperature distributions will be calculated in each time step (Δ*t*) (p, p+1, …) as denoted in the one-dimensional, unsteady-state problems.

The second-order partial derivative with respect to location (x) in Eq. 9 is approximated as

$$\left.\frac{\partial^2 T}{\partial x^2}\right|_t \cong \frac{T_{n+1}^p - 2T_n^p + T_{n-1}^p}{(\Delta x)^2} \tag{12}$$

Forward differencing is selected to solve the time derivative of Eq.9 According to the explicit method (forward differencing), the time derivative in Eq. 2 is approximated at the location 'x' as

$$\left.\frac{\partial T}{\partial t}\right|_x \cong \frac{T^{p+1} - T^p}{\Delta t} \tag{13}$$

Equations 12 and 13 are plugged into Equation 9 to obtain the governing Equation 14.

$$\frac{T_{n+1}^p - 2T_n^p + T_{n-1}^p}{(\Delta x)^2} = \frac{1}{\alpha}\frac{T_n^{p+1} - T_n^p}{\Delta t} \tag{14}$$

Based on Eq. 14, if the temperatures are known at locations *n*-1, *n*, and *n*+1 at a certain time '*p*', the temperatures after a time increment (Δt) (T_n^{p+1}) can be calculated by rearranging the equation:

$$T_n^{p+1} = \left[1 - \frac{2\alpha\Delta t}{(\Delta x)^2}\right] T_n^p + \frac{\alpha\Delta t}{(\Delta x)^2}\left(T_{n+1}^p + T_{n-1}^p\right) \tag{15}$$

The above equation (15) is applicable to the present conduction boundary conditions. If there is convection on the boundary, the boundary condition at $x = L$ is defined by

$$-k\left.\frac{\partial T}{\partial x}\right|_{x=L} = h[T(L) - T_\infty] \tag{16}$$

The convection boundary condition can be written with the finite-difference approximation as

$$k\frac{T_{m-1}^{p}-T_{m}^{p}}{\Delta x}+h\left(T_{\infty}-T_{m}^{p}\right)=\rho c\frac{\Delta x}{2}\frac{T_{m}^{p+1}-T_{m}^{p}}{\Delta t} \tag{17}$$

And can be rearranged as

$$T_{m}^{p+1}=\frac{\alpha\Delta t}{(\Delta x)^2}\left\{\left[\frac{(\Delta x)^2}{\alpha\Delta t}-2\frac{h\Delta x}{k}-2\right]T_{m}^{p}+2T_{m-1}^{p}+2\frac{h\Delta x}{k}\ T_{\infty}\right\} \tag{18}$$

Equation 15 and 18 are used to calculate the temperatures at the nodes depending on the boundary conditions at each time step.

4.3.1.1 Stability

Forward-difference approximation solutions are not always stable. To ensure the stability of Eq. 15, the below condition must be fulfilled.

$$\frac{\alpha\Delta t}{(\Delta x)^2}\leq 0.5 \tag{19}$$

In addition, the stability criteria of Eq.18 is

$$\frac{(\Delta x)^2}{\alpha\Delta t}\geq 2\left(\frac{h\Delta x}{k}+1\right) \tag{20}$$

If these conditions are not satisfied, the second law of thermodynamics is violated, and the solution becomes unstable [22]. Since $\alpha, h, k,$ and Δx are already defined, Δt is calculated in accordance with these two stability conditions for the model.

4.3.1.2 Natural Convection Coefficient (h)

The natural convection coefficient, h can be calculated as

$$h = \frac{Nu_L k_f}{L} \tag{21}$$

where Nu_L is the Nusselt number, L is the plate length and k_f is the fluid (i.e., air) thermal conductivity. The Nusselt number for a vertical plate is estimated by [25]

$$Nu_L = \left[0.825 + 0.387\left(\frac{Ra^{1/6}}{[1 + (0.492/Pr)^{9/16}]^{8/27}}\right)\right]^2 \tag{22}$$

Rayleigh number, Ra, is defined as

$$Ra = Gr.Pr \tag{23}$$

Prandtl number (Pr) is the ratio between the fluid kinematic viscosity (v) and the thermal diffusivity in a fluid (α_f) which can be calculated via Eq. 10 (Table 4.2).

$$Pr = v/\alpha_f \tag{24}$$

Table 4. 2. Parameters used to calculate the natural convection coefficient (h).

Parameters	**Value**
Fluid Temperature, T_∞ (℃)	80
Surface Temperature, T_s (℃)	485
Wall thickness, L (m)	0.01
Fluid density, ρ_s (kg/m³)	1.214
Fluid kinematic viscosity, v (m²/s)	$1.493*10^{-5}$
Fluid specific heat capacity, c_p (J/kg.K)	1005
Fluid thermal conductivity, k (W/m,K)	0.0256
Fluid thermal expansion coefficient, β ($\frac{1}{\text{K}}$)	$3.44*10^{-3}$
Force of gravity, g (m/s²)	9.81
Prandtl number, P_r	0.71
Grashof number, G_r	43147
Average Rayleigh number, R_a	30634
Average Nusselt number, Nu_L	6.97

Grashof number (Gr) is the ratio of buoyant to viscous forces in a fluid and calculated as

$$Gr = \frac{g\beta(T_s - T_\infty)L^3}{v^2} \tag{25}$$

I developed custom scripts using MATLAB 2018b to calculate the heat transfer coefficient and solve the heat transfer model (Appendix B). The temperature history from the heat transfer model will be then implemented to an interface healing model to calculate the degree of layer healing, as further described in the following section.

4.3.2 Degree of Healing Model

The temperature history of interlayers calculated with the HTM is used to determine the degree of healing between two layers of PEEK parts produced via FFF (Fig. 4.4).

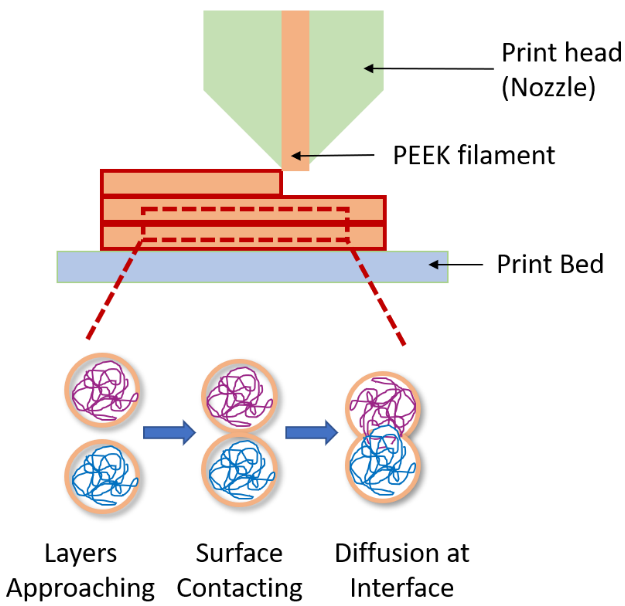

Figure 4. 4. While PEEK layers are consecutively deposited during the FFF process, healing between two layers starts with the interdiffusion across interfacial areas in contact that affects the development of interlayer adhesion strength.

Yang and Pitchumani [26] defined the non-isothermal degree of healing as the ratio of the instantaneous bond strength to the ultimate bond strength,

$$Dh(t) = \frac{\sigma}{\sigma_\infty} = \left[\int_0^t \frac{1}{t_w(T)}\,dt\right]^{1/4} \tag{26}$$

Which is explained based on the reptation theory as a function of time, where t_w is temperature-dependent welding time and the temperature is changing with time. The assumption for this model is that intimate contact is already achieved at the interface when the upper layer is completely extruded. The welding time can be calculated experimentally with the Arrhenius Equation [21].

$$t_w = A\,exp\left[\frac{E}{R}\left(\frac{1}{T} - \frac{1}{T_{ref}}\right)\right] \tag{27}$$

A and *E* are material constants, which are the rate of healing at critical bond temperature (T_{ref}) and the activation energy for the healing process, respectively. In this study, the welding function formula previously calculated for PEEK by Lee and Springer is used [27].

$$t_w = \left(\frac{1}{44.1}\,exp\,\frac{3810}{T}\right)^4 \tag{28}$$

Interlayer degree of healing values were calculated for the FFF PEEK construct under the conditions that were previously studied for FFF PEEK cages. Additionally, three main temperatures in the FFF system (T_B, T_N, T_C,) were varied to evaluate their effects on the healing of FFF PEEK layers. Five different values with 20℃ increments, 20℃ decrements, and 40℃ increments for the print bed, nozzle, and chamber temperatures, respectively, are investigated while all other parameters, except time step and convection coefficient, are kept constant. Adjusting the chamber temperature means changing the fluid temperature that is employed in the natural convection coefficient (h) calculation. For three conditions where the nozzle temperature is modified, the time step is gradually decreased to be able to detect points between the extrusion and melting temperatures which were otherwise not detectable with bigger time steps. Custom scripts developed for DOH were implemented into the HTM model in MATLAB 2018b (Appendix A).

4.4 Results

4.4.1 Heat Transfer Model

Both interlayer (n=49) and layer (n=50) temperature distributions are obtained for a 10 mm high 3D printed PEEK construct with 50 layers via HTM (Fig. 4.5).

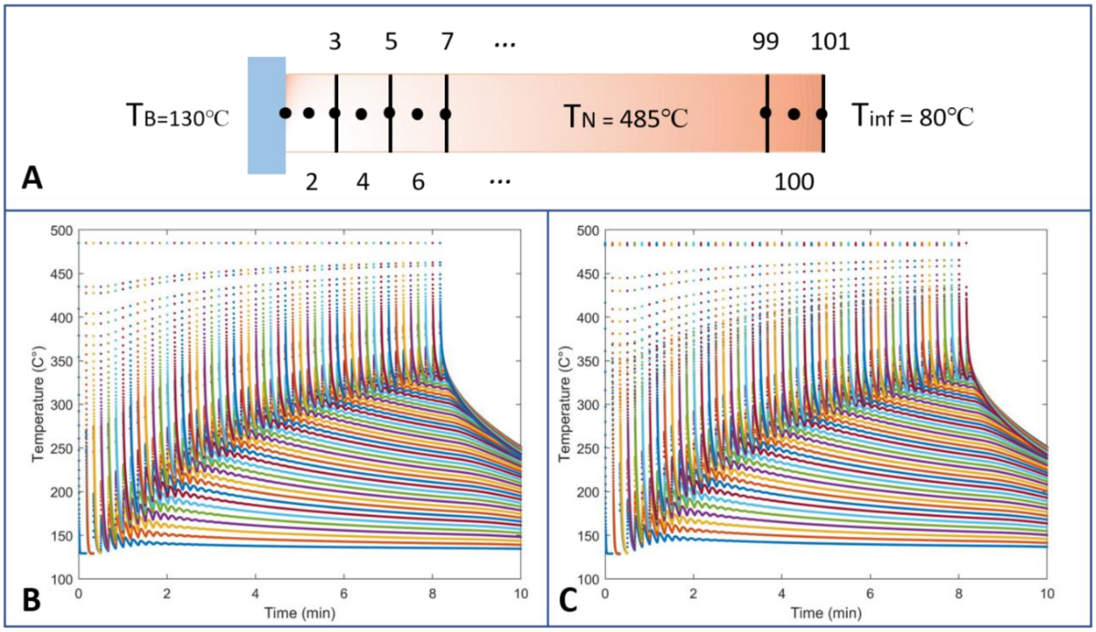

Figure 4. 5. Temperature distributions of nodes, in which the 1st node is the conduction boundary condition from the print bed and the 101st node is the convection boundary condition from the print chamber once the part is fully printed (A), are predicted through the part via HTM for layers (node 2 to 100) (B) and interlayers (node 3 to 99) (C).

It is observed that both layer and interlayer temperatures are decreasing faster when they are closer to the print bed (130℃). The temperatures are staying higher for the layers which are closer to the top of the object, where the convection boundary condition is effective. In addition, the reheating effect of consecutive layers is readily simulated (Fig. 4.6). Depending on the layer and/or interlayer, the first consecutive layer's effect is the biggest and it gradually decreases. Finally, after ten layers that effect is almost invisible.

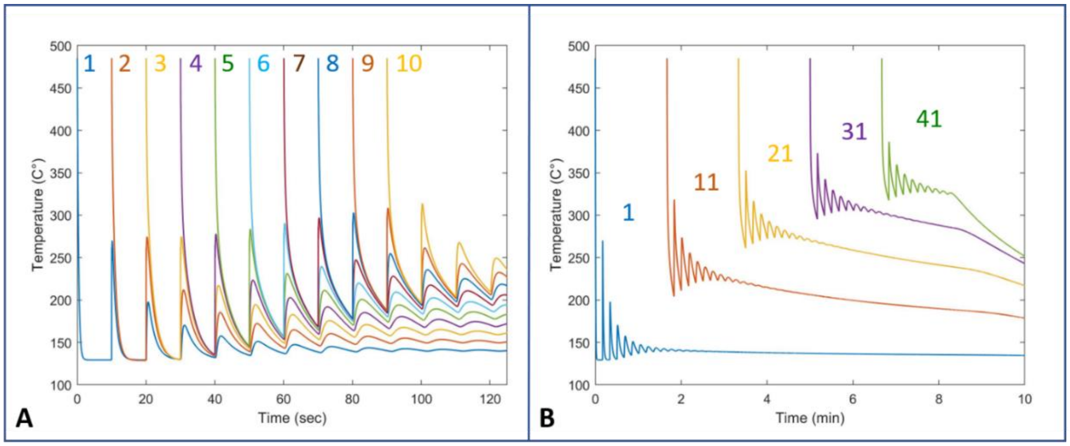

Figure 4. 6. The reheating effect of the consecutive layers can be observed from the temperature distributions of both of the first 10 layers (A), and the five layers selected from the part (B). Layer numbers are depicted next to the graphs.

For interlayer nodes, the same pattern of layer temperature distribution is observed (Fig. 4.7). It must be noted that the first part of the temperature data is extracted where these nodes act as the convection boundary condition until the consecutive layer is printed.

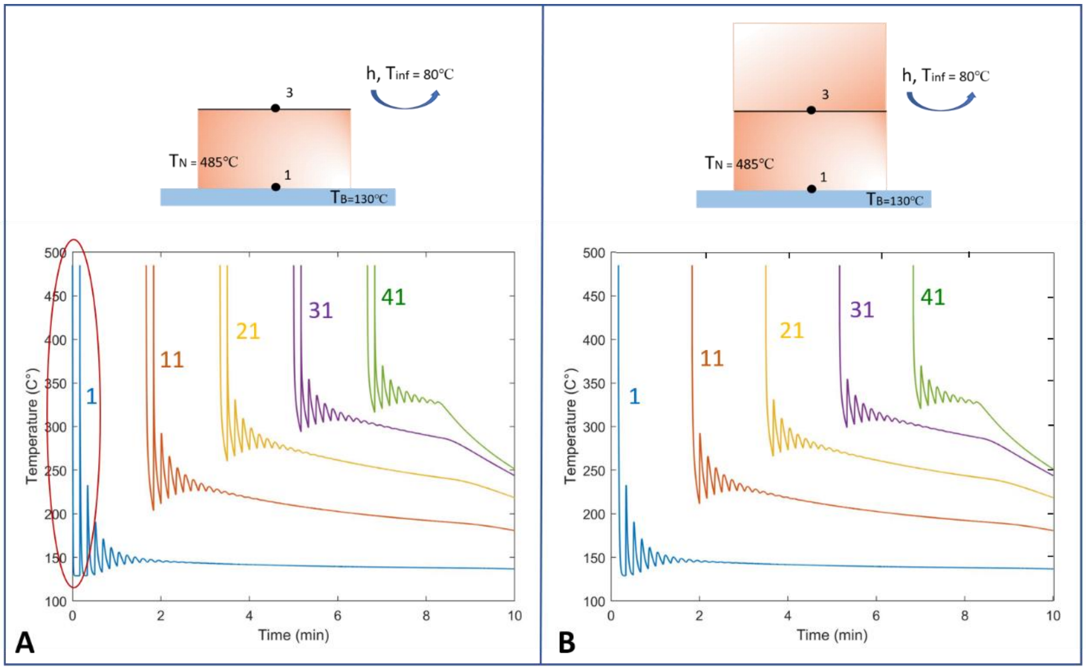

Figure 4. 7. First, an interlayer node (node 3) is a convective boundary for the lower layer (A) and then it becomes the interlayer when the next layer is laid on top (B). Interlayer numbers are depicted next to the graphs.

Apart for the model verification, the HTM results were compared to another 1D heat transfer model that is designed to predict the temperature distributions of FFF CFR-ABS thin walls with the permission of Dr. Compton [17] (Fig. 4.8). Prior to the comparison, the model was modified according to our part geometry and the PEEK material properties (the specific heat capacity (c_p), the density (ρ), and the thermal diffusivity (k)).

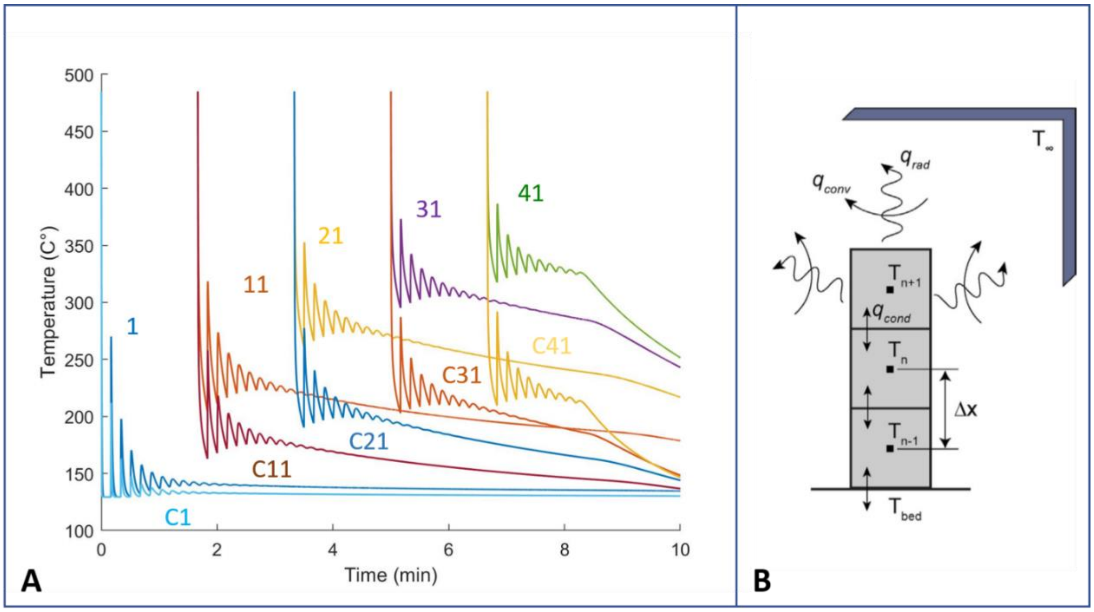

Figure 4. 8. 1D HTM developed to predict the layer and interlayer temperatures for 3D printed PEEK parts is compared with Compton et al. [17]'s 1D model (A) (numbers are depicted for the model developed in this study and 'C' is added for the reference model). Although the heat transfer will occur in one direction by the 1D model assumptions, Compton's model considered the heat transfers from side surfaces of a layer as depicted in their paper (B), reprinted from Compton et al. [17] with permission of Elsevier.

Since their node location was not necessarily aiming for an interlayer point, layer temperature distributions of five layers are compared here. The model predictions are in agreement for lower layer temperatures. However, the approximations for the upper layers diverge and the variation increases closer to the top layers.

4.4.2 Degree of Healing Model

In the literature, it is stated that the healing mechanisms are active only when the material temperature is above the melting point for the semicrystalline polymers, like PEEK [21]. Thus, to calculate the degree of healing for each interlayer point (n=49), temperature distributions between the deposition temperature (485°C) and the melting temperature of PEEK (343°C) were extracted from the HTM of PEEK (Fig. 4.9 (A)).

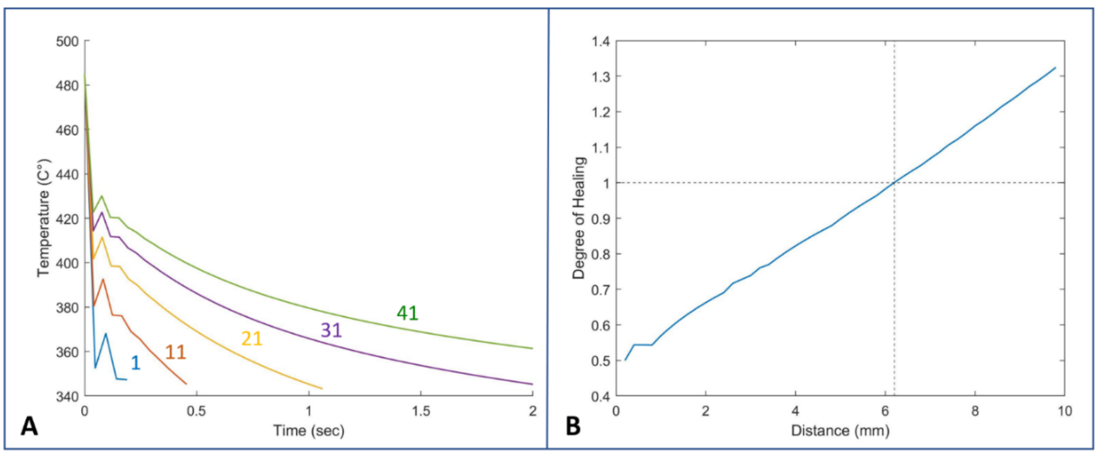

Figure 4. 9. The degree of healing for each interlayer is calculated with the help of interlayer temperature distributions between the nozzle temperature (485°C) and the melting temperature of PEEK (343°C) (A). The degree of healing across the 10 mm FFF PEEK build increases linearly from lower to upper layers in reference to the print bed, where DOH>1 indicates fully healed interfaces (B).

It is worth noting that the reheating effect might slightly contribute to healing in upper interlayers where the layer temperature is escalated above T_m. This additional healing needs to be investigated further, but it is not included in this study. Furthermore, the interlayer temperature distributions between melting and extrusion temperatures are considered to be linear for the welding function calculations. The predicted degree of healing calculated via Eq.25 and 27 is between '0.54' and '1.32' for interlayers with an average of '0.91' under initial temperature settings (Fig. 4.9 (B), Table 4.3). The degree of healing is lower than '1' for the first 30 interlayers, which means these layers are cooling down faster before 100% healing occurs. Thus, to reach 100% healing for these interlayers, more time is needed between the designated temperatures.

Table 4. 3. Theoretical degree of healing measurements of interlayers under different temperature conditions via the DOH model.

Bed Temperature (T_B, ℃)	**Nozzle Temperature (T_N, ℃)**	**Chamber Temperature (T_C, ℃)**	**Degree of Healing (DOH)**			**Interlayers with DOH<1**	**Convection Coefficient (h)**	**Time Step (Δt, sec)**
			Min	Max	Mean			
130	485	80	0.54	1.32	0.91	30	17.5	0.038
150	485	80	0.57	1.38	0.95	28	17.5	0.038
170	485	80	0.61	1.44	0.99	25	17.5	0.038
190	485	80	0.63	1.47	1.05	23	17.5	0.038
210	485	80	0.66	1.47	1.10	20	17.5	0.038
130	465	80	0.42	1.12	0.79	40	17.5	0.038
130	445	80	0.41	0.93	0.68	49	17.5	0.025
130	425	80	0.36	0.76	0.57	49	17.5	0.025
130	405	80	0.32	0.61	0.45	49	17.5	0.013
130	485	120	0.54	1.46	0.96	28	16.9	0.038
130	485	160	0.54	1.47	1.00	25	16.13	0.038
130	485	200	0.54	1.47	1.04	24	15.26	0.038

130	485	240	0.54	1.47	1.07	22	14.2	0.038

Three main temperatures' effects on the degree of healing are shown via the heat transfer-based degree of healing model (Fig. 4.10, Table 4.3). For the bed temperature (T_B), the degree of healing is calculated for five different temperatures with 20℃ increments (130, 150, 170, 190, and 210℃) (Fig 4.10 (A)). Increasing the temperature of conduction boundary condition from 130 to 210℃, referred to as print bed, increased the minimum, average and maximum healing (22%, 11%, and 21%, respectively). From minimum to maximum bed temperatures (80℃ difference) investigated in the model fully healed layer number is increased from 19 to 29 (53%).

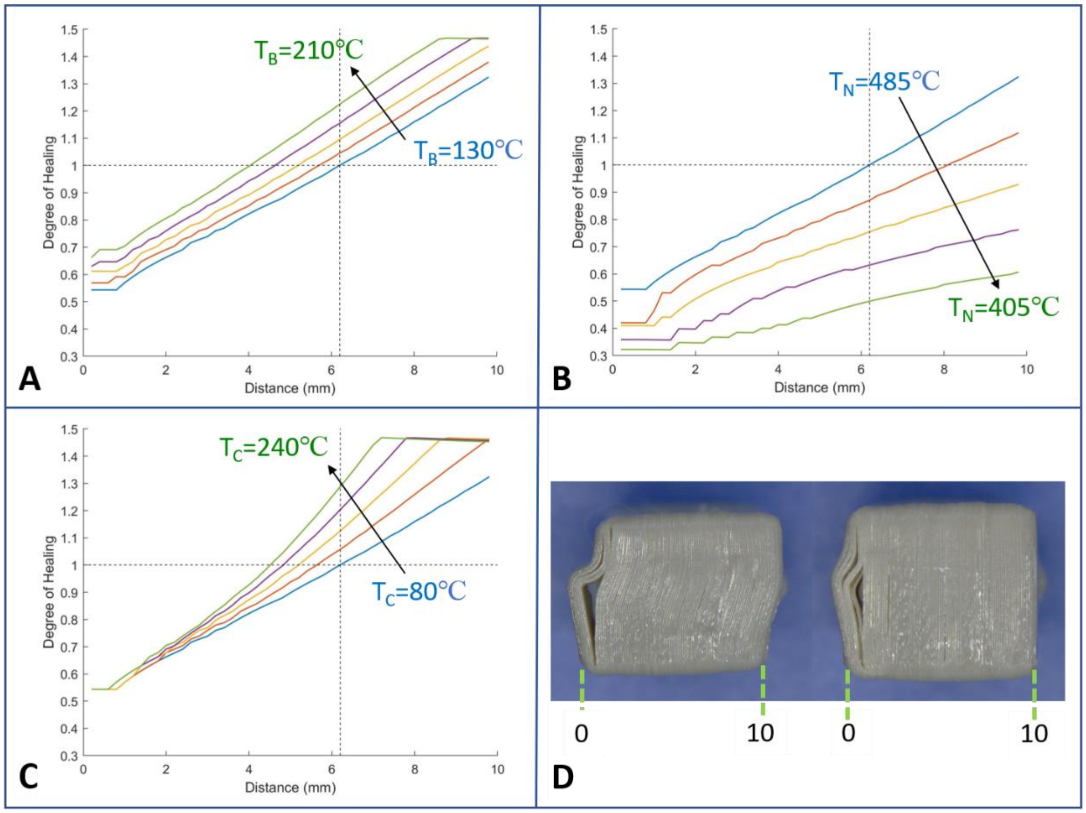

Figure 4. 10. More layers are fully healing (DOH≥1) when the main FFF temperatures, print bed (A), nozzle (B), and chamber (C), are enhanced according to the model. Layer delamination failures of previously tested FFF PEEK cages support the poorer interlayer adhesion closer to the print bed (green dotted lines are showing the distance (mm) to the print bed) (D).

Since the initial nozzle temperature (485°C) is already close to the decomposition temperature of PEEK [28], the effect of nozzle temperature on the interlayer degree of healing is studied via temperature decrements (485, 465, 445, 425, and 405°C) (Fig 4.10 (B), Table 4.3). Decreasing the nozzle temperature from 485 to 405°C decreased the minimum, average and maximum healing (41%, 51%, and 54%, respectively). With a 20°C decrease in the nozzle temperature (from 485 to 465°C), the unhealed interlayer number is increased to 40 interlayer points (33%). 445℃ and below nozzle temperature, none of the interlayers are 100% healed (n=49) with average layer healing between 45-68%. As previously mentioned, the time step (Δt) was decreased by 34% and 66% from its original value for three nozzle conditions to reach enough temperature points between the designated values. Finally, five different internal (chamber) temperatures (T_C) were investigated with 40℃ increments (80, 120, 160, 200, and 240℃) (Fig 4.10 (C), Table 4.3). Increasing the chamber temperature from 80 to 240℃ increased the average and maximum healing (18% and 11%, respectively), whereas did not change the minimum healing. From minimum to maximum chamber temperature convection coefficient varied 19%. Additionally, the 100% healed layer number increased to 27 layers (42%) with the highest chamber temperature.

4.5 Discussion

Interlayer delamination has been identified in FFF PEEK implants as a concern due to its association with the mechanical strength [8]. As heat management plays a key role in determining the bonding strength of layers to achieve stronger FFF parts, investigating the layer adhesion with a heat transfer-based polymer healing model is a valuable step in assessing their mechanical strength. In this study, we developed a 1D transient heat transfer-based, non-isothermal polymer healing model to predict the layer healing for a FFF PEEK build. The model was established in two sections separately: (1) 1D heat transfer model and (2) non-isothermal polymer healing model, which were then merged. The specific sections from temperature distributions in which healing occurs were implemented into the healing model to predict the healing across the FFF PEEK build. We observed that healing between the layers increases linearly from the bottom, where the part is in contact with the print bed, to the top of the part. According to the model, under the settings used in the previous chapter, more than half of the layers need to spend more time above T_m to heal 100%. We showed that the absolutely healed layer number could be increased by raising the main temperature settings, however, printability under these settings should be experimentally evaluated. This model helps to determine which layers are not healed properly, which could induce layer delamination under loading conditions due to insufficient healing, on the FFF PEEK builds printed with defined parameters. The results of this study support the hypothesis that heat transfer based non-isothermal polymer healing model is a suitable tool to investigate both the direct and indirect thermal parameters in a FFF system and quantify the layer healing of FFF PEEK parts.

Some limitations of this study must be noted here. For the first part of the model, considering the layer dimensions (0.2x10x10 mm^3), the heat transfer of the FFF part was modeled as 1D. This assumption was supported by the idea that most heat transfer will happen in the layer thickness direction. Additionally, due to the 1D nature of the model, layers are assumed to be deposited instantaneously after a pre-defined layer deposition time. The node numbers designated in a layer could be adjusted according to the precision of the model, but one might consider the increase in solution time and total error as a result of numerical techniques as time step decreases. For the second part of the model in which healing is calculated, the welding function was based on an equation developed experimentally in the literature for injection-molded PEEK. When using this model, the PEEK filament utilized in the study may be investigated further to govern this function experimentally for an advanced welding assumption in time. Moreover, the temperature distribution between the melting and the deposition temperatures is assumed to be linear for the simplicity in the degree of healing calculations, which could be investigated in detail in the future. Furthermore, key FFF temperatures (T_B, T_N, and T_C) used in the model are adopted from the FFF machine settings to produce spinal implants in the previous chapter. These temperatures as model inputs are experimentally validated in the next chapter. In addition, material-dependent values accessed from the literature represent the bulk PEEK properties. However, these characteristics might be affected while processing the PEEK filament from the bulk material. Especially, temperature-dependent material features should be examined for the manufactured filaments. Finally, these material dependents and thermal parameters are considered to be constant during 3D printing for the model, but more investigation is suggested under unstable FFF process conditions.

It was demonstrated via the developed model that temperatures from the upper layers remain higher for a longer period because their base (aka conduction boundary) is influenced by the previously extruded layers. The more layers below a newly deposited layer, the higher boundary temperature which preserves the heat of the deposited layer is prolonged. It is also important to recognize the reheating effect of the continuous layers. The first ten consecutive layers are decreasingly raising the temperature of the initial layer. This reheating phenomenon is also presented by previous models for FFF

[16-18]. However, due to the closer gap between the bed and extrusion temperatures, while printing low-temperature polymers, the reheating effect is less obvious and critical in layer healing compared to FFF of PEEK. Reheating the interlayer above PEEK's melting temperature might supplement to healing, which is beyond the scope of this work and needs further investigation.

For the HTM validation, the temperature distributions calculated via this model were compared with a 1D heat transfer model which was developed for CFR-ABS with Dr. Compton's permission [17]. Their model was modified with the parameters in accordance with the PEEK structure developed for the model. It is observed that predicted temperatures for the lower layers in the current model are in good agreement with Compton's model. On the other hand, our model is predicting the upper layer temperature profiles warmer than Compton's model. We anticipate the difference between the models is due to their model assumptions. Although their model is developed for 1D, the governing equations consider the heat transfer occurring from side surfaces of the object as well which incorporates the other two dimensions to the problem. This could lead the layers to cool down faster in Compton's temperature assumptions compared to our model. Finally, it was recognized that the interlayer nodes act as the convection boundaries, hence the first ten seconds of interlayer temperature distributions are excluded while calculating the degree of healing until the next layer is extruded on top. This behavior was also presented in a 3D HTM where the bonding between two different low-temperature materials is studied [18].

According to the model, we found an association between the major temperatures (T_B, T_N, and T_C) and the degree of healing in a FFF PEEK build. Zhang et al. [16] also stated that these three temperature settings are primary factors determining the temperature variation in FFF PLA parts. This is primarily driven by the welding process, for which the layers should remain above the critical temperature enough to ensure good healing. Increasing these temperatures is increasing the time spent between the extrusion temperature and the melting temperature of PEEK layers. We observed that the biggest difference in 100% healed layer number was ensured with the nozzle temperature adjustment. Decreasing the nozzle temperature by 20℃ to 465℃ almost halves totally healed layers (47% less) and below 445℃ (T_N) none of the layers could achieve 100% healing. Similarly, Coasey et al. [29] showed that the degree of filament healing increased more than two times with the same amount of increase (20℃) in the nozzle temperature for a FFF ABS interface point. They mentioned the extrusion temperature's dominant effect on the degree of healing due to its direct relation to the reptation time. In the same manner, Ko et al. [30] expressed the dramatic increase in interface strength of filaments by increasing the printing temperature for PC-ABS. They also confirmed our observation that it is reasonable to assume that the most mechanical strength is recovered during the first few seconds or even milliseconds where the layer temperature is above the critical temperature. In addition to low-temperature polymer FFF studies, Wang et al. [20] investigated the flow parameters including the nozzle temperature for FFF PEEK to optimize the surface roughness. They recommended using higher heating temperatures above 440℃ to improve density, reduce internal effects and surface roughness, and strengthen the adhesion between the printed layers and filaments in FFF PEEK builds.

Furthermore, the second dominant temperature setting in layer healing for FFF PEEK was the print bed temperature (T_B). Increasing T_B not only increased the minimum, maximum, and average degree of healing over the FFF PEEK part but also increased the totally healed layer number by 53% (T_B from 80°C to 210°C). Previously, Yin et al. [18] increased the build plate temperature (from 30°C to 68°C) for ABS-TPU and claimed that the role of the building stage is more obvious than two conditions (T_N and T_C) depending on the temperatures they tested within the model. Finally, regarding the tested conditions in this study, the chamber temperature was found to be the least dominant temperature in the degree of interlayer healing. Across the chamber temperatures tested in the model (80-240°C), the minimum degree of healing was not affected signifying that environment temperature has less impact on the lower layers of the FFF PEEK part. Yet, 42% increment in perfectly healed layers were managed with a 160°C increase in T_C since it still increased the average and maximum degree of layer healing. Contrarily, Compton et al. [17] demonstrated that the ambient temperature has the largest effect in CF-ABS layer temperature distribution according to their HTM. As discussed in limitations, it is indisputable that the temperatures selected and the material-dependent heat transfer coefficients in the studies would remarkably vary the results of the model.

Although theoretical calculations suggest the enhancement in layer healing via main temperature increments, this should be experimentally tested since efficient cooling of layers is critical which allows sequential layer accumulation to achieve a successfully 3D printed part.

Fundamentals of FFF require to detect the optimum spot where the layer temperatures should be low enough to allow further layer build, but in the meantime high enough to accomplish the maximum healing between the layers for a solid part. To produce mechanically stable FFF PEEK implants for AM-POC, it is vital to understand the heat transfer and layer healing mechanisms of FFF. This study provides a 1D heat transfer based non-isothermal degree of healing model to determine the healing of PEEK layers when 3D printed. This model proves a theoretical method to evaluate both thermal and non-thermal parameters in FFF that could be used for FFF implants to reduce the time-consuming experimental steps in the future. The associations observed between the manufacturing temperatures and the layer healing highlight the potential of the model in parameter optimization for different designs of FFF PEEK implants.

4.6 References

1. Tack, P., et al., *3D-printing techniques in a medical setting: a systematic literature review.* Biomed Eng Online, 2016. **15**(1): p. 115.
2. Eltorai, A.E., E. Nguyen, and A.H. Daniels, *Three-Dimensional Printing in Orthopedic Surgery.* Orthopedics, 2015. **38**(11): p. 684-7.
3. Gibbs, D.M., et al., *Hope versus hype: what can additive manufacturing realistically offer trauma and orthopedic surgery?* Regen Med, 2014. **9**(4): p. 535-49.
4. Martelli, N., et al., *Advantages and disadvantages of 3-dimensional printing in surgery: A systematic review.* Surgery, 2016. **159**(6): p. 1485-1500.
5. Provaggi, E., J.J.H. Leong, and D.M. Kalaskar, *Applications of 3D printing in the management of severe spinal conditions.* Proc Inst Mech Eng H, 2017. **231**(6): p. 471-486.
6. Ventola, C.L., *Medical Applications for 3D Printing: Current and Projected Uses.* P t, 2014. **39**(10): p. 704-11.
7. Basgul, C., et al., *Thermal localization improves the interlayer adhesion and structural integrity of 3D printed PEEK lumbar spinal cages.* Materialia, 2020. **10**: p. 100650.
8. Basgul, C., et al., *Structure-property relationships for 3D printed PEEK intervertebral lumbar cages produced using fused filament fabrication.* J Mater Res, 2018. **33**(14): p. 2040-2051.
9. Basgul, C., et al., *Does annealing improve the interlayer adhesion and structural integrity of FFF 3D printed PEEK lumbar spinal cages?* Journal of the Mechanical Behavior of Biomedical Materials, 2020. **102**: p. 103455.
10. Delaney, L.J., et al., *Acoustic Parameters for Optimal Ultrasound-Triggered Release from Novel Spinal Hardware Devices.* Ultrasound in Medicine & Biology, 2020. **46**(2): p. 350-358.
11. Delaney, L.J., et al., *Ultrasound-triggered antibiotic release from PEEK clips to prevent spinal fusion infection: Initial evaluations.* Acta Biomaterialia, 2019. **93**: p. 12-24.
12. Cheng, B.C., et al., *A comparative study of three biomaterials in an ovine bone defect model.* Spine J, 2020. **20**(3): p. 457-464.

13. Costa, S.F., F.M. Duarte, and J.A. Covas, *Estimation of filament temperature and adhesion development in fused deposition techniques.* Journal of Materials Processing Technology, 2017. **245**: p. 167-179.

14. Thomas, J. and J. Rodriguez, *Modeling the fracture strength between fused-deposition extruded roads.* Proc. Solid Freeform Fabr. Symp, 2000: p. 16-23.

15. Bellehumeur, C., et al., *Modeling of Bond Formation Between Polymer Filaments in the Fused Deposition Modeling Process.* Journal of Manufacturing Processes, 2004. **6**(2): p. 170-178.

16. Zhang, J., et al., *Numerical investigation of the influence of process conditions on the temperature variation in fused deposition modeling.* Materials & Design, 2017. **130**: p. 59-68.

17. Compton, B.G., et al., *Thermal analysis of additive manufacturing of large-scale thermoplastic polymer composites.* Additive Manufacturing, 2017. **17**: p. 77-86.

18. Yin, J., et al., *Interfacial bonding during multi-material fused deposition modeling (FDM) process due to inter-molecular diffusion.* Materials & Design, 2018. **150**: p. 104-112.

19. Ravoori, D., et al., *Experimental and theoretical investigation of heat transfer in platform bed during polymer extrusion based additive manufacturing.* Polymer Testing, 2019. **73**: p. 439-446.

20. Wang, P., B. Zou, and S. Ding, *Modeling of surface roughness based on heat transfer considering diffusion among deposition filaments for FDM 3D printing heat-resistant resin.* Applied Thermal Engineering, 2019. **161**: p. 114064.

21. Yang, F. and R. Pitchumani, *Healing of Thermoplastic Polymers at an Interface under Nonisothermal Conditions.* Macromolecules, 2002. **35**(8): p. 3213-3224.

22. Yener, Y.K., S., *Heat Conduction*. Vol. 4th Edition. 2008: CRC Press.

23. *Victrex™ PEEK 450G™*. 2019.

24. Cheng, S.Z.D. and B. Wunderlich, *Heat capacities and entropies of liquid, high-melting-point polymers containing phenylene groups (PEEK, PC, and PET).* Journal of Polymer Science Part B: Polymer Physics, 1986. **24**(8): p. 1755-1765.

25. Churchill, S.W. and H.H.S. Chu, *Correlating equations for laminar and turbulent free convection from a vertical plate.* International Journal of Heat and Mass Transfer, 1975. **18**(11): p. 1323-1329.

26. Yang, F. and R. Pitchumani, *Nonisothermal healing and interlaminar bond strength evolution during thermoplastic matrix composites processing.* Polymer Composites, 2003. **24**(2): p. 263-278.

27. Lee, W.I. and G.S. Springer, *A Model of the Manufacturing Process of Thermoplastic Matrix Composites.* Journal of Composite Materials, 1987. **21**(11): p. 1017-1055.

28. Patel, P., et al., *Mechanism of thermal decomposition of poly(ether ether ketone) (PEEK) from a review of decomposition studies.* Polymer Degradation and Stability - POLYM DEGRAD STABIL, 2010. **95**: p. 709-718.

29. Coasey, K., et al., *Nonisothermal welding in fused filament fabrication.* Additive Manufacturing, 2020. **33**: p. 101140.

30. Ko, Y.S., et al., *Improving the filament weld-strength of fused filament fabrication products through improved interdiffusion.* Additive Manufacturing, 2019. **29**: p. 100815.

Chapter 5: Validation of the theoretical layer temperatures determined via heat transfer model with the experimental FFF PEEK layer temperatures

5.1 Abstract

FFF PEEK implants' failure mechanism was indicated as layer delamination in the literature [1]. Evaluating the heat transfer mechanisms of FFF PEEK is critical to understand the failure mechanism of 3D printed implants. In this study, the heat transfer component of the previously developed model for layer healing assessment of FFF PEEK was validated separately. The initial PEEK cube design (10x10x10 mm^3), used for model development, was 3D printed in industrial (P220) and medical (M220) generations FFF machines. The cubes were printed under 2000 mm/min speed with a 0.4 mm nozzle diameter and an industrial-grade PEEK filament (Apium). During the printing and cooling processes of FFF, thermal videos were recorded via an infrared (IR) camera in both printers while printing the PEEK cube. Thermal images were then processed to obtain layer temperature distributions and cooling profiles of FFF PEEK prints. Additionally, experimental print bed (T_B) and chamber (T_C) temperatures were calculated from the thermal images to employ the HTM prior to validation. Since the nozzle temperature (T_N) was defined as the maximum material temperature in the model, experimental nozzle temperature was calculated from the maximum layer temperatures measured. We observed that the model predictions were in good agreement with the experimental data particularly for mid-layers (24-26th layers) of FFF PEEK cubes printed in the P220 machine. Moreover, the layer temperature estimations for M220 prints reached the experimental data in earlier layers (~20th layer)

due to the raft effect. In the first quarter of the print period (the first two minutes), model approximations were converged to the experimental temperatures beginning at the 20^{th} layers in both machines and was aligned with the upper layer temperatures to the top. This chapter presents a validation technique for heat transfer models on determining the layer temperatures of FFF PEEK builds that will enable the further development of the model as well as its implementation to the healing model to improve the macro mechanical properties of FFF PEEK implants.

5.2 Introduction

FFF systems as an AM method has inspired both research and industry to manufacture PEEK implants [2-5]. FFF has the material conservation advantage by requiring filament as the form of material over SLS powder systems that have been investigated to manufacture PEEK implants [6-8]. In addition to savings over expensive medical grade PEEK material, the FFF technology itself is more accessible which promotes research towards AM-POC. Although, there have been some initiatives on FFF PEEK implants [5, 9, 10], due to high processing temperatures of PEEK it is important to avoid layer delamination by ensuring proper healing between the PEEK layers [1]. In the previous chapter, the importance of understanding the heat transfer mechanisms for further improvements in FFF PEEK implants was emphasized. The HTM developed to predict layer temperatures of a FFF PEEK build was investigated theoretically in detail. As the first step, it is crucial to validate the presented heat transfer model for further implementation of the HTM into the layer healing model to investigate the macro-mechanical properties of FFF PEEK implants.

In the literature, researchers utilized heat transfer models to investigate the mechanical outcomes of FFF builds [11-14]. For instance, Thomas et al. [11] measured the fracture toughness mechanically in FFF ABS, where they studied a 2D heat transfer model. Moreover, Bellehumeur et al. [12] used sintering experiments for quantitative predictions of FFF ABS filament bond formation in which they employed a 1D heat transfer model. Similarly, the bonding strength, calculated theoretically with the help of a 3D heat transfer model, was validated by mechanical tests in bi-material FFF prints

(ABS-TPU) [13]. Finally, one study investigated the surface roughness of FFF PEEK implementing a 1D heat transfer model and measured the roughness of 3D printed PEEK parts experimentally [14]. Nonetheless, a few studies which were developed for low-temperature polymer FFF directly investigated the validation of their heat transfer models [15-17]. Costa et al. [15] compared the filament temperatures of ABS obtained via the 1D heat transfer model with the experimental filament temperatures measured via an IR camera. Besides, Ravoori et al. [17] used an IR camera to measure the temperatures of the PLA filaments extruded to investigate the temperature field on the platform bed during filament dispense. Finally, one study conducted thermal camera readings to justify the layer temperatures of large scale CF-ABS builds predicted with a 1D HTM [16].

Heat transfer models have been recognized for temperature analysis in FFF systems to optimize the mechanical strength of FFF builds. However, most of the studies which utilized HTMs directly verified the model outcomes via mechanical tests bypassing the heat transfer model validation. Although there have been efforts to validate the temperatures from thermal videos/images in few studies, they all investigated the low-temperature polymers in which the whole healing mechanisms were different compared to FFF PEEK layers. In addition, two studies out of these investigated the filament temperatures rather than examining the layer temperatures. Besides, the other study inspected the layer temperatures for massive FFF build failures such as warping and cracking, which resulted in large-scale model geometry that is out of scope for implants. Hence, specific validation of FFF PEEK layer temperature predictions is critical for the proposed heat transfer model before its further applications in layer healing approximations.

In this study, we used thermal camera readings collected from two different FFF PEEK printers to validate the 1D heat transfer model that is developed to predict the temperature distributions of FFF PEEK layers via simulating the FFF process. Hence, we asked: (1) Can previously exhibited 1D HTM estimate the FFF PEEK layer temperatures through the FFF build? (2) Will the HTM tolerate a different FFF system with additional heat transfer mechanisms? (3) How are the model predictions affected by initial geometry change with a raft addition?

5.3 Materials & Methods

5.3.1 Experimental Setup for Temperature Measurements

To validate the layer temperatures obtained by the HTM in the previous chapter, the initial cube design (10x10x10 mm^3) was printed with industrial-grade PEEK filament (Apium PEEK 4000) both in 2^{nd} (P220) and 3^{rd} generation (M220) FFF machines (Apium Additive Technologies GmbH, Karlsruhe, Germany) (Fig. 5.1).

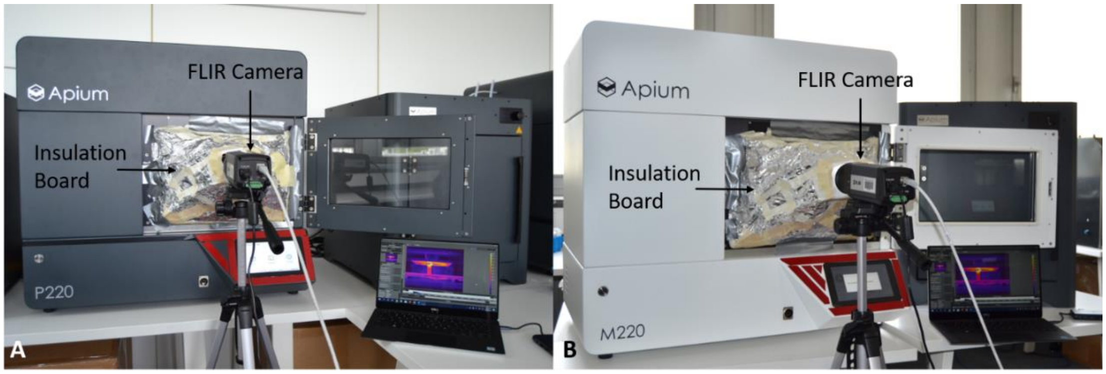

Figure 5. 1. Thermal videos were recorded for both P220 (A) and M220 (B) FFF printers During PEEK cube prints.

The filaments used in this study were dried at 120°C for four hours prior to printing. In the P220 machine, which was introduced as the industrial 3D printer for high-performance materials, heating elements are the extruder, glass print bed, and the metal heated plate (referred to as the zone heater) around the extruder (nozzle) (maximum temperatures of 540°C, 160°C, and 250°C, respectively). On the other hand, M220 is the first 3D printer that is invented for medical PEEK products and implants by ensuring a sterile print environment. Thus, the prints are deposited on a specifically designed metal print bed, which allows filtered hot airflow in a particle-free circuit (maximum temperature of 280°C). The STL file of the cube was created using commercially available software (SolidWorks 2016). Simplify 3D software (available commercially) was used to construct the g-codes from the STL file for both FFF machines. To increase the adhesion between the cube and the print bed in the P220 machine, in addition to the brim (Fig. 5.2 (B-D)), one layer of Dimafix® (DIMA 3D

Printers) solution was applied onto the heated bed prior to printing. For the M220 machine, the slicing software of Apium embedded in the printer creates an automated raft for every part (Fig. 5.2 (E)). To avoid contamination, the combination of the raft and print bed design in this machine extinguishes the requirement for any additional adhesives.

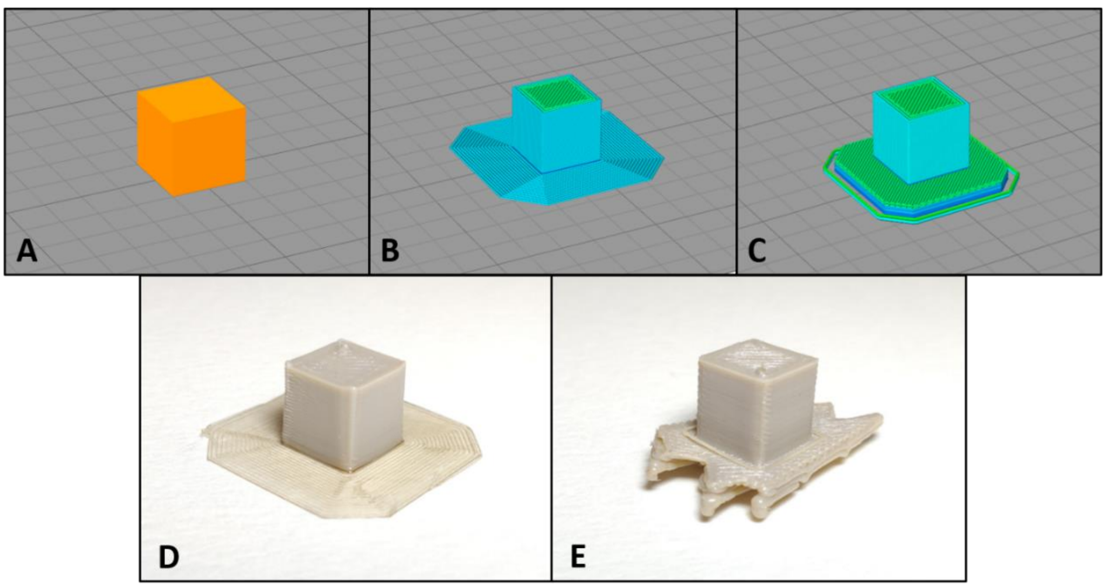

Figure 5. 2. The cube design (A), used in the previous chapter, was printed with the addition of brim (B-D) or raft (C-E) depending on the FFF system requirements.

FFF PEEK cubes were printed under 2000 mm/min print speed with a 0.4 mm nozzle diameter and 0.2 mm layer thickness in both machines (as studied in the previous chapter) (Table 5.1).

Table 5. 1. FFF parameters used in this study for 2nd and 3rd generation PEEK printers.

	2nd Generation Printer (P220)	3rd Generation Printer (M220)
Extruder		
Nozzle Diameter	0.4	0.4
Extrusion Multiplier	0.90	0.90
Extrusion Width	0.48	0.48
Ooze Control (Retraction Enabled)		
Retraction Distance (mm)	2	2
Retraction Speed (mm/min)	1800	1800
Retraction Vertical Lift	0.15	0.15
Layer Settings		
Layer Height (mm)	0.2	0.2
Top Solid Layers	3	3
Bottom Solid Layers	3	3
Outline/Perimeter Shells	3	3
First Layer Setting		
1st Layer Height	100% Height	100% Height
1st Layer Width	100% Width	100% Width
1st Layer Speed	40%	40%
Additions (Skirt/Brim)		
Use Skirt/Brim	Enabled	Enabled
Skirt Layers	1	2
Skirt Offset from Part (mm)	0.00	1.00
Skirt Outlines	18	1
Use Raft	Disabled	Enabled
Raft Base Layers	-	3
Raft Base Layer Height (mm)	-	0.7 0.6 0.5
Raft Base Layer Speed (mm/min)	-	200
Raft Interface Layers (mm)	-	3
Raft Interface Layer Height (mm)	-	0.2
Raft Interface Layer Speed (mm/min)	-	2000
Raft Interface Infill	-	100%
Raft Offset from Part (mm)	-	-0.1
Infill Settings		
Internal Fill Pattern	Rectilinear	Rectilinear
External Fill Pattern	Rectilinear	Rectilinear
Interior Fill Percentage	100%	100%
Outline Overlap	50%	50%
Infill Extrusion Width	100%	90%

Minimum Infill Length (mm)	5	5
Temperature Settings		
Bed Temperature (°C)	130	180 (Air Flow)
Nozzle Temperature(°C)	440	440
Speed Settings		
Default Printing Speed (mm/min)	2000	2000
Outline Underspeed	40%	40%
Solid Infill Underspeed	80%	80%
X/Y Axis Movement Speed (mm/min)	4800	4800
Z Axis Movement Speed (mm/min)	1000	1000
Other		
Build Volume (mm^3)	205x155x150	130x130x130
Filament Diameter (mm)	1.75	1.75

When printing the PEEK cubes with defined settings in both FFF printers, thermal videos are recorded at 50 Hz (frames per second) with a FLIR A655sc machine (FLIR, Wilsonville, OR). The accuracy of the camera is ±2℃ that is established by yearly calibrations from the manufacturer. As suggested by the manufacturer, the camera was positioned approximately 25 cm away from the heat source (the print area). Since the temperature readings were affected by an object placed between the print build and the camera (i.e., the 3D printer door), an insulation board in both machines surrounded the IR camera to preserve the heat while the printer door remained open (Fig. 5.1).

5.3.2 Image Analysis

Thermal videos collected with a FLIR A655sc camera were converted into the TIFF image stacks which contain the temperature information via ResearchIR software (FLIR, Wilsonville, OR) for further analysis in MATLAB 2018b. Second, the region of interests (ROI) was defined conforming to the object location, and the image stacks were cropped accordingly to 150 by 150-pixel frames (Fig.5.3).

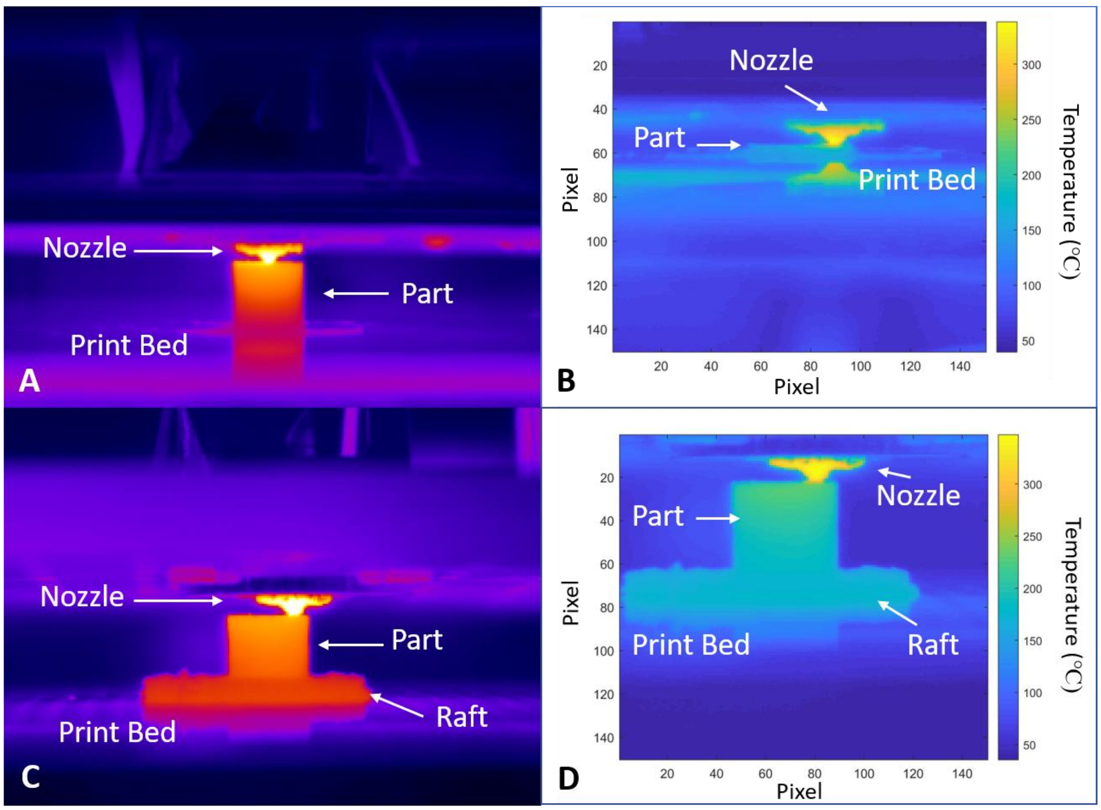

Figure 5. 3. To further analyze the thermal readings from both P220 (A-B) and M220 (C-D) machines, first, the videos (A-C) were transferred to MATLAB 2018b as thermal image stacks, and then these images were cropped according to ROIs defined (B-D).

Once the processable image stacks with ROIs were achieved in MATLAB 2018b, “Sobel Edge Detection Algorithm” [18] was conducted to detect the edges defined near the printed cubes for both machines (Fig. 5.4). According to the movement of these edges during the FFF processes, the beginning and end frames, in between where the cubes were being printed, were determined for the layer temperature history.

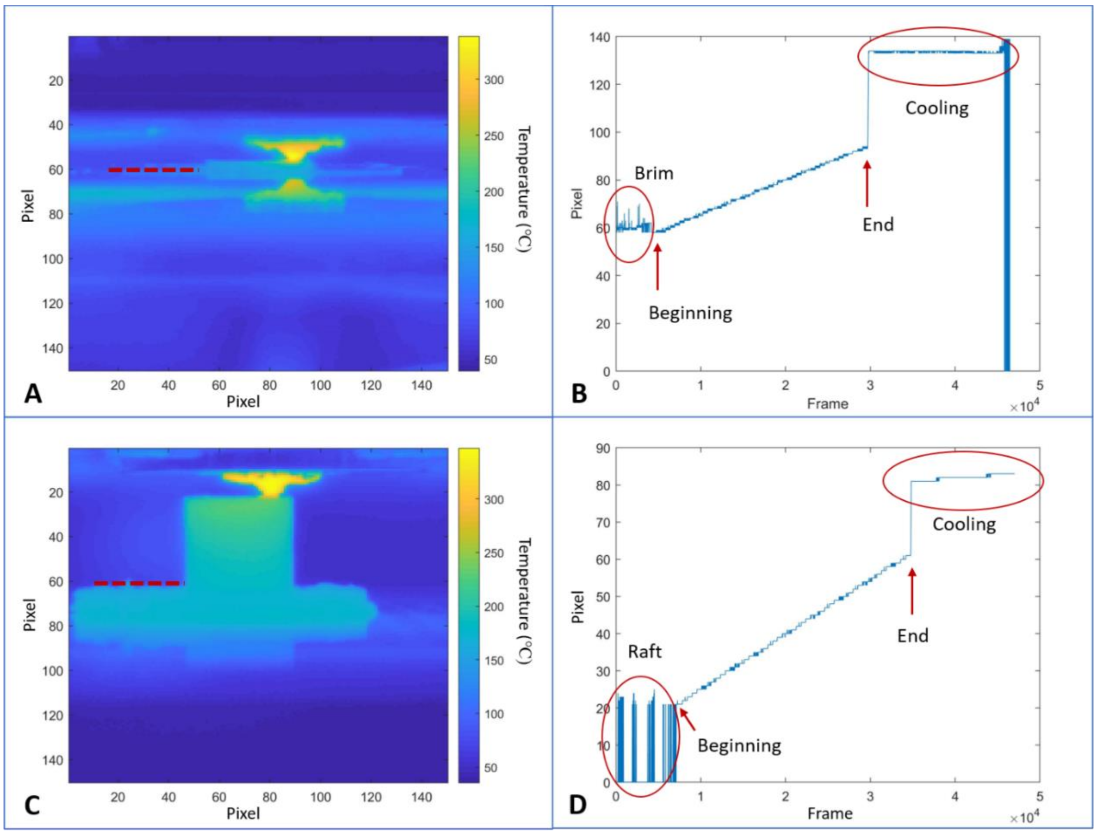

Figure 5. 4. The edges were defined near the FFF PEEK cubes to track the print bed movement in both P220 (A-B) and M220 (C-D) machine thermal images. According to the edge movement, FFF processes were divided into sections. In both processes, where solely the cubes were 3D printed (between beginning and end frames) were determined to collect the layer temperatures during printing (B-D).

After defining the beginning and end frames where the part is being printed, the mid-pixel of the object is selected to analyze the temperatures in both printers (Fig. 5.5). Due to the set-up limitations of the IR camera, pixel number through the printed cube was interpolated to acquire an exact equivalent of the pixel numbers and the layer numbers (n=50).

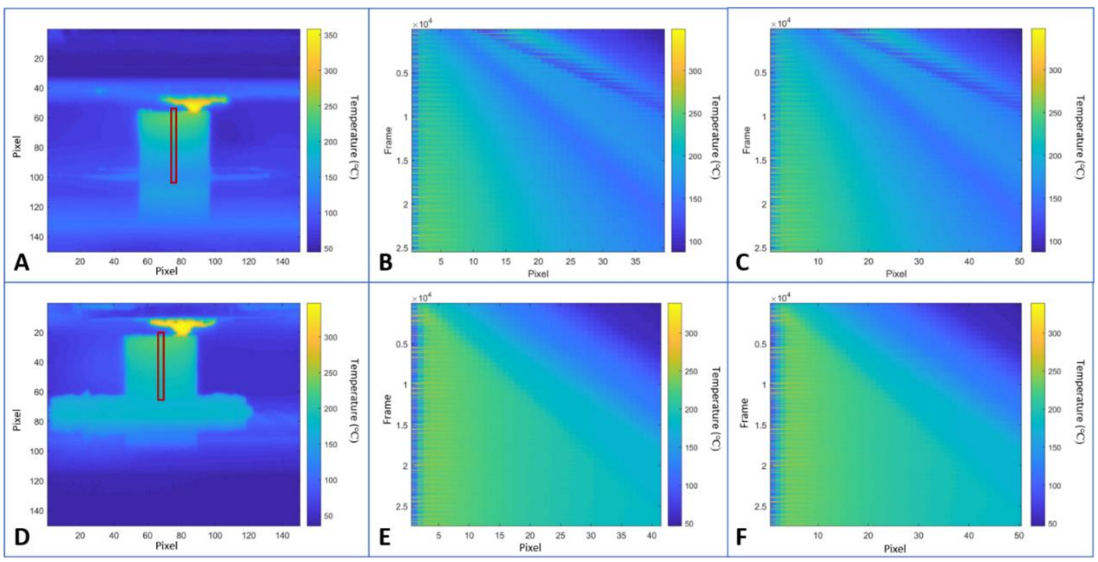

Figure 5. 5. For temperature history analysis of layers, mid-points of the cubes were selected in P220 (A) and M220 (D) prints. Bilinear interpolation of the pixel numbers, which correspond to the cubes (n=39 for P220 (B) & n=40 for M220 prints (E)), was employed in thermal images to achieve equal pixel numbers to the layers (n=50) (C-F).

After the data interpolation, there were enough pixels to maintain the temperature history of each layer. However, the pixel which contains the temperatures of a specific layer was changing because of the sequential deposition of the layers during printing.

In a certain pixel, a layer temperature was preserved for ten seconds until the next layer was deposited. After ten seconds, the same layer's temperature was maintained for the next ten seconds in the below pixel due to print bed movement in the negative z-direction (Fig. 5.6).

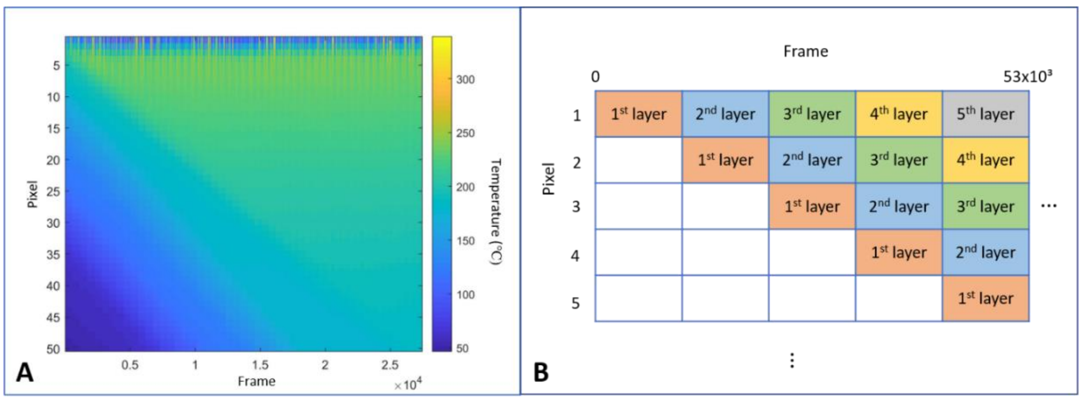

Figure 5. 6. In both FFF processes studied in this chapter, the print bed moves down after each layer deposition. Thus, it was essential to unwrap the interpolated temperature data first (A). For instance, the 1st layer's temperature was stored in the 1st pixel until the 2nd layer deposited on top, hence the pixel number corresponding to a layer was updated continuously after every ten seconds for each layer (B).

Once the cubes were printed completely, the print bed in both FFF machines moved down from the nozzle and the object was allowed to cool down at that certain location (Fig. 5.7). The pixel numbers as a result of the new location were revisited to assess the temperature distribution during the cooling.

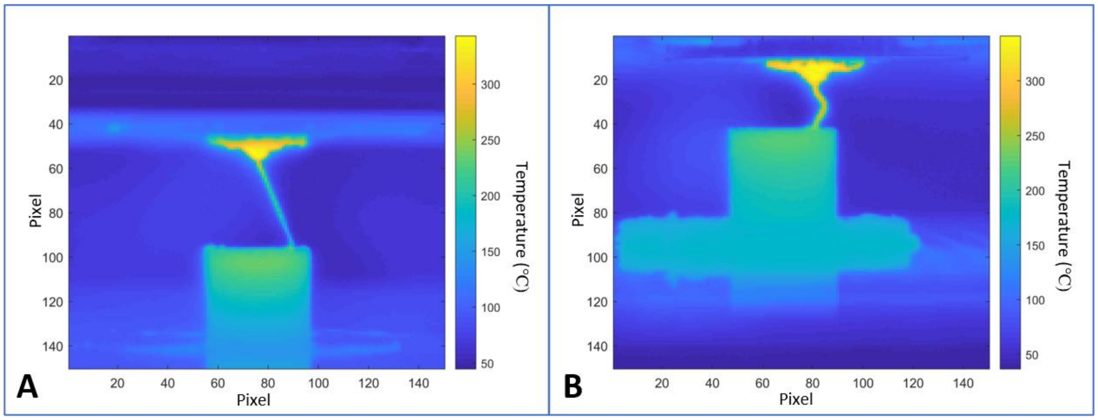

Figure 5. 7. Once 3D printing of the cubes was completed, the cubes were relocated in the thermal images. Since the cube was stable during cooling for both P220 (A) and M220 (B) machines contrary to their instability during printing, the temperature history of each layer was stored in a certain pixel number.

In addition, key FFF temperatures (T_N, T_B, and T_C) utilized in the model were calculated experimentally for model validation in both printers. For the material deposition temperature (referred to as the nozzle temperature), the maximum temperatures from each layer (n=50) were averaged in MATLAB 2018b. For the bed and environment temperatures, the mean value was calculated from five different regions selected in the thermal videos with the help of ImageJ (U. S. National Institutes of Health, MD, USA). I developed custom scripts using MATLAB 2018b to fulfill previously described steps for layer temperature history of FFF PEEK cubes printed with 2nd (P220) and 3rd (M220) generation machines (Appendix C).

5.4 Results

5.4.1 P220 machine

The material deposition temperature to employ in the model for the P220 machine was 344℃ (Table 5.2). The bed and chamber temperatures calculated from the thermal videos were 95℃ and 213℃, respectively (Fig.5.8).

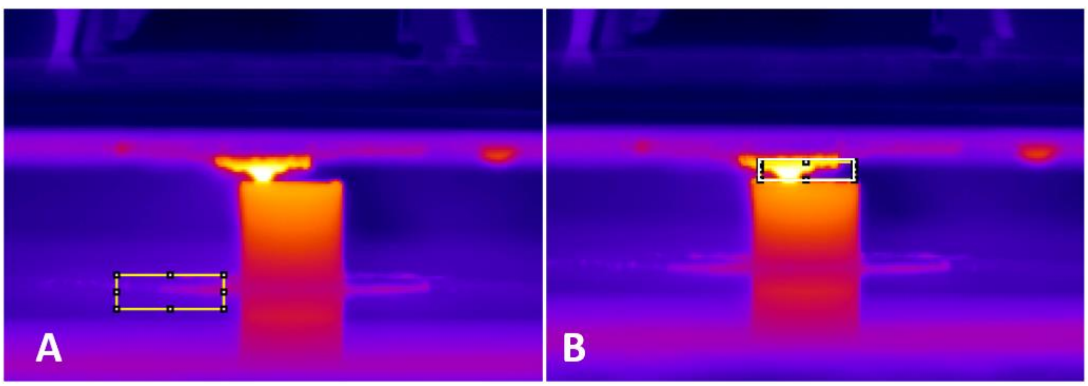

Figure 5. 8. The print bed temperature was calculated from the regions selected around the object while avoiding the reflected areas (A). For the chamber temperature measurements, the top of the cube was selected to simulate developed HTM's 1D consideration optimally (B).

The natural convection coefficient (h) and the time step (Δt) were revised in the HTM with the new temperature implementation (Table 5.2).

Table 5. 2. Parameters used in model validation for P220 printer.

Parameters	**Value**
Thermal conductivity, k (W/m,K)	0.29
Specific heat capacity, cp (J/kg.K)	1957
Density, ρ (kg/m³)	1300
Natural convection coefficient, h (W/m². K)	14.9
Part length, L (m)	0.01
Number of layers	50
Layer height, d (m)	0.0002
Distance between the nodes, Δx (m)	0.0001
Number of nodes, n	101
Layer deposition time, t (sec)	10
Time step, Δt (sec)	0.033
Cool down time (sec)	300
Initial Temperature, T_N (°C)	344
Bed Temperature, T_B (°C)	95
Chamber Temperature, T_C (°C)	213

It was observed that there was more noise due to the extruder in the beginning of the print, especially the first minute, where the heat of the nozzle affected the layer temperature readings the most (Fig.5.9 (A)). While that effect of the nozzle diminished slowly, the reheating effect of the sequential layers was more visible. For cooling temperatures, a parabolic decay at the pre-defined cooling period was observed as expected (Fig.5.9 (B)). It should be noted that the temperature data during the instant movement of the object from the printing to the cooling stage was excluded here.

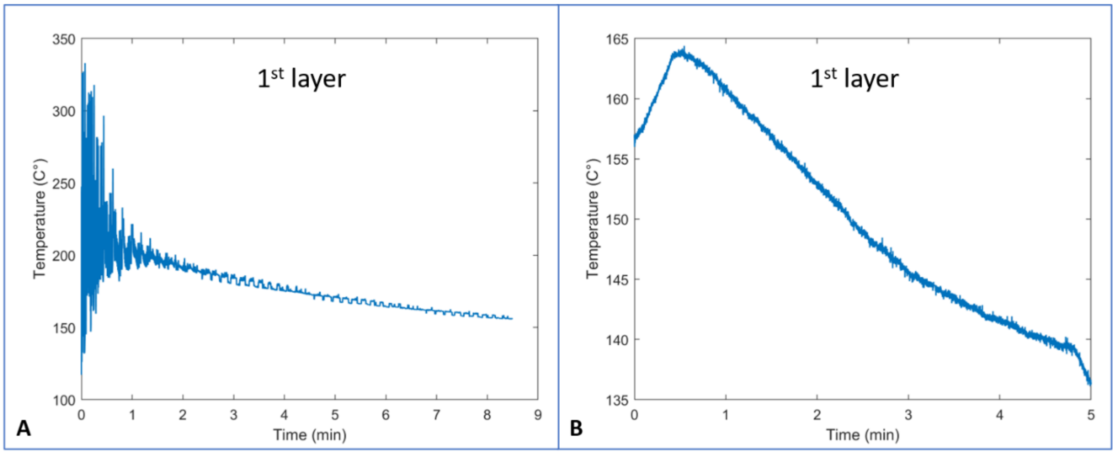

Figure 5. 9. For each layer, the experimental temperature distributions for printing (A) and cooling (B) stages of the FFF process were plotted and the graphs were merged for further validation.

As mentioned in the previous chapter, the temperatures stayed higher for longer periods from the bottom to the top of the FFF PEEK cube printed. This was shown in five-layer picks through the print build (Fig. 5.10). We noticed from the FFF experiments that the 1st layer temperature dropped from 333℃ to 195℃ approximately in the first two minutes and slowly decreased to 156℃ by the end of the print. Whereas the maximum temperature observed for the 11th layer was 343℃ which decreased to 217℃ in two minutes and was 173℃ at the print end. The maximum layer temperature, the temperature at two minutes and before cooling started were 344℃, 229℃, and 193℃, respectively for the 21st layer. The maximum temperature started at 346℃ and then reduced to 235℃ after 120 seconds for the 31st layer. The temperature measured before cooling started was 217℃. Finally, for the last layer selected (41st layer), the highest layer temperature was 347℃. After two minutes, the layer was already in the cooling stage and the temperature was 217℃. Before cooling started, the last temperature measured was 241℃.

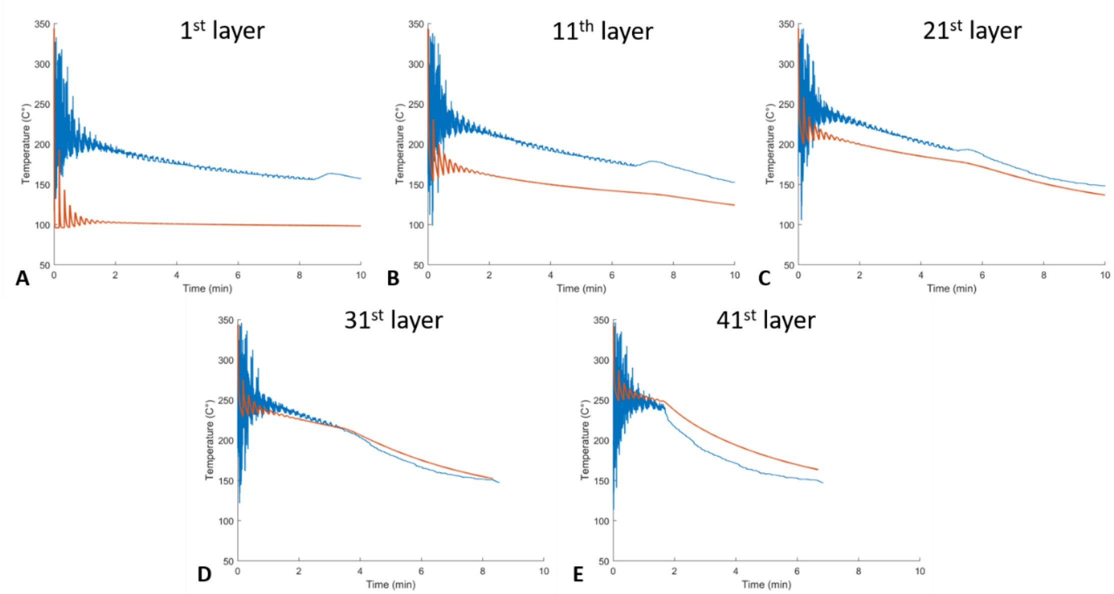

Figure 5. 10. Temperature distributions achieved from the model (red) vs experimental (blue) data were analyzed for layers of FFF PEEK cube printed in the P220 machine. As for the lower layers, conduction boundary (print bed temperature) was dominant in the model (A-B), mid-layer temperature predictions of the model, and experiments were in good agreement (C-D). For upper layers, experimental layer temperatures were marginally lower than the model approximations (E).

The temperature decrement observed while cooling was steeper for the upper layers. When we compared the layer temperature distributions from the 1D HTM model designed for FFF PEEK and the experimental data recorded from the P220 machine, we recognized that the model assumptions were closer to the experimental data for the mid-layers of the cube (Fig. 5.11). The model approximated the lower layer temperatures colder compared to the experimental temperatures. However, the difference between the model and experimental temperature history was diminishing when approaching the upper layers through the FFF build. Moreover, the model predictions for the top layers stayed slightly higher than the experimental temperatures.

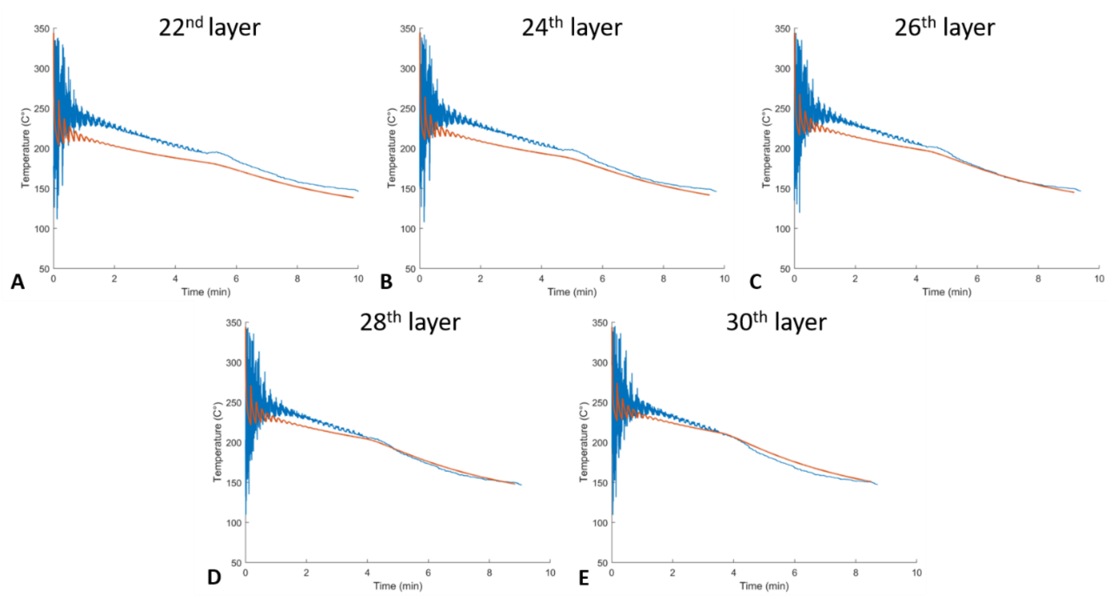

Figure 5. 11. The printing profile of the model approximations (red) was approaching the experimental temperatures (blue) for five-layer picks from the mid-part of the FFF PEEK cube (A through E). The model cooling profile fitted the experimental temperature profile by the mid-layer (C) and then moved above the experimental predictions imperceptibly (D-E).

In addition to whole printing and cooling processes, HTM approximations of physical layer temperatures are especially important for the first couple minutes where healing occurs as mentioned in the previous chapter (Fig.5.12). Although the noise of experimental data was more notable when studying temperature profiles in shorter time sections, the model approximations along with the layer reheating effect were in good agreement with layer temperatures as the top of the cube was reached.

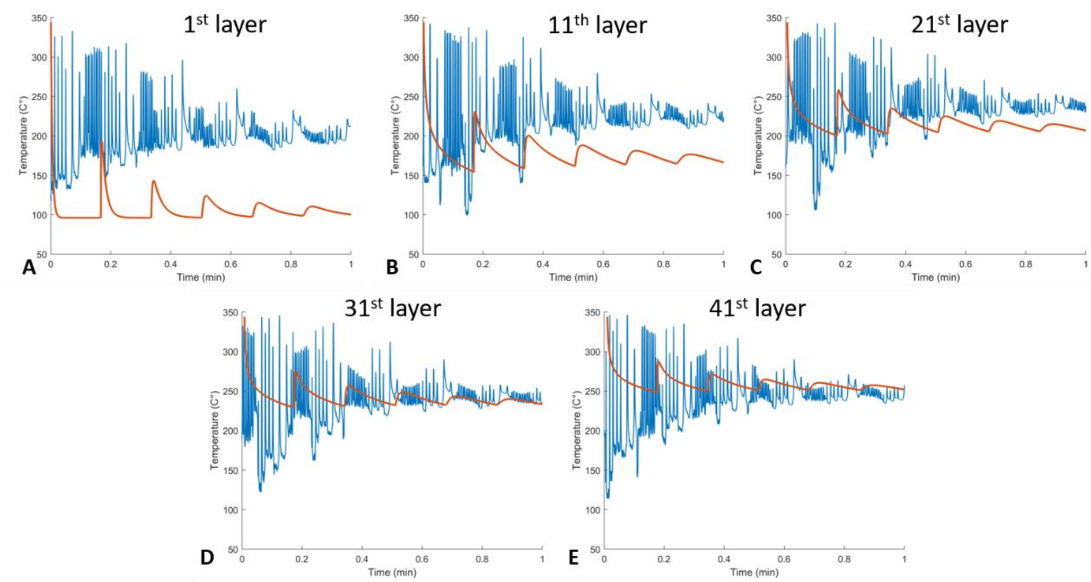

Figure 5. 12. The model predictions of layer temperatures (red) through the FFF PEEK cube were also considered under one minute. Model approximations of the layer temperatures under one minute improved when converging to the top layers (A through E).

5.4.2 M220 machine

In the M220 printer, the material deposition temperature was measured as 318℃ considering the maximum layer temperatures (Table 5.3). As the designed HTM examined the conduction boundary (print bed) at a constant temperature, the bed and chamber temperatures were calculated similarly for this machine as 91℃ and 215℃, respectively (Fig. 5.13).

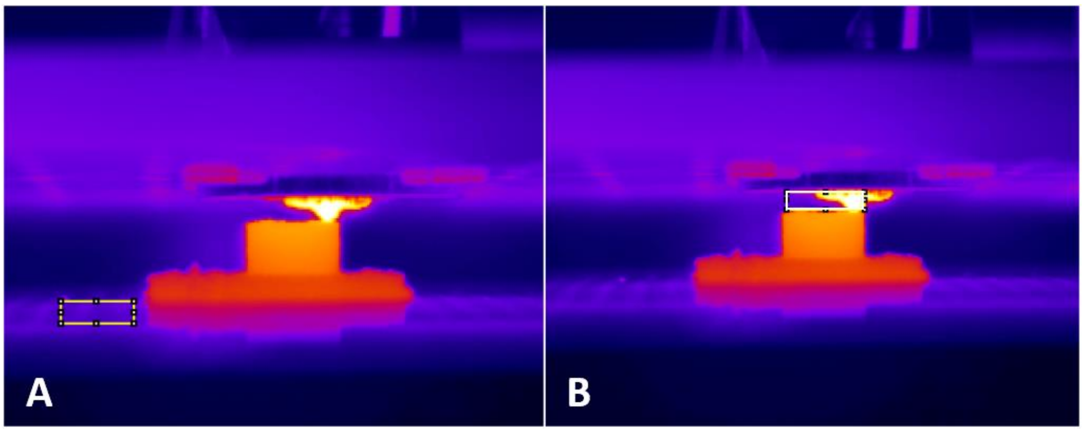

Figure 5. 13. The print bed temperature was measured around the FFF PEEK cube by preventing the raft and the reflected areas (A). The chamber temperature measurements were conducted on the top of the cube due to the 1D consideration of the HTM (B).

Since the raft, printed automatically underneath the FFF cube, changed the length of the part in the HTM, the number of layers, and nodes were modified accordingly for further validation (Table 5.3).

Table 5. 3. Parameters conducted in the HTM for the FFF PEEK cube printed in the M220 machine.

Parameters	**Value**

Thermal conductivity, k (W/m,K)	0.29
Specific heat capacity, cp (J/kg.K)	1957
Density, ρ (kg/m³)	1300
Natural convection coefficient, h (W/m².K)	14.9
Part length, L (m)	0.012
Number of layers	62
Layer height, d (m)	0.0002
Distance between the nodes, Δx (m)	0.0001
Number of nodes, n	125
Layer deposition time, t (sec)	10
Time step, Δt (sec)	0.033
Cool down time (sec)	300
Initial Temperature, T_N (°C)	318
Bed Temperature, T_B (°C)	91
Chamber Temperature, T_C (°C)	215

Similar to P220 experimental data, noise due to the nozzle heat was observed particularly at the first minute of the layer temperature readings during the printing process (Fig.5.14 (A)). After the first minute of printing, the descending reheating effect was noted during the whole printing period. The cooling distributions of layers were decreasingly declining from lower to upper layers (Fig.5.14 (B-C)). Once the print job was finished, the print bed moved to the new location for the cooling stage. The temperature data was not collected until the print bed reached its stable location.

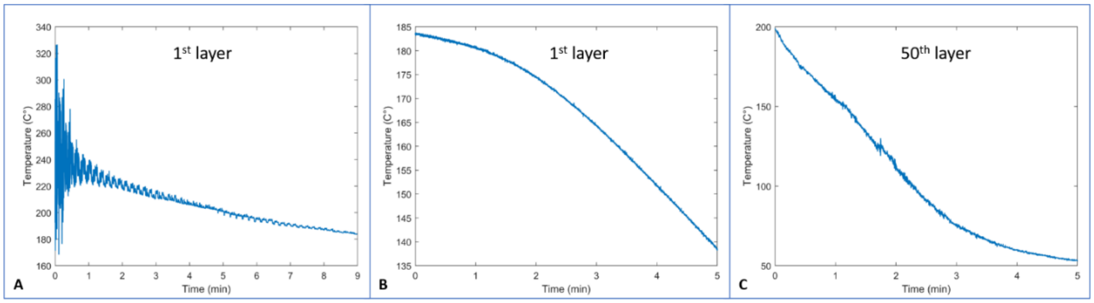

Figure 5. 14. The temperature data for printing (A) and cooling (B-C) stages of the FFF process were analyzed separately before plotting the entire temperature distributions of each FFF PEEK layer printed with M220.

Furthermore, the first layer temperature (327°C) decreased to 220°C in the first two minutes and reached 185°C by the end of the print (Fig. 5.15 (A)). For the 11th layer, the highest temperature was 316°C that decreased to 226°C in two minutes and 190°C when the cube was completely printed (Fig. 5.15 (B)). The highest layer temperature, the temperature at two minutes, and the temperature at the end of the FFF process were 317°C, 228°C, and 199°C, respectively for the 21st layer (Fig. 5.15 (C)). The temperature readings of the 31st layer were 318°C, 227°C, and 211°C for the highest layer temperature, the temperature at two minutes, and the temperature at the end of the FFF process, respectively (Fig. 5.15 (D)). For the 41st layer, the temperature decreased from 318°C to 214°C in two minutes and print ended for the layer before two minutes where the temperature was 224°C (Fig. 5.15 (E)).

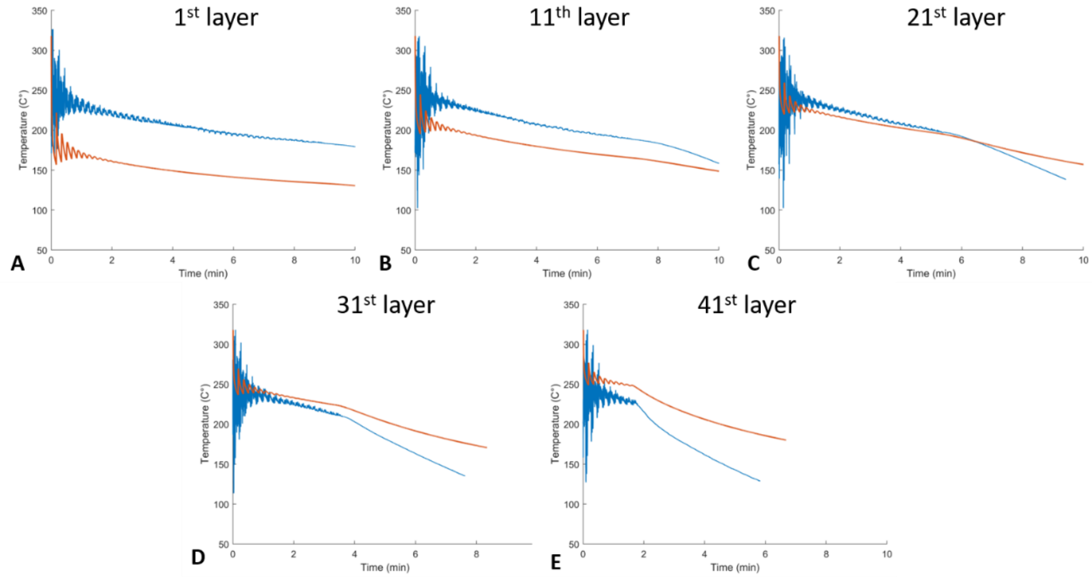

Figure 5. 15. The model (red) vs experimental (blue) temperature distributions of FFF PEEK layers were studied for the M220 machine. Similar to P220 validations, experimental layer temperatures were higher compared to the model for lower layers (A-B), whereas by the mid-layers the HTM results and the experiments were in good agreement (C). After the mid-layer, experimental layer temperatures stayed lower than the model approximations (D-E).

It was observed that the temperature predictions of the model overlapped with the experimental temperatures measured for mid-layers of the FFF PEEK cube (Fig. 5.16). The model predicted the layer temperature distributions lower for the lower layers and matched well for the mid-part of the object. By the 30th layer, the model approximations started to remain higher for layers and the difference increased to the top of the FFF PEEK cube. Additionally, after the first quarter of the cube, the cooling profile of the HTM recognized it to remain higher than the experimental readings.

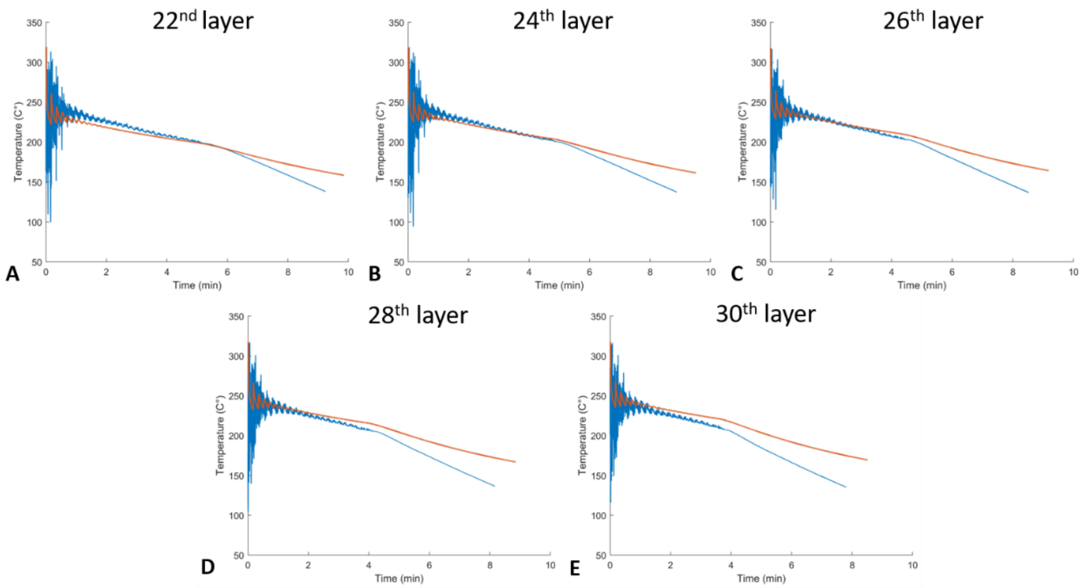

Figure 5. 16. The HTM results (red) supported the experimental layer temperatures (blue) specifically for mid-layers. Printing profiles of the model initiated below the FFF layer temperatures (A-B), whereas fitted almost completely for the mid-layers (C). After mid-layers, the layer temperature predictions settled slightly higher for the printing stage (D-E).

Other than the model validation of the layer temperatures during printing and cooling processes, the model predictions of layer temperatures at the very beginning of the print were investigated which are crucial for healing mechanisms (Fig.5.17). Despite the experimental data when plotted for shorter times appearing to be noisier, it was acknowledged that the HTM layer temperatures agreed accurately with the FFF layer temperatures, specifically after the first 20 layers.

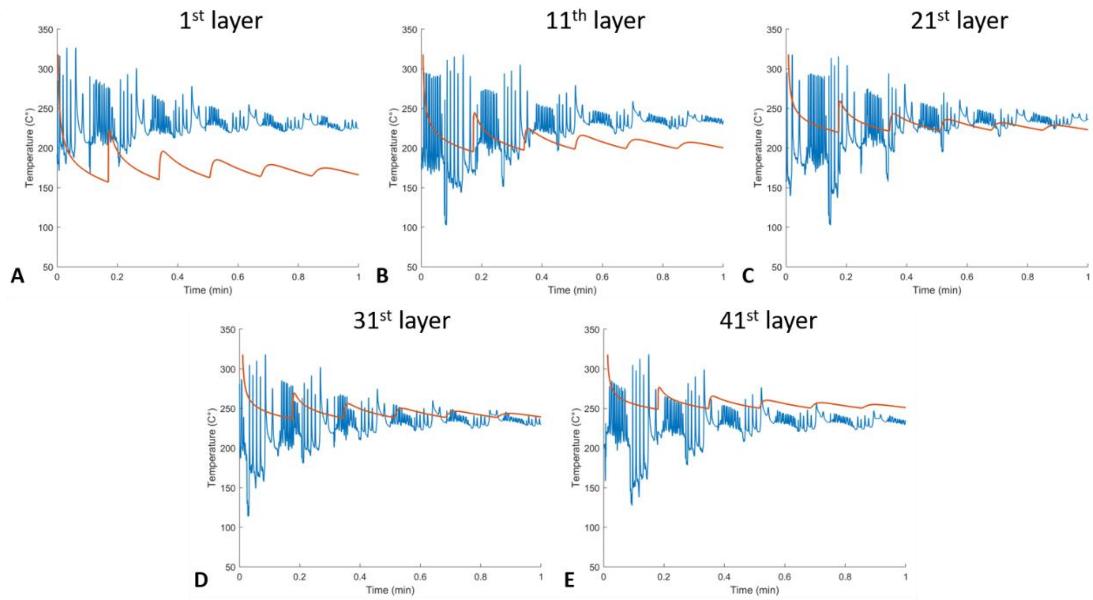

Figure 5. 17. Although the experimental layer distributions (blue) were certainly affected by the extruder while printing, the incremental convergence of the model (red) and the experiments from the beginning to the end of the FFF PEEK cube was remarkable (A through E).

5.5 Discussion

Heat transfer analysis has been used to access the temperature history of FFF builds for further part optimization [19]. In the previous chapter, a 1D HTM was proposed to achieve the temperature history of both layers and interlayers for a FFF PEEK build, that would be implemented in a healing model to investigate the FFF PEEK integrity. Before examining the entire model, it is necessary to validate the HTM temperature predictions with the experimental data from FFF PEEK. Hence, in this study, thermal videos were recorded while printing the FFF PEEK cubes in industrial (2nd) and medical (3rd) generation FFF machines. As the HTM model earlier presented, the experimental layer temperatures also stayed higher during the printing phase for upper layers compared to the lower layers of the FFF PEEK cube for both printers. For the 2nd generation (P220) machine, the temperature predictions for the printing profile were closest in the mid-part (around 30th layer) of the build, in which the cooling profile remained slightly higher. To operate the HTM for the 3rd generation (M220) machine, necessary modifications were performed in the model due to the imperative raft printed underneath the cube design. The best agreement between the model and experimental data for the printing period in the M220 machine was observed between the 24th and 26th layers, while the experimental cooling profile was under the model. Additionally, short-term approximations, which would be important for the degree of healing studies, provided more insight into how the model fitted the experimental data. For both machines, the approximations were more consistent after the 20th layer in the first minute of the print. The results of this study presented a feasible validation technique for layer temperature assessment of FFF PEEK builds, which concluded that the 1D HTM can be employed further in the healing model for mechanical strength optimization of the FFF PEEK implants.

There were some limitations involved in this study. Firstly, the thermal measurements were collected leaving the printer door open in both machines due to the capability of the thermal camera. However, to preserve the heat inside the printers as much as possible, insulation boards were covered around the camera during recordings. Additionally, the FLIR camera was required to be placed at a certain distance (25 cm) from the heat source (the print area) for safety, which limited the resolution of the thermal videos/images. Moreover, the bed and chamber temperatures were calculated in designated areas from the thermal videos, however, the actual temperatures might vary. The bed temperature, where the PEEK cube was being printed, was not able to be measured during the FFF process. Additionally, the nozzle (extruder) could not be avoided for the environment temperature valuations, which affected the chamber temperature conducted in this study. In the same manner, the noise because of the nozzle location on top of the print area was inevitable for the experimental layer temperatures especially for the first couple minutes of the prints. The temperature of the material (PEEK) particularly during extrusion needs to be explored in the future, which was found via the maximum layer temperatures. In both FFF systems, once the print job was finished, the print bed moved to the new location for cooling. The cooling temperatures were not collected until the print bed reached its stable location. The distance between the nozzle tip and the print build during cooling was set for both printers by the manufacturer. Different distance settings would affect the cooling profiles differently. Finally, although the previously developed HTM with a constant conduction boundary at the print base was applied for the M220 printer, there was additional convective heat transfer occurring due to the hot air flow underneath the print bed which requires additional considerations.

First, it should be noted that the experimental temperature measurements for the nozzle (T_N), print bed (T_B), and the chamber (T_C) were employed in the model for both FFF printers which were different than the FFF temperature settings. The nozzle temperature indicated for the P220 machine was 440°C, whereas the maximum layer temperature measured of the FFF PEEK cube via thermal camera was 344℃. The same nozzle temperature setting was applied in the M220 printer and 318℃ was calculated for the maximum layer temperature. The difference between the FFF setting of the nozzle temperature and the maximum extrusion temperature of the material might be occurring due to the journey of molten PEEK from the extruder, where it is heated, to the tip of the nozzle and deposition of it as a layer. This difference was also recognized and taken into the consideration by Costa et al. [15] while studying FFF ABS filament temperatures. They mentioned the ABS filament temperature at the nozzle exit was 190℃ and 200℃ when the nozzle temperature (referred to as die) was set to 200℃ and 210℃, respectively. Moreover, the bed temperature (T_B) was placed to 130℃ in the P220 machine, however, an experimental bed temperature value around the PEEK cube (95℃) was adopted in the HTM. As there is no bed temperature setting but the airflow (180℃) in the M220 printer, 91℃ was determined from the bed surface to establish in the model. In the same manner, the temperature variation (40-65℃) in the print bed was noticed depending on the distance to the extruder for FFF ABS [15].

We acknowledged the noise due to the extruder heat in experimental temperature distributions collected from both FFF machines in this study. Similarly, Ravoori et al. [17] indicated that the temperature increment at the concerned point may be influenced by the heat source (nozzle) in addition to thermal energy diffusion by the dispensed PLA filament. They suggested that conductive heat transfer might play a role as well due to the adjacency of the nozzle tip since the nozzle tip is in contact with the material during extrusion. Moreover, as revealed by the HTM in the previous chapter, we noticed that experimental layer temperatures in both machines were higher for the upper layers compared to the lower layers in reference to the print bed. The higher temperatures for the longer were declared for the upper filaments compared to the lower filaments which were in physical contact with the print bed for FFF ABS as well [15]. When the experimental layer temperatures achieved from the P220 printer were compared with the HTM model, it was shown that for the layer closer to the print bed, the model estimations were lower compared to the experimental temperatures. This might be due to the bed temperature in the print area being higher than the value used in the model. Additionally, the sandwich effect of the heated plate around the nozzle and the print bed might be accelerating the bed temperature which would be more remarkable for lower layers. For instance, even when Compton et al. [16] 3D printed a thin wall geometry (lines rather than layers), their first layer temperature predictions were lower than the experimental temperatures via thermal readings. The gap between the model and experiments diminished as mid-layers were approached, since the layer below, for which the most accurate temperature approximation was done in the model according to the maximum layer temperatures measured via thermal videos, would be the new conduction boundary. Thus, the model predictions for FFF PEEK layers, when printed in the P220 machine, were in good agreement after the 25th layer which was more recognizable when the convergence was investigated in the first two minutes (25%) of the print. Finally, as the printing profile approximations of the model converged to the experimental temperatures, the cooling profile of the model was slightly higher. Additionally, a raise can be seen in some temperature profiles during cooling, especially for the first half of the cube, which is due to the confidential cooling procedure in the P220 machine.

Furthermore, similar to the model comparisons with the experimental temperatures, the model predictions were converging to the FFF PEEK layer temperatures from the M220 machine in the mid-layers. The reason why the convergence happened earlier, for instance, the smaller gap between the model and the experiments for the lower layers, was the raft involved in the model as well as in the experiments. In other words, the first layer from the PEEK cube was the 13th layer in the build after the raft (12 layers) and was not directly affected by the print bed temperature but the preceding layer temperature. This confirmed our interpretations about the dominance of the conduction boundary temperature in the model, suggesting the print bed and its variation during the FFF process need to be investigated further in detail when adopting this model. In addition to the whole print duration (printing and cooling stages) model comparisons, short term comparisons in the M220 machine proved that the model may estimate the FFF PEEK layer temperatures even more accurately with the enhanced FFF temperature estimations in the future.

Heat transfer mechanisms were analyzed in detail for FFF PEEK in the previous chapter and a 1D HTM was developed for temperature predictions that would be used to calculate the degree of healing between the PEEK layers. It is crucial to understand the model capabilities by validating the temperature distribution estimations with experiments since the layer temperature assumptions will be further involved in the non-isothermal healing model. This study presents initial investigations for the HTM model validation of FFF PEEK layers printed with industrial and medical generation FFF machines. The validation studies of HTM presented here are the first steps towards temperature evaluations of FFF PEEK builds for further optimization. The correlation between the model and the experimental results from different FFF systems support the promising future of the proposed HTM for FFF PEEK implants.

5.6 References

1. Basgul, C., et al., *Structure-property relationships for 3D printed PEEK intervertebral lumbar cages produced using fused filament fabrication.* J Mater Res, 2018. **33**(14): p. 2040-2051.
2. Basgul, C., et al., *Thermal localization improves the interlayer adhesion and structural integrity of 3D printed PEEK lumbar spinal cages.* Materialia, 2020. **10**: p. 100650.
3. Delaney, L.J., et al., *Ultrasound-triggered antibiotic release from PEEK clips to prevent spinal fusion infection: Initial evaluations.* Acta Biomater, 2019. **93**: p. 12-24.
4. Prechtel, A., et al., *Fracture load of 3D printed PEEK inlays compared with milled ones, direct resin composite fillings, and sound teeth.* Clinical Oral Investigations, 2020.
5. Zhang, C., et al., *Bionic design and verification of 3D printed PEEK costal cartilage prosthesis.* Journal of the Mechanical Behavior of Biomedical Materials, 2020. **103**: p. 103561.
6. Berretta, S., K. Evans, and O. Ghita, *Additive manufacture of PEEK cranial implants: Manufacturing considerations versus accuracy and mechanical performance.* Materials & Design, 2018. **139**: p. 141-152.
7. Zhong, R., et al., *Clinical application of triangular parabolic PEEK mesh with hole button produced by combining CAD, FEM and 3DP into cranioplasty.* Biomedical Research, 2018. **29**.
8. El Halabi, F., et al., *Mechanical characterization and numerical simulation of polyether-ether-ketone (PEEK) cranial implants.* J Mech Behav Biomed Mater, 2011. **4**(8): p. 1819-32.
9. Wang, L., et al., *Three-Dimensional Printing PEEK Implant: A Novel Choice for the Reconstruction of Chest Wall Defect.* The Annals of Thoracic Surgery, 2019. **107**(3): p. 921-928.
10. Kang, J., et al., *Custom design and biomechanical analysis of 3D-printed PEEK rib prostheses.* Biomechanics and Modeling in Mechanobiology, 2018. **17**(4): p. 1083-1092.
11. Thomas, J. and J. Rodriguez, *Modeling the fracture strength between fused-deposition extruded roads.* Proc. Solid Freeform Fabr. Symp, 2000: p. 16-23.

12. Bellehumeur, C., et al., *Modeling of Bond Formation Between Polymer Filaments in the Fused Deposition Modeling Process.* Journal of Manufacturing Processes, 2004. **6**(2): p. 170-178.

13. Yin, J., et al., *Interfacial bonding during multi-material fused deposition modeling (FDM) process due to inter-molecular diffusion.* Materials & Design, 2018. **150**: p. 104-112.

14. Wang, P., B. Zou, and S. Ding, *Modeling of surface roughness based on heat transfer considering diffusion among deposition filaments for FDM 3D printing heat-resistant resin.* Applied Thermal Engineering, 2019. **161**: p. 114064.

15. Costa, S.F., F.M. Duarte, and J.A. Covas, *Estimation of filament temperature and adhesion development in fused deposition techniques.* Journal of Materials Processing Technology, 2017. **245**: p. 167-179.

16. Compton, B.G., et al., *Thermal analysis of additive manufacturing of large-scale thermoplastic polymer composites.* Additive Manufacturing, 2017. **17**: p. 77-86.

17. Ravoori, D., et al., *Experimental and theoretical investigation of heat transfer in platform bed during polymer extrusion based additive manufacturing.* Polymer Testing, 2019. **73**: p. 439-446.

18. Jiang, X.J. and P.J. Scott, *Chapter 11 - Characterization of free-form structured surfaces*, in *Advanced Metrology*, X.J. Jiang and P.J. Scott, Editors. 2020, Academic Press. p. 281-317.

19. Costa, S., F. Duarte, and J. Covas, *Using MATLAB to Compute Heat Transfer in Free Form Extrusion*. 2011.

Chapter 6: Conclusions and Future Work

This thesis aimed to investigate the interlayer debonding phenomenon which was stated for FFF PEEK implants [1, 2]. The execution of these objectives through the thesis provides a direct assessment of FFF PEEK layers' interface bonding with the help of two-compartment model allowing for parameter optimization in future FFF PEEK implants. In the beginning, AM PAEKs for implant applications were outlined evidencing the growing research interest in AM-POC, especially for FFF PEEK. Later, the parameters which indirectly regulate the layer cooling were identified to 3D print PEEK cages in the first two generation FFF machines expressing the consequences of the thermal mechanisms involved in layer adhesion. In the light of these findings, a heat transfer model was designed to predict the interface temperatures for a FFF PEEK build. Moreover, the layer interface temperature history was further utilized in a non-isothermal healing model that identified the degree of healing at each interface through the printed PEEK part. The effect of three key temperatures of the FFF system on the layer healing was exhibited via model. The model can be leveraged to optimize the parameters for enhanced interlayer adhesion in FFF PEEK implants. Finally, the first compartment of the model, for its further implementation into the healing model, was validated with experimental temperatures of FFF PEEK cubes printed in medical and industrial FFF machines.

The systematic review presented in the second chapter summarized the current Additive Manufacturing of PAEK aiming towards implant applications. We intended to identify the investigations in the literature to help to stimulate the guidelines and regulations in 3D printing PAEK implants forward for POC AM. The interest in FFF was found to be more (63%) compared to SLS systems and among these FFF studies, a great majority focused on PEEK implants (92%). The impact of the thermal mechanisms in FFF PEEK was emphasized in the review by the choice of implant number printed in a single build which significantly impacted the mechanical strength of spinal implants [2]. Despite the ongoing preclinical research for AM PAEK, 20 patients in total were implanted with FFF PEEK PSIs clinically. It is noted that these studies manufactured the FFF PEEK implants with self-developed printers and unconfirmed medical grade materials and did not clear the regulations followed. Although in general successful outcomes were reported [3, 4], failure of the FFF PEEK scapula was reported after three months of implantation [5]. Thus, careful considerations in FFF PEEK implants must be conducted to determine the failure mechanisms.

In the first aim of this research, FFF parameters (that indirectly control the thermal conditions) were investigated on the mechanical properties and microstructure of standardized spinal cages printed with two generations of FFF machines. As temperature conditions were kept constant, the nozzle size, print speed, layer thickness, and the number of cages fabricated per build were varied. The cage crystallinity was not associated with the manufacturing method (AM vs traditional), hence supporting that print defects at the microscale cause the differences between the FFF and machined PEEK cages. Our hypothesis was validated by changing printing conditions that decrease the cooling time of a layer improved the interlayer adhesion and strength of 3D printed PEEK cages. Printing a single cage at a time with a bigger nozzle significantly showed higher forces prior to failure. For instance, single 3D printed cages printed with both printer generations exceeded 10kN before failure and achieved 86% ultimate load of the traditionally machined PEEK cages. While finer details and microstructures could demand a smaller nozzle diameter, the increase in printing time of the implants which leads to longer layer cooling times should be observed carefully to avoid the mechanical strength reduction. The layer thicknesses and the print speeds explored in this study were neither associated with the layer cooling time nor affect the mechanical outcomes of FFF PEEK implants. Treatment of the PEEK filaments prior to printing was necessary since moisture absorption affected the internal porosity of FFF PEEK implants. Interestingly, even though FFF temperature settings were different between the two generations of FFF printers, there was not a strength difference between cages printed. Furthermore, altering the FFF parameters with fixed temperature conditions did not change the failure mechanism of FFF cages which still failed due to layer detachment. These conclusions from Aim 1 emphasized: (1) the importance of discussions in Aim 2 about the accomplished model to understand the thermal mechanisms in FFF that affect the layer healing and (2) the necessity of FFF systems' temperature validations in Aim 3 for authenticating the heat transfer mechanisms. In this study, we were restricted by the capabilities of 3D printers utilized (e.g., nozzle diameter, print head speed, print bed dimensions, and constant temperature conditions controlled during the print), which were the first two generations of Apium

PEEK printers. Further studies might investigate the associations between the mechanical and micro-structural outcomes and the FFF PEEK cages with different FFF machines and/or changes in the current configurations.

The significance of heat management in layer bonding strength to achieve stronger FFF PEEK cages was highlighted in the first aim [2, 6]. Within the second aim, a heat transfer-based polymer healing model was formulated to determine the layer healing of a FFF PEEK build for further mechanical strength evaluations depending on the selected FFF parameters. The model was designed separately involving two compartments: (1) 1D transient heat transfer model and (2) non-isothermal polymer healing model. The specified ranges of temperature distributions acquired from the HTM were employed in the healing model. According to the model, the degree of healing increased linearly from lower, closer to the print bed, to the upper layers of the FFF PEEK cuboids.

With the FFF settings conducted to print cages, more than half of the layers were not healed completely, which can be enhanced via increasing the key FFF temperatures (nozzle, bed, and environment) based on the model. The model helped to define the insufficiently healed layers through FFF PEEK build, which could trigger layer debonding under biomechanical loads for FFF PEEK implants. Hereby, the heat transfer based non-isothermal polymer healing model was demonstrated as an appropriate approach to optimize both the direct and indirect thermal parameters in a FFF system by quantifying the layer healing degree of FFF PEEK builds. As for the first investigations, assumptions were made for the 1D HTM design. Further studies could develop more complex models (e.g., 2D and 3D) for the FFF PEEK layer temperature analysis. Furthermore, in this model instant deposition of layers was assumed. For additional examinations, gradual deposition of a layer can be simulated to have more a precise temperature distribution through the layer. However, they might consider the limitations of numerical solutions that as precision is desired to be improved, the solution time and total error increase. In addition, for the healing calculations, the welding function for PEEK filaments needs to be experimentally governed in the following explorations. Moreover, future work could investigate the functions of the temperature distributions for healing calculations that were assumed to be linear in this model. Upcoming investigations would be helpful in material-dependent properties of PEEK filaments when utilizing this model under unstable FFF processes.

Validation of FFF filament temperatures instantaneously and layer temperature measurements was done for open-air FFF systems [7-9]. However, experimental FFF PEEK layer temperature measurements remained unclear. In the last aim, validation studies were conducted on the first component of the model which was the HTM designed to achieve the FFF PEEK interface and layer temperatures. Thermal videos collected from industrial (2^{nd}) and medical (3^{rd}) generation FFF machines were analyzed to derive FFF PEEK layer temperatures in this study. Experiments from both printers confirmed that the upper FFF PEEK layers, in reference to the build plate, stayed higher compared to the lower layers. In both machines, the model predictions converged the experimental layer temperatures around mid-layers. For the medical generation printer, the convergence happened earlier due to the additional raft layers underneath the part. Since approximated layer temperatures were depended on maximum layer temperatures measured via thermal videos, the newly deposited layer as conduction boundary was the most accurate boundary temperature. The dominance of the conduction boundary (print bed) especially for the lower layers was recognized. Determination of the build plate temperature and the variations during the FFF process were suggested as further considerations for future studies that adopt HTM. Moreover, in both machines, slightly more in medical generation machine, cooling profile estimation of the model stayed higher than the experimental temperatures. This could be due to the limitation of an unclosed print door which would cause faster heat loss than in an enclosed environment. In addition to introducing a feasible validation technique to assess FFF PEEK layer temperatures, this aim executed the first steps in understanding the thermal processes of FFF to manufacture PEEK implants. The experimental temperatures from the medical FFF printer were reasonably in agreement with the heat transfer model approximations on FFF PEEK layer temperatures. Nonetheless, modifications in the current model may be engaged for future models depending on the FFF technology design such as the additional convection due to the hot airflow. Despite the previous explanations on healing for semi-crystalline polymers indicated that the healing occurs above the melting temperatures, the experiments from both FFF machines revealed that the layer temperatures were either quite close or below the melting temperature of PEEK once deposited. Hence, non-isothermal healing models are required to be improved on the defined temperatures where healing exactly occurs for semi-crystalline polymers like PEEK. For instance, crystallization temperature is a crucial parameter while additively manufacturing PEEK that is not mentioned in the previous healing models [10]. Further supporting the above considerations, it was stated that the accuracy of the non-isothermal healing formula utilized can be affected by the crystallinity of the material resulting from cooling [11]. Moreover, previous investigations were based on the reptation theory when intimate surface contact was achieved which was ensured with pressure in traditional manufacturing methods. Future efforts should consider developing more comprehensive healing models for FFF layers that discuss the layer deposition and the contact due to the gravitational forces without incorporating additional pressure. It is evident that the above recommendations should be embraced for the healing model validation moving forward.

In summary, this body of work outlined thermally driven interlayer bonding mechanisms in FFF PEEK, highlighting the importance of heat transfer mechanisms in the FFF system to manufacture PEEK implants for AM-POC. First, the effect of indirect thermal parameters on layer cooling was proved experimentally in FFF PEEK cages. Printing single cages at a print build with a bigger nozzle diameter resulted in significantly higher failure forces. However, 3D printed cages still failed due to interlayer detachment phenomena of FFF. A heat transfer based non-isothermal healing model is proposed to estimate the degree of healing between FFF PEEK layers. The model suggested the increase in main temperatures of the FFF system (bed, nozzle, and environment) would increase the layer healing through the FFF PEEK builds. However, printability in these temperatures should be experimentally studied further. The heat transfer section of the model was validated with the FFF machine designed for clinical use. The studies described in this thesis can be used to influence the patient-specific PEEK implants by optimizing the printing process.

6.1 References

1. Sharma, N., et al., *Quality Characteristics and Clinical Relevance of In-House 3D-Printed Customized Polyetheretherketone (PEEK) Implants for Craniofacial Reconstruction.* J Clin Med, 2020. **9**(9).
2. Basgul, C., et al., *Thermal localization improves the interlayer adhesion and structural integrity of 3D printed PEEK lumbar spinal cages.* Materialia, 2020. **10**: p. 100650.
3. Kang, J., et al., *Custom design and biomechanical analysis of 3D-printed PEEK rib prostheses.* Biomechanics and Modeling in Mechanobiology, 2018. **17**(4): p. 1083-1092.
4. Wang, L., et al., *Three-Dimensional Printing PEEK Implant: A Novel Choice for the Reconstruction of Chest Wall Defect.* The Annals of Thoracic Surgery, 2019. **107**(3): p. 921-928.
5. Liu, D., et al., *Application of 3D-printed PEEK scapula prosthesis in the treatment of scapular benign fibrous histiocytoma: A case report.* Journal of Bone Oncology, 2018. **12**: p. 78-82.
6. Basgul, C., et al., *Structure-property relationships for 3D printed PEEK intervertebral lumbar cages produced using fused filament fabrication.* J Mater Res, 2018. **33**(14): p. 2040-2051.
7. Costa, S.F., F.M. Duarte, and J.A. Covas, *Estimation of filament temperature and adhesion development in fused deposition techniques.* Journal of Materials Processing Technology, 2017. **245**: p. 167-179.
8. Ravoori, D., et al., *Experimental and theoretical investigation of heat transfer in platform bed during polymer extrusion based additive manufacturing.* Polymer Testing, 2019. **73**: p. 439-446.
9. Compton, B.G., et al., *Thermal analysis of additive manufacturing of large-scale thermoplastic polymer composites.* Additive Manufacturing, 2017. **17**: p. 77-86.
10. Chen, P., et al., *Crystallization kinetics of polyetheretherketone during high temperature-selective laser sintering.* Additive Manufacturing, 2020. **36**: p. 101615.
11. Lee, W.I. and G.S. Springer, *A Model of the Manufacturing Process of Thermoplastic Matrix Composites.* Journal of Composite Materials, 1987. **21**(11): p. 1017-1055.

Appendix

Appendix A: Heat Transfer and Degree of Healing Model Scripts

Additive manufacturing heat transfer-based degree of healing model file

```
%AM_HT_DOH.m
%% Heat Transfer Model
L=0.01; %m, Wall thickness
layers=50;  % N umber of layers
T0=344;  %Initial temperature of wall
Tbed=95; % Surface 1 temperature (Print Bed)
Tinf=213; % Surface 2 temperature (Chamber Temperature)
h=naturalconvectioncoefficient(Tinf); % heat transfer coefficient
k=0.29; %thermal conductivity
cp=1957; %specific heat capacity (J/kg.K)
rho=1300; %density (kg/m3)

layerheight=L/layers; %m, layer height
nodesperlayer=1; % located in the middle
dx=layerheight/(nodesperlayer+1); %nodal distance
nodes=(layers*2)+1; %total points to calculate the temperatures for

alpha=k/(cp*rho); %thermal diffusivity

dt1=(dx)^2/(2*alpha*((h*dx/k)+1)); %stability for convection BC
dt2=(dx)^2/(2*alpha); %Stability for conduction BC
dt=min(dt1,dt2)*0.75;     %s, fixed time step according to stability

kappa=(alpha*dt)/dx^2; %constant for the heat transfer model
x=linspace(0,L*1000,layers+1); % distance in reference to print bed

layertime=10; % Physical time between deposition of each new layer
(seconds)
timepoints = floor(layertime/dt) + 1;
totaltimepoints=timepoints*layers;

cooldowntime = 300;  %seconds
cooldowntimepoints = floor(cooldowntime/dt);
 temporary = 0;

Tnodes=NaN(totaltimepoints+cooldowntimepoints,nodes); % Temperature
matrix to keep the data in each time step

%Initial conditions
 for n = 1:layers
```

```
   if n==1
       Tnodes(1, [1:nodesperlayer+2]) = T0;
   elseif n==layers
       temporary = cooldowntimepoints;
       Tnodes(((n-1)*timepoints + 1), [ n*(nodesperlayer+1)-
1:n*(nodesperlayer+1)+1]) = T0;
   else
       Tnodes(((n-1)*timepoints + 1), [ n*(nodesperlayer+1)-
1:n*(nodesperlayer+1)+1]) = T0;
   end

%Solutions for temperature (j)
   for j = ((n-1)*timepoints + 1):(n*timepoints +temporary)

       Tnodes(j+1,1)=(1-
2*kappa)*Tnodes(j,1)+kappa*(Tnodes(j,2)+Tbed);

 % Solution for middle nodes with convective cooling and conduction
(iteration through nodes (i))
    for i = 2:n*(nodesperlayer+1)+1

      if i==n*(nodesperlayer+1)+1
         Tnodes(j+1,i)=kappa*((1/kappa-((2*h*dx)/k)-
2)*Tnodes(j,i)+2*Tnodes(j,i-1)+(2*h*dx*Tinf)/k);
      else
        Tnodes(j+1,i)=(1-
2*kappa)*Tnodes(j,i)+kappa*(Tnodes(j,i+1)+Tnodes(j,i-1));

      end

    end

   end

 end

 time = [0:dt:(layers*timepoints+cooldowntimepoints)*dt]';
%conversion of the time points into time (seconds)

 layer_points=[2:2:100]; %mid points of the layers
 intlayers=[3:2:99]; %interlayer points
 layerpicks=[2,22,42,62,82]; %1,11,21,31,41th layers

 plot((time./60, Tnodes(:,layerpicks),'LineWidth',2)
 xlabel("Time (min)","fontsize",11)
 ylabel("Temperature (C°)","fontsize",11)
 axis([0 0.2 50 350]);

%%Interlayer Healing Model
Temperature={};
IntTemperatures={};

syms t
for k=1:layers-1
```

```
    Temp=Tnodes(timepoints*k+1:timepoints*(k+1),(k*2)+1); % for each
layer temperature interval for 10 seconds
    IntTemperatures{k}=Tnodes(timepoints*k+1:end,(k*2)+1);
%Temperatures of interlayers
    Temperature{k}=Temp(Temp>343); %Temperatures greater than melting
point of PEEK
    it(k)=length(Temperature{k});
    time2{k}=linspace(0,it(k)*dt,it(k));

    a(k)=(Temperature{k}(1)-Temperature{k}(end))/(time2{k}(end)-
time2{k}(1)); %slope of the line
     b(k)=Temperature{k}(1); %constant for the linear line equation

F=integral(@(t)(1./(((1./44.1)*exp(3810./(a(k).*t+b(k)))).^(1/4))),0,
it(k)*dt); % non-isothermal degree of healing formula
    Dh(k)=F^(1/4); %non-isothermal degree of healing
end

figure; %Degree of healing Graph
   plot(x(2:50),Dh,'LineWidth',1)
   xlabel("Distance (mm)","fontsize",11)
   ylabel("Degree of Healing","fontsize",11)
   axis([0 10 0.3 1.50]);
```

Appendix B: Function Script for Natural Convection Coefficient

```
%naturalconvectioncoefficient.m
function h=naturalconvectioncoefficient(Tinf)


Tsurface=342; %temp of the material (C)
L=0.01; %wall height (m)
rho_surface=1.214; %fluid density (kg/m3)
v=1.493*10^(-5); %fluid viscosity (m2/s)
cp= 1005; %fluid specific heat (J/kg.K)
k=0.0256; %fluid thermal conductivity (W/m.K)
beta=3.44*10^(-3); %fluid thermal expansion coefficient (1/K)
g=9.81; %gravity
alfa_fluid= k/(rho_surface*cp); %thermal diffusivity in a fluid
Pr=v/alfa_fluid; %Prandtl number
Gr= (g*beta*(Tsurface-Tinf)*(L^(3)))/(v^(2)); %grashof number
Ra= Pr*Gr; %Rayleigh number

Nu= (0.825 + 0.387*( Ra^(1/6)/(1+(0.492/Pr)^(9/16))^(8/27)))^2;
%Nussel number

h=(Nu*k)/L; %natural convection coefficient;

end
```

Appendix C: Thermal Image Analysis Scripts to Obtain the Experimental Layer Temperatures

Image Reading and Transfer

```
%readfile.m

info = imfinfo('Rec-000034.tif');


data = zeros(46492,150,150);
counter =1;
for i = 4000:50491
    frame = imread('Rec-000034.tif',i);
    data(counter,:,:) = frame(331:330+150,245:244+150);
    counter = counter + 1
end
save data1.mat data -v7.3
```

Edge Detection Algorithm

```
edgedetect.m
load('data1.mat')
pos = zeros(46492,1); %position defined for the line to be detected

k = 1;

for j = 1:46492
    image = squeeze(data(j,:,:));
    BW = edge(image,'Sobel',7,'horizontal');
    X =57;
    Y=51;
    line = BW(X+1:end,Y);

    for i=1:(150-(X+1))
        pixval = line(i);

        if(pixval == 1)
            pos(k) = i + X;
            break
        end
    end

    k = k +1;

end
```

Layer Temperature Assignment

```
getdatalayers.m
function data_layer = GetDataLayers(data)

    n_layer = size(data,1);
    n_data = size(data,2);

    layer_val = NaN(n_layer,n_data);
    time_points = floor(linspace(1, n_data, n_layer + 1));

    for i=1:n_layer
        track=0;
        for j=i:length(time_points)-1
        track=track+1;

layer_val(i,time_points(j):time_points(j)+(time_points(j+1)-
time_points(j)))=track;
        end
    end


    for j=1:n_layer
        layertemp=[];
        for i=1:size(layer_val,1)-j+1
            ind=find(layer_val(i,:)==j);
            layertemp=[layertemp, data(i,ind)];
        end
        data_layer{j}=layertemp;

    end

end
```

Temperature Analysis of Layers

```
tempanalysis.m
load('data1.mat')
midpoint=data(4206:29690,56:94,76);
J = imresize(midpoint, [25484 50] , 'bilinear');
J2=J';

data_layers=GetDataLayers(J2);
midpoint_cool=data(29800:45240,97:135,76);
D = imresize(midpoint_cool, [15441 50] , 'bilinear');
D2=D';

for i=1:50
    data_layers{i}=[data_layers{i}, D2(51-i,:)];
end

dt= 0.0200; % frequence of the video taken (50Hz)

layerpicks={};
time={};
```

```
for j=1:5
   layerpicks{j}=data_layers{(10*(j-1))+1};  %layers selected to
display layerpicks=[1,11,21,31,41]
   %layerpicks{j}=data_layers{20+(j*2)}; %layers selected to display
layerpicks=[22,24,26,28,30]
    time{j} =
linspace(0,(size(layerpicks{j},2))*dt,(size(layerpicks{j},2)));
%frame to secs

%     figure;
%     plot(time{j}./60, layerpicks{j},'LineWidth',1)
%         xlabel("Time (min)","fontsize",11) %frame to sec *Hz value
%         ylabel("Temperature (C)","fontsize",11)
end

A=time{3};
B=layerpicks{3};
figure;
hold on
    plot(A/60, B,'LineWidth',1)

        xlabel("Time (min)","fontsize",11) %frame to sec *Hz value
        ylabel("Temperature (C°)","fontsize",11)

for i=1:50 % to calculate the max layer temperature as the model
input

     maxtemp(i)=max(data_layers{i});
 end
 averagemaxtemp=mean(maxtemp);
```

Vita

Cemile Basgul

Education

Drexel University — Philadelphia, USA

Doctorate Degree of Biomechanical Engineering — 09-2016/01-2021

Advisors: Dr. Steven M. Kurtz & Dr. Kenneth Barbee

*CGPA:*3.95/4.00

TOBB ETU — Ankara, Turkey

Master's Degree of Mechanical Engineering — 09-2013/06-2016

Advisors: Dr. Teyfik Demir

*CGPA:*3.86/4.00

TOBB ETU — Ankara, Turkey

Bachelor's Degree of Industrial Engineering — 09-2009/09-2013

Advisors: Prof. Dr. İsmail Burhan Türkşen & Dr. Sibel Alumur Alev

CGPA: 3.60/4.00

Professional Experience

Drexel University — Philadelphia, USA
Implant Research Center — 09-2016/in progress
Research Assistant
Optimization FFF PEEK for medical devices & Investigation of other AM techniques for implants

TOBB ETÜ — Ankara, Turkey
Research and Teaching Assistant — 09-2013/06-2016
Pedicle screw designs & application techniques

Publications

- Spece H., **Basgul C.**, Andrews C.E., MacDonald D.W., Taheri M.L., Kurtz S.M., A Systematic Review of Preclinical in vivo Testing of 3D Printed Porous Ti6Al4V for Orthopaedic Applications, Part I: Animal Models and Bone Ingrowth Outcome Measures. *Journal of* Biomedical Materials Research Part B: Applied Biomaterials, Accepted Jan 2020. Doi: 10.1002/jbm.b.34803.
- **Basgul C.**, Spece H., Sharma N., Thieringer M.T., Kurtz S., Structure, Properties, and Bioactivity of 3D Printed PAEKs for Implant Applications: A systematic review. *Journal of Biomedical Materials Research Part B: Applied Biomaterials*, Submitted Sep 2020. Under review.
- Garcia-Leiner, M., Streifel, B., **Basgul, C.**, MacDonald, D.W., Kurtz, S.M. Characterization of paek filaments and printed parts produced by extrusion-based additive manufacturing., *Polymer International*. Submitted Dec 2020. Under review.
- Delaney, L.J., **Basgul C.**, MacDonald D.W., Fitzgerald K., Hickok N.J., Kurtz S.M., Forsberg F., Acoustic Parameters for Optimal Ultrasound-Triggered Release from Novel Spinal Hardware Devices. *Ultrasound in Medicine & Biology*, 2020. 46(2): p. 350-358.

- **Basgul C.**, MacDonald D., Siskey R., Kurtz S., Thermal localization improves the interlayer adhesion and structural integrity of 3D printed PEEK lumbar spinal cages. *Acta Materialia*, May 2020. https://doi.org/10.1016/j.mtla.2020.100650
- **Basgul C.,** Yu T., MacDonald D., Siskey R., Marcolongo M., Kurtz S., Does annealing improve the interlayer adhesion and structural integrity of FFF 3D printed PEEK lumbar spinal cages? *Journal of the Mechanical Behaviour of Biomedical Materials*, Available online 27 September 2019. https://doi.org/10.1016/j.jmbbm.2019.103455.
- **Basgul C.,** Yu T., MacDonald D., Siskey R., Marcolongo M., Kurtz S., Structure-Property Relationships for 3D printed PEEK Intervertebral Lumbar Cages Produced using Fused Filament Fabrication, Journal of Materials Research, 2018 Jul 27;33(14):2040-2051. doi: 10.1557/jmr.2018.178.
- Önen M., **Basgul C.**, Yılmaz İ., Özkaya M., Demir T., Naderi S., Comparison of rigid and semirigid instrumentation acute load on vertebrae treated with PLIF/TLIF procedures: an experimental study, *Journal of Engineering in Medicine*, 2018.
- Demir T., **Basgul C.**, Pullout performance of pedicle screws. Springer, 2015.
- Tolunay T., **Basgul C.**, Demir T., Yaman ME., Arslan KA. Pedicle Screw Pullout Performance Comparison Based on Cement Application and Design Parameters. *Journal of Engineering in Medicine,* 2015.